Dynamics of wet adhesion at soft interfaces

Dynamics of Wet Adhesion at Soft Interfaces

Maciej Chudak

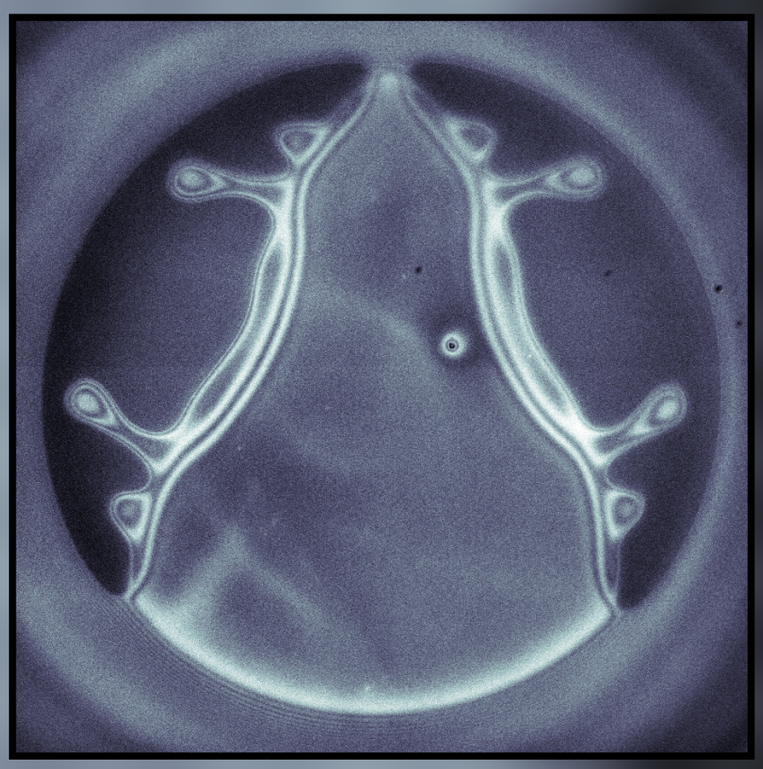

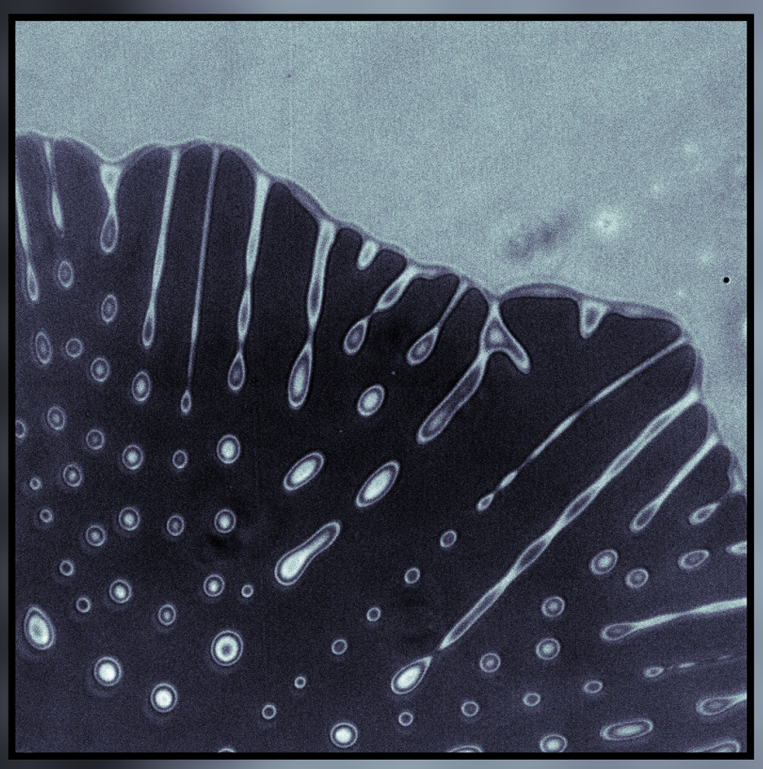

Dynamics of Wet Adhesion at Soft Interfaces

This project has received funding from the European Union's Horizon 2020 research and innovation programme under the Marie Skłodowska-Curie grant agreement No. 642861.

A catalogue record is available from the Eindhoven University of Technology Library.

ISBN: 978-90-386-5123-1

Dynamics of Wet Adhesion at Soft Interfaces

PROEFSCHRIFT

ter verkrijging van de graad van doctor aan de Technische Universiteit Eindhoven, op gezag van de rector magnificus prof.dr.ir. F.P.T. Baaijens, voor een commissie aangewezen door het College voor Promoties, in het openbaar te verdedigen op maandag 26 oktober 2020 om 11:00 uur

door

Maciej Krzysztof Chudak

geboren te Poznań, Polen

Dit proefschrift is goedgekeurd door de promotoren en de samenstelling van de promotiecommissie is als volgt:

voorzitter:	prof.dr.ir. G.M.W. Kroesen
1e promotor:	prof.dr. A.A. Darhuber
2e promotor:	prof.dr.ir. J.H. Snoeijer (Universiteit Twente)
leden:	prof.dr. M.M.G. Kamperman (Rijksuniversiteit Groningen)
	prof.dr.ir. H. van Brummelen
	dr. A. Lyulin

Het onderzoek of ontwerp dat in dit proefschrift wordt beschreven is uitgevoerd in overeenstemming met de TU/e Gedragscode Wetenschapsbeoefening.

Summary

In this work, I focus on the dynamical aspects of wet adhesion to soft surfaces. This topic is relevant to adhesion science, as adhering to wet or underwater surfaces requires the removal of liquid. This process often involves elastic materials, like the adhesive or the substrate. Understanding it requires considering the soft solid-liquid interaction as well as surface energy-driven dewetting, i.e. movement of a triple contact line. I propose a numerical model that reproduces many aspects of soft elastohydrodynamic dewetting in cases like non-axisymmetric dry spot nucleation and anisotropic expansion, dewetting on patterned surfaces and movement of trapped liquid. Additionally, I explore a switchable adhesion system utilizing static electric fields.

Contents

List of symbols

Symbol	Unit	Description
		Introduced in Chapter 1
t	s	Time
x, y, z	m	Spatial coordinates
h	m	Liquid film thickness
S	$\mathrm{N\,m^{-1}}$	Spreading parameter
$\gamma_{\zeta\theta}$	$\mathrm{N\,m^{-1}}$	Surface energy of an interface between domains ζ and θ
η	Pa s	Viscosity
Y	Pa	Young's modulus
r_{cl}	m	Contact line position
r_{cs}	m	Contact spot radius
τ	s	Squeeze-out time
κ	—	Dimensionless constant in Eq. (2.3)
R_L	m	Radius of curvature of the rubber lens
σ_{ij}	Pa	Cauchy stress tensor
f_i	$\mathrm{N\,m^{-3}}$	Cartesian components of a body force density vector
G	Pa	Shear modulus
B	Pa	Bulk modulus
ν	—	Poisson's ratio
δ_{ij}	—	Kronecker delta
e_{ij}	—	Infinitesimal strain tensor
u_i	m	Displacement vector
φ	—	Azimuthal angle
P_f	Pa	Liquid film pressure distribution
$\mathbf{v}_e, \mathbf{v}_s$	$\mathrm{m\,s^{-1}}$	Tangengial velocity of the elastomer, substrate interface
z_e, z_s	m	vertical position of the elastomer, substrate interface
Π	Pa	Disjoining pressure
C	—	Dimensionless constant in Eq. (2.9)

Continued on next page

Symbol	Unit	Description
S_Π	$\mathrm{N\,m^{-1}}$	Amplitude factor with units of surface tension
h^*	m	Nanoscopic lengthscale
n, m	—	Integers ($n > m$) defining the shape of the disjoining pressure isotherm
T_i	Pa	Interfacial traction
δ_{ij}	—	Unit tensor
n_i	—	Components of a unit normal vector at an interface
z_d, Δh_d, w_d, r_d	m	Defect height profile, center-height, half-width, position
$\mathrm{f_{hs}}$	—	Smooth Heaviside function with two continuous derivatives
$u_z^{(e)}$	m	z-component of the displacement vector of the elastomer at the liquid-elastomer interface
r	m	Auxiliary coordinate, $r^2 \equiv x^2 + y^2$
b_0, b_1	m	initial and final positions of the substrate
t_c	s	Approach time constant
s	m	Arc length of contact line path
α, β	—	Dimensionless constants in Eq. (2.20)
v_{cl}	$\mathrm{m\,s^{-1}}$	Contact line velocity
t_d	s	Time at which dewetting started
R_{crit}	m	Critical radius of a dry spot nucleus
h_{crit}	m	Critical film thickness below which dewetting may start
$\mathcal{E}$	—	Dimensionless constant in Eq. (2.26)
r_0	m	Constant in Eq. (2.27)
φ_{cl}	—	Azimuthal position of the azimuthal apex of the dry spot
		Introduced in Chapter 2
a_d, h_d	m	Droplet footprint radius, center height
L_{ec}	m	Elastocapillary lengthscale
u_A	$\mathrm{J\,m^{-2}}$	Work per unit area performed by pressure displacing an elastic surface
U_d	J	Energy needed to introduce a droplet at an interface between two elastomers
Ω_f	$\mathrm{Pa\,m^{-1}}$	Radial pressure gradient
v_d	$\mathrm{m\,s^{-1}}$	Droplet velocity
$\dot{U}_\mu$	W	Viscous dissipation rate
Δt	s	Droplet coalescence time
P_{H}	Pa	Hertzian pressure distribution
P_0	Pa	Central pressure in a Hertzian distribution
β_d	—	Nondimensionalized droplet radius

Continued on next page

Symbol	Unit	Description
P_{JKR}	Pa	The Johnson-Kendall-Roberts pressure distribution
P_1	Pa	Scale of the non-Hertzian P_{JKR} component
d	m	Radial distance to the edge of the contact spot
$I_c(d,t)$	—	Time-dependent interferogram radial intensity profile
d_d	m	Position of the midpoint of the droplet
ψ	$\mathrm{m^3\,s\,kg^{-1}}$	Ratio of droplet velocity to local pressure gradient
$\widetilde{S}$	$\mathrm{N\,m^{-1}}$	Spreading parameter determined from droplet geometry
A_n	$\mathrm{m^2}$	Droplet footprint area after the n-th coalescence cascade
ζ_n	—	Area reduction ratio in the n-th coalescence cascade
We	—	The Weber number
Oh	—	The Ohnesorge number
A, λ	m	Surface wave pattern amplitude, wavelength
v_{avg}	$\mathrm{m\,s^{-1}}$	Average velocity of the contact line moving over the wave pattern
		Introduced in Chapter 3
h_p, r_p, d_p	m	Micropillar height, radius, spacing in an array
		Introduced in Chapter 4
$\mathbf{E}$	$\mathrm{V\,m^{-1}}$	Electric field
u, u_M	m	Displacement of probe, motorized z-stage
F	N	Measured force on the probe
k	$\mathrm{N\,m^{-1}}$	Machine stiffness of the stage-probe system
A_p	$\mathrm{m^2}$	Contact area
R_p	m	Probe radius of curvature
u_p	m	Indentation depth
ε_0	$\mathrm{F\,m^{-1}}$	Vacuum permittivity
ε_r	—	Relative material permittivity
V	V	Electric potential
ρ	$\mathrm{C\,m^{-3}}$	Volume charge density
$\mathbf{J}$	$\mathrm{A\,m^{-2}}$	Current density
σ	$\mathrm{S\,m^{-1}}$	Electrical conductivity
∇_t	—	Surface gradient operator
σ_s	S	Surface conductivity
RH	—	Relative humidity
E_c	$\mathrm{V\,m^{-1}}$	Critical electric field magnitude above which conductivity is field-dependent
s_L	$\mathrm{m\,V^{-1}}$	Parameter in Eq. (5.5)
F_{es}	N	Force exerted on the probe by the electric field
T_{ij}	Pa	Maxwell stress tensor

Continued on next page

Symbol	Unit	Description
$\mathbf{D}$	$\mathrm{C\,m^{-2}}$	Electric displacement field
$\mathbf{S}$	Pa	Traction exerted by the electric field on a surface
w_a	m	Electrode array width and length
a	m	Electrode stripe half-width
b	m	Electrode array half-period
h_c	m	Ceramic substrate thickness
φ	—	Micropillar array volume filling ratio
a_L, h_L	m	Probe radius, thickness
x_m, y_m, z_m	m	Computational domain width, length, height
h_e	m	Elastomer layer thickness
δ	m	Air gap thickness
V_0	V	Applied voltage

List of Tables

List of Figures

Chapter 1

Introduction

How do we prevent cars from aquaplaning on wet roads? [Fig. 1.1(a)] How do we make sure roller bearings won't wear down quickly? How can aquatic animals stick to underwater or wet surfaces? [Fig. 1.1(b)] To answer these questions we need to understand how thin liquid films behave when confined between soft surfaces. In some cases, the liquid film is desired to be stable to prevent lubricated surfaces from touching.[1,2] In other cases, the opposite is sought. A car will retain traction if water will be removed from the tires-asphalt interface quickly enough.[3–13] Thin liquid film removal is desired in some industrial applications, like nanoimprint lithography.[14–19]

The process of thin liquid film removal is called *dewetting* and can refer to a system transitioning from a solid-liquid-air to solid-air interface or solid-liquid-solid to solid-solid. The liquid film is usually removed through nucleation and growth of dry spots (as in Fig. 1.2), but if it is thin enough it may undergo spinodal dewetting due to surface instabilities.[20] Figure 1.3 shows dewetting of a thin liquid film in a soft solid-liquid-soft solid system, where the liquid is intercalated between a soft elastomer surface and a soft elastomer hemisphere.

The rupture of thin liquid films and liquid removal are widely studied. Roberts and Tabor reported the collapse of thin liquid films below 40 nm confined between a rubber surface and a lens.[22] Brochard-Wyart and de Gennes presented an analytical model for the dewetting of water films between a rigid solid and a rubber.[23] They derived the scaling law for the growth rate of an axisymmetric dry spot. Martin and Brochard-Wyart experimentally confirmed the scaling laws.[24]

Figure 1.1: (a) A car will slip if a water film forms between the tires and asphalt, causing aquaplaning. (b) A frog can stick to wet and underwater rocks, even in strong currents.

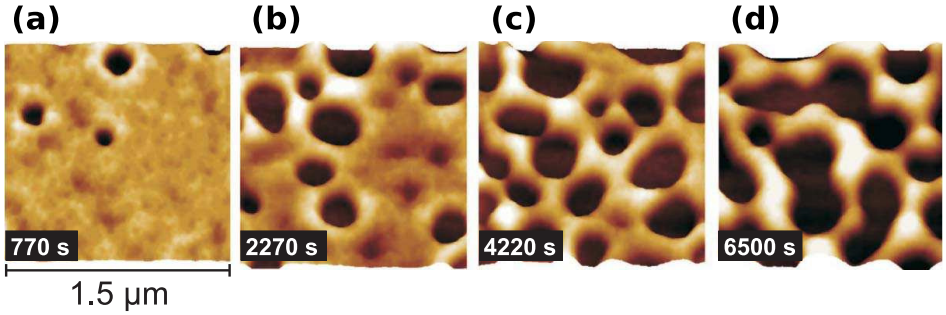

Figure 1.2: Dewetting morphology of a 3.9 nm polystyrene film (molecular mass 2000 u) at 53°C on a silicon wafer with a 191 nm thick silicon oxide layer, as recorded by in situ AFM. Adapted from Ref. [21].

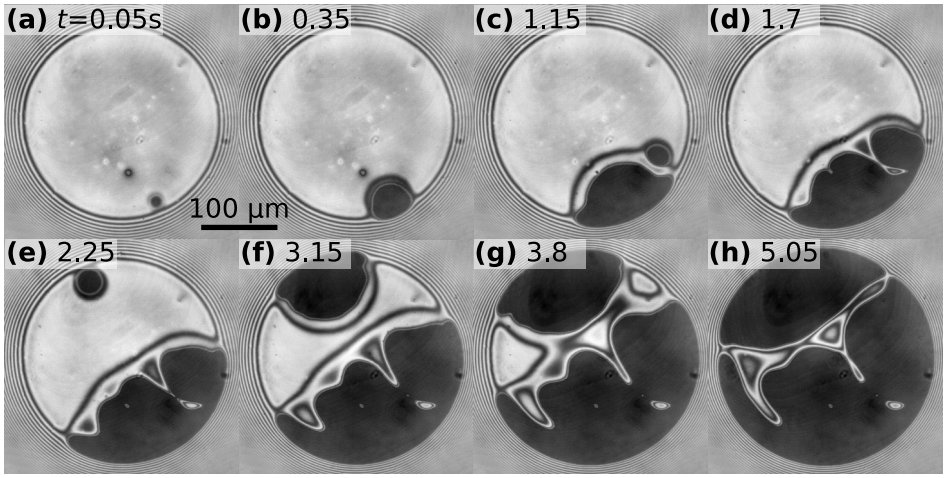

Figure 1.3: Dewetting of a thin liquid film [light circular spot in (a)] intercalated between a soft elastomer surface and a soft elastomer hemisphere.

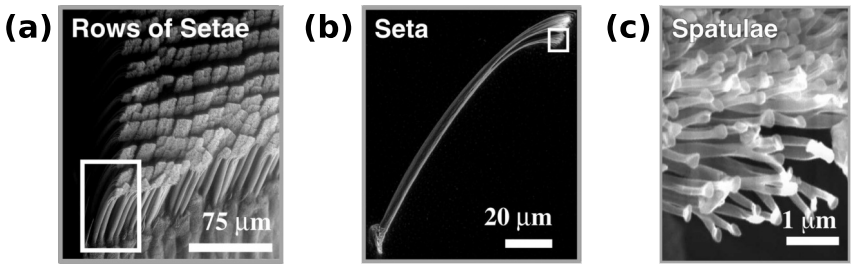

Figure 1.4: Scanning electron microscopy images of a gecko foot, showing its morphology in microscale. Adapted from Ref. [37].

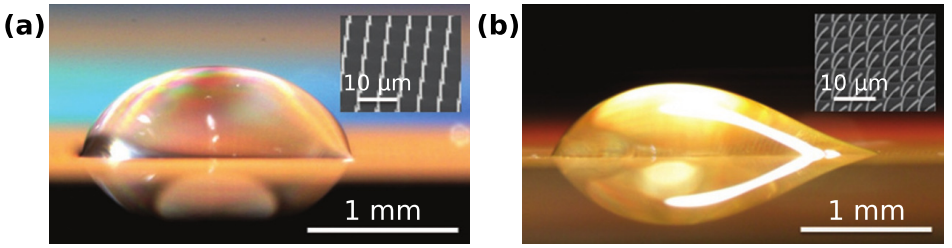

Figure 1.5: Droplets spreading on micropatterned surfaces. (a) Straight micropillars (SEM image in the inset) cause the droplet to spread uniformly. (b) Slanted micropillars cause anisotropic spreading. In both cases the pillars have a diameter of 0.5 μm, spacing of 3.5 μm and height of 10 μm. Adapted from Ref. [43].

Persson *et al.* reported how pressure distribution inside the contact area affects the contact line speed during dewetting.[25]

The problem of liquid removal is only one aspect of wet adhesion. There are ongoing efforts to develop novel adhesive systems utilizing functional surfaces with unusual wetting and adhesive properties thanks to being covered in a micropattern.[26–36] One strategy is to try mimicking nature. Autumn *et al.*[37–40] described the gecko foot adhesion mechanism, which can conform to rough surfaces and adhere due to their intricate microstructures (Fig. 1.4) and the van der Waals forces. Biomimetic micro-pillar arrays made from an elastic polymer were demonstrated to conform well to rough surfaces, providing better adhesion than a flat elastomer would.[41,42]

Patterned surfaces can exhibit unusual wetting properties. Understanding how liquids spread on patterned surfaces is an active research

topic.[44–46] Barthlott and Neinhuis[47] investigated the superhydrophobic properties of lotus leaves due to their intricate microstructure. Figure 1.6 shows similar structures found in other plants.[48] Figure 1.7 shows another example of a superhydrophobic micropattern in nature, found on the skin of aquatic insects called *springtails*. The pattern on their plastron prevents them from getting wet, which would interfere with their ability to breathe through the skin.[49] Numerous works[51–55] demonstrated that these properties can be replicated by manufactured patterns and showed the importance of a hierarchical two-lengthscale topography that is necessary to reproduce the effect. Figure 1.8 shows an example, the mushroom shape of the pillars causes the patterned surface to be omniphobic, that is, prevent the wetting by any liquid, independant of its surface tension and contact angle on a flat surface of the same material.[56–59]

Switchable adhesion is of particular interest. Reddy *et al.* developed a system of thermoresponsive micropillars, which allowed to switch adhesion on and off by changing the temperature.[60] Drotlef *et al.* demonstrated that pillars with embedded neodymium nanoparticles will bend when a magnetic field is applied, which can also be used to control the adhesive properties of the surface.[61]

In chapter 2 we describe soft solid-liquid-solid dewetting in a more general way, considering non-axisymmetric cases. We consider the dynamics of sessile droplets at soft interfaces, propelled by the pressure gradient (chapter 3). In chapter 4 we describe dewetting of patterned substrates pressed in a liquid against a soft solid. Finally, we consider a switchable adhesion mechanism by means of static electric fields (chapter 5).

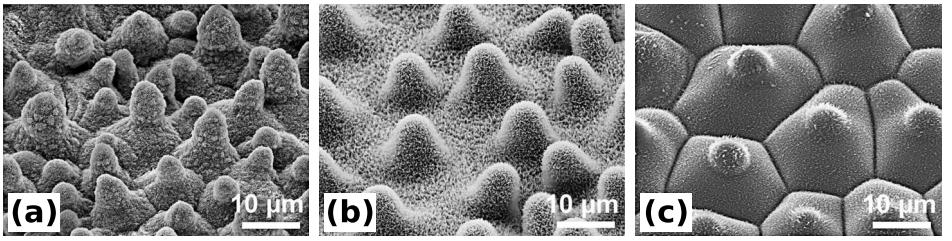

Figure 1.6: Scanning electron microscopy images showing the microstructures on the surface of plant leaves. (a) *Nelumbo nucifera* (lotus), (b) *euphorbia myrsinites* (myrtle spurge), (c) *colocasia esculenta* (taro) and Adapted from Ref. [48].

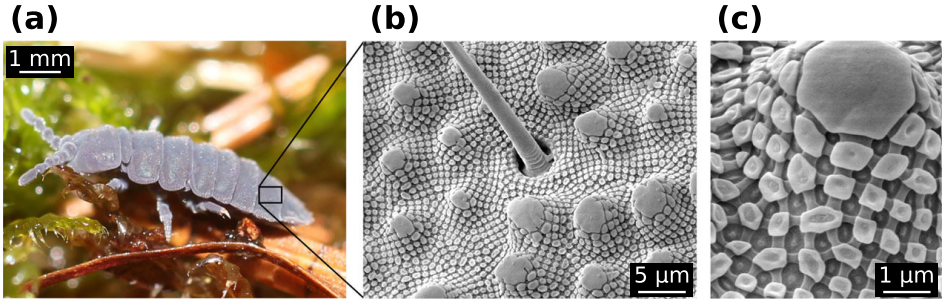

Figure 1.7: (a) *Tetrodontophora bielanensis*, a springtail. (b,c) Scanning electron microscopy images showing the microstructures of the plastron. Adapted from Ref. [50].

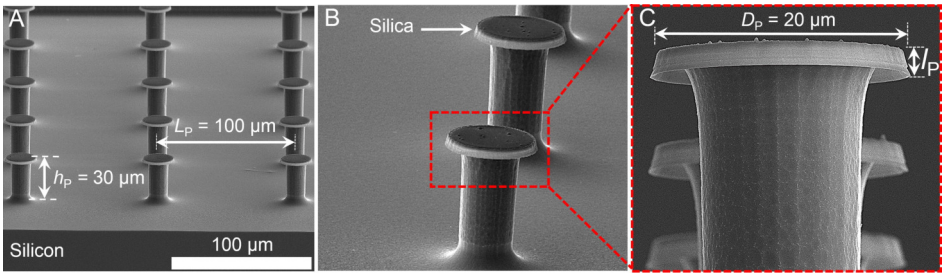

Figure 1.8: Scanning electron microscopy images showing mushroom-shaped pillars, providing an omniphobic surface and inspired by nature. Adapted from Ref. [59].

Chapter 2

Non-axisymmetric elastohydrodynamic solid-liquid-solid dewetting: Experiments and numerical modelling

2.1 Introduction

The presence and stability of thin liquid films between two solid surfaces is of great scientific and technological relevance for many systems and applications. For minimizing wear in bearings, a stable liquid film is desirable.[1,2] To prevent aquaplaning on wet roads, the liquid film should be removed as efficiently as possible to maximize traction.[3–13] Certain carnivorous plants developed an prey capture strategy based on insect aquaplaning.[11,62] Similarly, for residue-free nanoimprint lithography, a swift and complete removal of intervening liquid is required.[14–19] The strength of adhesion between organic or polymeric surfaces is considerably reduced by the presence of a water film, as the Hamaker constant for the interaction of e.g. two polystryrene or poly-tetra-fluoro-ethylene halfspaces across vacuum is 7 to 10 times higher than across an ultrathin water layer.[63]

Roberts and Tabor reported the spontaneous collapse of thin liquid films confined between a rubber surface and an SiO_2 lens for film

thicknesses below 40 nm.[22] Serayssol and Davis studied the influence of surface interactions on the elastohydrodynamic collision of two suspended spheres.[64] Becker and Mugele and de Beer *et al.* studied the dewetting of molecularly thin liquid films between mica substrates using a surface forces apparatus.[65,66] They observed dewetting transitions and trapped liquid for high approach rates of the two substrates. Persson and Mugele provided an exhaustive review of squeeze-out of molecularly-thin wetting and non-wetting liquid films.[67] Bandyopadhyay *et al.* showed that a micrometer-scale corrugation of the elastomeric punch can effectively suppress the dewetting transition of confined ultrathin polystyrene films.[68] Li *et al.* found that the addition of the surfactant sodium-dodecyl-sulfate (SDS) can prevent dewetting and induce film stability.[69]

Brochard-Wyart and de Gennes were the first to present an analytical model for the dewetting of water films between a rigid solid and a rubber.[23] By balancing the surface energy change with the viscous dissipation in the liquid they derived the scaling law for the growth rate of an axisymmetric dry spot. Martin and Brochard-Wyart presented experiments that confirmed the predicted scaling laws.[24] Persson *et al.* additionally considered the nonuniformity of the pressure distribution inside the contact area.[25] Brochard-Wyart and Martin extended the model towards materials that are characterized by a static shear modulus, a high frequency modulus, and a relaxation time.[70] Carbone and Persson extended the model of Brochard and de Gennes towards dewetting of liquid films between viscoelastic materials.[71]

Brochard *et al.* focused on axisymmetric dewetting induced by purposely introduced defects or protrusions on one of the confining solids. In contrast, in this manuscript we present systematic experiments of non-axisymmetric dewetting. The experimental setup is illustrated in Fig. 2.1(a). An elastomeric half-sphere is pressed onto a flat layer of the same material with liquid confined in between them. Due to the applied pressure the liquid film thickness h decreases in time. After h has become sufficiently low, dry-spot nucleation may occur usually near defects and surface irregularities, as shown in Fig. 2.1(d,e). We developed a 3D fully-coupled numerical model of the dewetting process, which combines thin film flow with elastic surface and bulk deformation and which reproduces many features observed in the experiments.

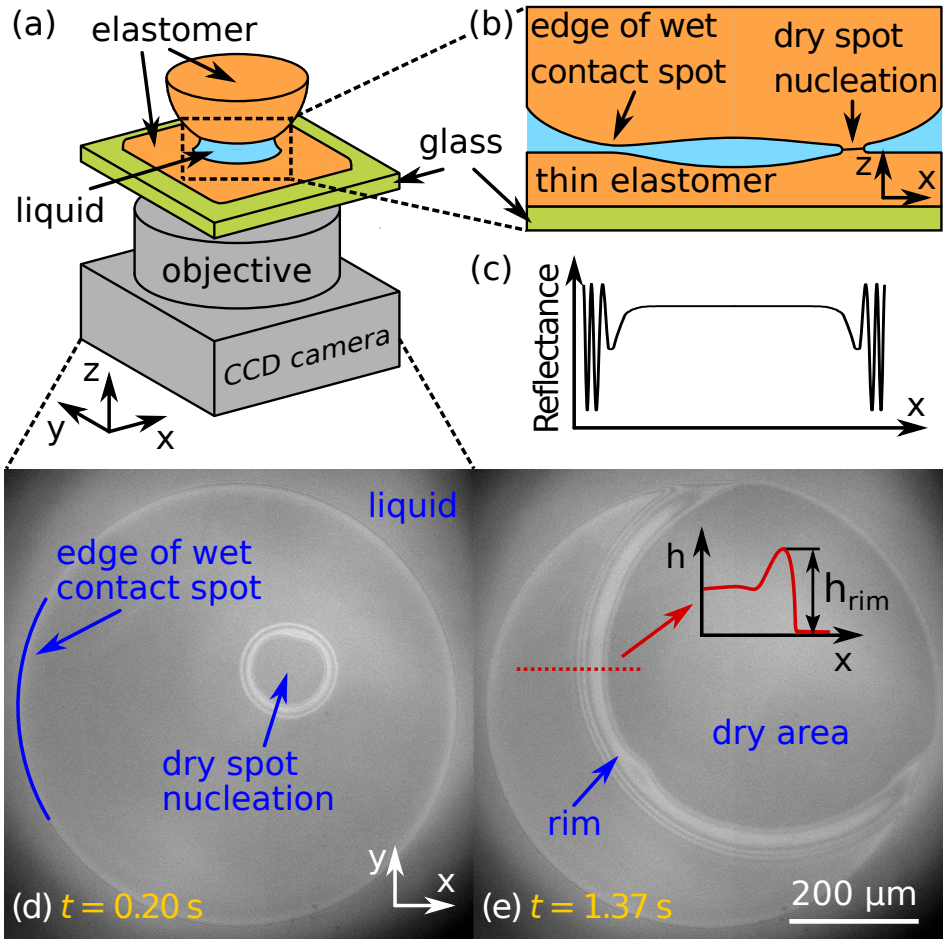

Figure 2.1: (a) Sketch of the experimental setup. (b) Magnified cross-section of the wet contact spot. (c) Schematic of a typical observed light interference pattern that contains information about the film thickness distribution. (d,e) Microscope images showing the nucleation and growth of a dry-spot in the confined thin liquid film. The time $t = 0$ corresponds to the moment of nucleation.

2.2 Modelling

2.2.1 Analytical Models

The stability of thin liquid films confined between solid elastic media is governed by the spreading parameter $S \equiv \gamma_{AB} - \gamma_{AL} - \gamma_{BL}$,[72] which depends on the interfacial energies of the contacting media, γ_{AB} being the surface energy of the dry A-B elastomer interface, γ_{AL} and γ_{BL} the solid-liquid interfacial energies, respectively. For $S > 0$ the liquid is always stable but for $S < 0$ dewetting may occur.

In the case of circular dry spots initiating in the center of the contact area, the growth dynamics may be predicted by comparing the rate of surface energy gain with the rate of viscous dissipation in the rim forming in front of the contact line [see Fig. 2.1(e)]. The dissipation rate depends on the shape of the rim, which depends on the surface and elastic properties of the materials in contact. Brochard-Wyart and De Gennes derived the following relation for the time evolution of the dry spot radius[23]

$$r_{cl}(t) \sim \left(\frac{|S|}{\eta}\, t\right)^{3/4} \left(\frac{|S|}{Y}\right)^{1/2} h^{-1/4}, \tag{2.1}$$

where η is liquid viscosity, Y is the Young's modulus of the elastomer and h is the liquid film thickness (assumed uniform). Persson *et al.* additionally considered the nonuniformity of the pressure distribution inside the contact area.[25] They assumed a Hertzian distribution,[73] leading to the following implicit solution for the time t needed for the contact line position to reach a certain position r_{cl}

$$\frac{t}{\tau} \sim \int_0^{r_{cl}/r_{cs}} \frac{\xi^{1/3}}{1 + \kappa\xi^2(1-\xi^2)^{-1/2}}\, \mathrm{d}\xi\,. \tag{2.2}$$

Here, r_{cs} is the radius of the contact spot, τ the squeeze-out time derived from Eq. (2.1) by solving for the time when $r_{cl}(\tau) = r_{cs}$, and κ is a parameter dependent on the geometrical and material properties of the system

$$\kappa \equiv \frac{1}{\pi} \frac{h r_{cs}}{R_L} \frac{Y}{|S|}\,, \tag{2.3}$$

where R_L is the radius of curvature of the rubber lens and h is also assumed to be uniform.

For values of κ typical for our experimental geometry and material systems, the solution of Eq. (2.2) is very well approximated by Eq. (2.1), up to approximately a third of the contact spot radius.

2.2.2 Numerical model

We developed a theoretical model to simulate soft elastohydrodynamic lubrication phenomena and the dewetting of thin films between soft elastic surfaces numerically. The model combines the Reynolds equation for the thin liquid film flow and linear elasticity accounting for the stresses and deformations of the soft elastomeric components. The three dimensional implementation allows us to study non-axisymmetric geometries. All simulations were performed using the finite element software COMSOL Multiphysics vs. 5.3.

2.2.3 Linear elasticity

The elastic deformation in the limit of slow deformation and small strain is governed by the Cauchy momentum equation for a stationary system

$$\sum_{i=1}^{3} \frac{\partial \sigma_{ij}}{\partial x_i} = -f_j \,, \tag{2.4}$$

where σ_{ij} is the Cauchy stress tensor and f_i are the Cartesian components of an external body force density vector. Due to the small dimensions, we neglect gravity. The body force density is thus assumed to vanish $f_i = 0$.

We assume the elastic material properties to be linear, non-dissipative, isotropic and homogeneous. The corresponding constitutive equation is

$$\sigma_{ij} = 2Ge_{ij} + \left(B - \frac{2G}{3}\right) e_{kk}\delta_{ij} \,, \tag{2.5}$$

where

$$G \equiv \frac{Y}{2(1+\nu)} \quad \text{and} \quad B \equiv \frac{Y}{3(1-2\nu)} \tag{2.6}$$

are the shear and bulk modulus, Y and ν are Young's modulus and Poisson's ratio. We assumed $\nu = 0.49$ to represent the effective incompressibility of the elastomer at the pressures relevant to our experiments.[74] Moreover, δ_{ij} is the Kronecker delta and e_{ij} is the infinitesimal

strain tensor, which depends on the displacement vector u_i via

$$e_{ij} = \frac{1}{2}\left(\frac{\partial u_i}{\partial x_j} + \frac{\partial u_j}{\partial x_i}\right). \tag{2.7}$$

For computational simplicity we assume the substrate to be rigid and oriented parallel to the base plane of the hemisphere. In the appendix, we consider the case of elastomeric substrates using an Arbitrary Lagrangian-Eurlerian (ALE) approach.

As for boundary conditions (BCs), the base of the hemisphere is assumed to be attached to a rigid surface and thus $u_i(r, z = 0) = 0$. The surface of the solid not in contact with the liquid (i.e. the elastomer-air interface) is assumed to be traction-free and therefore $\sum_i \sigma_{ij} n_i = 0$. In the azimuthal direction the computational domain is bounded by two symmetry planes, $\varphi = 0$ and $\varphi = \varphi_0$, φ being the azimuthal angle, where the normal displacement vanishes, $u_\varphi = 0$. As a consequence, the radial displacement at $r = 0$ vanishes, $u_r(r = 0, z) = 0$. The considered geometry and boundary conditions (BCs) are illustrated in Fig. 2.2.

2.2.4 Thin liquid film flow

Since the typical film thickness (order 100 nm) is much smaller than the radius of the contact spot r_{cs} (order 300 µm), a thin film approximation can be used to describe the liquid flow. Assuming impenetrable liquid-solid interfaces, incompressible laminar flow subject to no-slip BCs, the Reynolds equation can be solved

$$\frac{\partial h}{\partial t} + \nabla_{||} \cdot \left[h\frac{\mathbf{v}_e + \mathbf{v}_s}{2} - \frac{h^3}{12\eta}\nabla P_f\right] = 0\,, \tag{2.8}$$

to obtain the pressure distribution P_f. Here, t is time, η is the dynamic viscosity of the liquid, and $\mathbf{v}_e$ and $\mathbf{v}_s$ are the tangential velocities of the liquid-elastomer interface and the substrate surface [see Fig. (2.2)], respectively, which are computed from their elastic displacements. The liquid film thickness $h(x, y, t)$ is calculated from the positions of the boundaries $h = z_e - z_s$.

Partial wettability in solid-liquid-solid systems can be implemented in an elastohydrodynamic framework by means of the concept of

disjoining pressure Π.[75] We assume the following empirical form

$$\Pi(h) = C\left[\left(\frac{h^*}{h}\right)^n - \left(\frac{h^*}{h}\right)^m\right], \tag{2.9}$$

with

$$C \equiv \frac{|S_\Pi|}{h^*}\frac{(n-1)(m-1)}{n-m}, \tag{2.10}$$

where S_Π is an amplitude factor with units of surface tension (N/m), h^* is a nanoscopic lengthscale, and n and m are integers ($n > m$) defining the shape of the disjoining pressure isotherm and the limiting behavior for $h \to 0$ and $h \to \infty$. We typically chose $h^* = 10$ nm. The value of $\Pi(h)$ is different from zero essentially only for ultrasmall film thicknesses ($h \lesssim 10h^*$), whereas it is immeasurably small at microscopic distances, $\Pi(h \gg h^*) \approx 0$. The divergence of Π for $h \to 0$ enforces a non-zero minimum film thickness, which helps alleviate the hydrodynamic stress singularity associated with moving contact lines.[76]

The two-dimensional computational domain of the liquid phase has three boundaries. At the azimuthal bounding planes $\varphi = 0$ and $\varphi = \varphi_0$, we prescribe symmetry conditions

$$\frac{\partial h}{\partial \varphi} = 0 \quad \text{and} \quad \frac{\partial P_f}{\partial \varphi} = 0\,. \tag{2.11}$$

At the external boundary, i.e. outside of the contact spot, the pressure is set to zero.

2.2.5 Interfacial coupling conditions

At the elastomer-liquid boundary a traction $T_i = \sum_j \sigma_{ij} n_j$ is exerted by the liquid on the solid

$$T_i = \sum_{j=1}^{3} \frac{\eta}{h}\left(\delta_{ij} - n_i n_j\right)\left(v_{e,j} - v_{s,j}\right) - (P_f + \Pi) n_i, \tag{2.12}$$

where δ_{ij} is the unit tensor and n_i are components of the unit normal vector of the liquid-elastomer interface. The second term in Eq. (2.12) corresponds to a pressure load applied to the solid-liquid interface, which is a superposition of the total fluid pressure calculated from Eq. (2.8) and the disjoining pressure $\Pi(h)$.

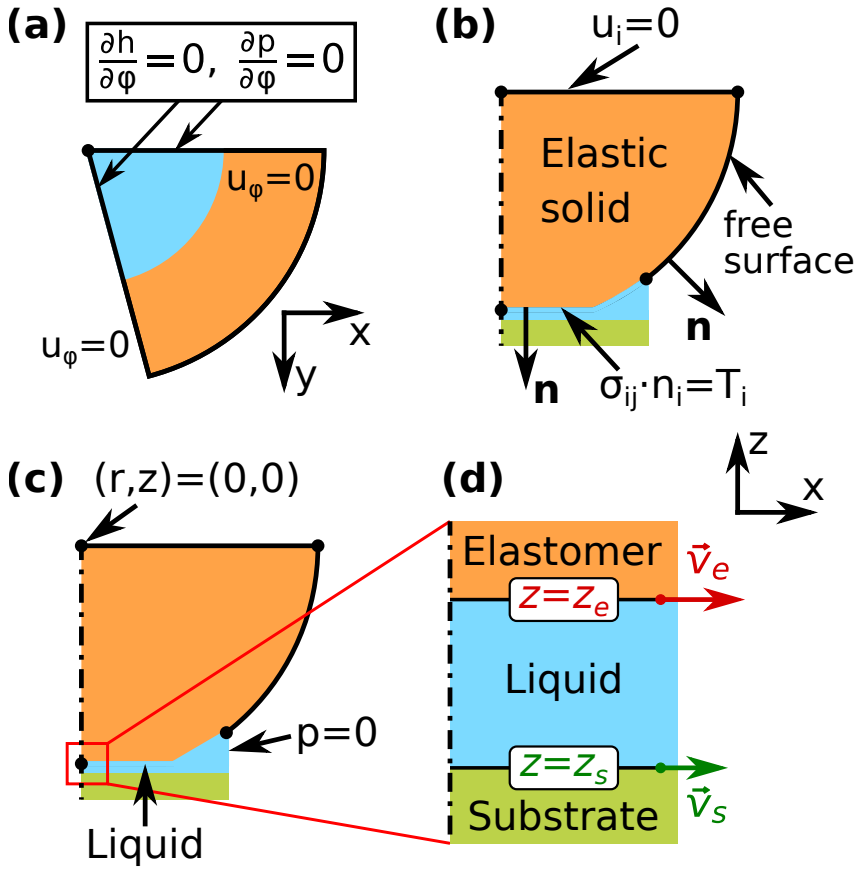

Figure 2.2: Boundary conditions used in the numerical model.

2.2.6 Initial and kinematic conditions

In order to induce dry spot nucleation at a predefined location, we introduce a defect with shape

$$z_d(\mathbf{r}) = \Delta h_d \, \mathrm{f_{hs}} \left(1 - 2 \frac{|\mathbf{r} - \mathbf{r}_d|}{w_d} \right), \tag{2.13}$$

as part of the surface topography of the rigid substrate. Here, Δh_d and w_d define the height and width of the defect, $\mathbf{r}_d$ is the defect position and $\mathrm{f_{hs}}$ is a smooth Heaviside function with two continuous derivatives

$$\mathrm{f_{hs}}(\tilde{t}) = \begin{cases} 0 & \text{for } \tilde{t} < -1 \\ 1 & \text{for } \tilde{t} > 1 \\ \frac{1}{2} + \frac{15}{16}\tilde{t} - \frac{5}{8}\tilde{t}^{\,3} + \frac{3}{16}\tilde{t}^{\,5} & \text{otherwise.} \end{cases} \tag{2.14}$$

The dynamics of the system is generated by a vertical motion of the rigid substrate, while the base plane of the elastomeric hemisphere is held fixed. The vertical position of the liquid-elastomer interface is

$$z_e(\mathbf{r}, t) = u_z^{(e)}(\mathbf{r}, t) - \sqrt{R_L^2 - r^2}, \tag{2.15}$$

where $u_z^{(e)}$ is the z-component of the displacement vector of the elastomer at the liquid-elastomer interface and $r^2 \equiv x^2 + y^2$.

We prescribe the time dependence of the vertical position of the liquid-substrate interface as

$$z_s(\mathbf{r}, t) = b_0 + (b_1 - b_0) \, \mathrm{f_{hs}} \left[2 \frac{t}{t_c} - 1 \right] + z_d(\mathbf{r}) - R_L, \tag{2.16}$$

where b_0 and b_1 are the initial and final positions of the substrate and t_c is the approach time constant. The value of the time constant t_c is restricted by the requirements of slow elastic deformation and by the timescale of the dewetting process. We chose t_c much shorter than the time required for dry spot nucleation and found that the precise value of t_c then effectively has no influence on the liquid film thickness evolution.

At $t = 0$ the displacement field of the solid is set to zero. The initial pressure distribution is assumed to be zero in the entire liquid. The initial condition for h is determined by Eqs. (2.15) and (2.16).

2.2.7 Axisymmetric variant of the model

If a dry spot nucleates in the center of a circular contact spot, dewetting can evolve in an axially symmetric manner. In this case we simplified the model and considered a one-dimensional liquid and a two-dimensional solid domain using cylindrical coordinates. Equation (2.7) simplifies to

$$\begin{aligned} e_{rr} = \frac{\partial u_r}{\partial r}\,, \quad e_{\phi\phi} = \frac{u_r}{r}\,, \quad e_{zz} = \frac{\partial u_z}{\partial z}\,, \\ e_{r\phi} = e_{\phi z} = 0\,, \quad e_{zr} = \frac{1}{2}\left(\frac{\partial u_r}{\partial z} + \frac{\partial u_z}{\partial r}\right). \end{aligned} \tag{2.17}$$

Equation (2.8) becomes

$$\frac{\partial h}{\partial t} + \frac{1}{r}\frac{\partial}{\partial r} r \left(h \frac{v_e + v_s}{2} - \frac{h^3}{12\eta}\frac{\partial P_f}{\partial r} \right) = 0\,. \tag{2.18}$$

The boundary conditions remain in effect. At the symmetry axis $r = 0$ we have

$$\frac{\partial h}{\partial r} = 0, \quad \frac{\partial p}{\partial r} = 0, \quad u_r = 0 \quad \text{at} \quad r = 0. \tag{2.19}$$

2.3 Materials and methods

The elastomer used was a silicone-based, heat-curable, two-component polymer resin (Smooth-On, Encapso K). Samples were prepared by mixing the two components in a 1:1 weight ratio and depositing a droplet on a borosilicate glass slide. The droplet spreads into a layer approximately 200 to 300 μm thick and 2 cm wide. In order to obtain a spherical silicone cap, resin was deposited on the flat side of a fused silica half-ball lens (Edmund Optics, product number 67-395, radius of curvature 1.5 mm), which was glued to a borosilicate glass substrate using a UV-curable adhesive (Norland Optical Adhesive 65). The procedure was similar to the one described in,[77] except that we used Gibbs confinement[78] to define the shape rather than a flat hydrophobic substrate. The radius of curvature of the spherical cap can be adjusted by the deposited volume of resin. After curing for at least 24 hours at room temperature, an optically transparent elastomer was obtained, with a Young's modulus given by the manufacturer as 1.365 MPa.

Compared to using micro-machined molds this contact-free fabrication procedure yields molecularly smooth surfaces.

The liquid used in the experiments was a perfluoropolyether (Solvay, Fomblin Y LVAC 14/6, average molecular weight 2500). It is essentially non-volatile at room temperature, has a viscosity η of 140 cSt at 20°C, a density of 1890 $\mathrm{kg\,m^{-3}}$ at 25°C, and a refractive index n_D of 1.298. With the chosen materials, swelling of the polymer was never observed. The spreading parameter S can vary with contamination and nonuniformity of the polymer surfaces. An estimate derived from the analysis of the shape of trapped liquid droplets, as discussed in Ref. [79], is close to 14 mN/m.

A detailed sketch of the experimental setup is presented in Fig. 2.3. An incoherent blue LED light source (Roithner) is used with a center wavelength of 450 nm. A nonpolarizing beam splitter (Thorlabs, product number CCM1-BS013/M) is used to direct the light through the objective (Olympus, LUCPlanFL N 20x/0.45NA) towards the sample and the reflected light from the sample to the CCD camera (Basler, model piA1000-60gm). A borosilicate glass cover slip with dimensions 1 mm×25 mm×75 mm is used as a rigid support for the silicone layer. The latter is covered with liquid and brought in wet contact with the silicone hemispherical lens. A grey filter with a drop of an index matching liquid is used to lessen unwanted reflections from the glass-air interface. The top glass slide is pivoting on a rubber platform on one side. On the other side it is supported by a force gauge (Strain Measurement Devices, model S100 0.2N) with measurement range 0.2 N and spring constant 89 N/m. By using a vertical translation stage the silicone lens can be lowered onto the silicone substrate. The load on the lens can be regulated from 0 to roughly half of the weight of the top glass slide.

Light reflected from the silicone-liquid interfaces gives rise to interference fringes [Fig. 2.1(c-e)], which allow to determine the film thickness distribution of the liquid. Details of the film thickness evaluation are provided in the supplementary information.

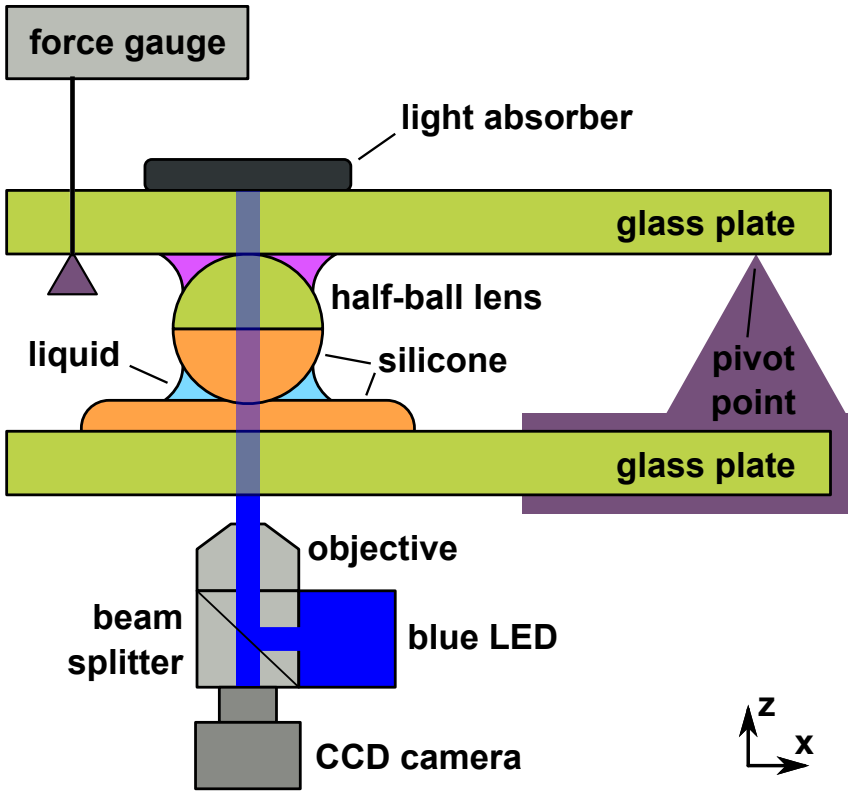

Figure 2.3: Detailed sketch of the experimental setup.

2.4 Experimental Results

2.4.1 Nucleation inside the contact spot

In Fig. 2.4 the positions of the contact line are plotted (symbols) as a function of time for the experiment shown in Fig. 2.1(d,e), where dewetting started 91 μm from the center of the contact spot. The contact line positions were extracted in the directions radially inward and outward relative to the center of the contact spot. The dashed lines represent fitted powerlaw relations $r_{cl} \sim t^{3/4}$ according to Eq. (2.1), which are excellent approximations during the early stage of the dewetting process. Later, the measured data deviate from this behavior, because the contact line is accelerated by the radially-increasing pressure gradient in the contact spot. The dash-dotted lines correspond to Eq. (2.2), where κ was treated as a fitting parameter, which shows excellent agreement over the entire data range.

However, an approximate implicit solution can be found by considering a shifted Hertzian pressure distribution

2.4.2 Nucleation at the edge of the contact spot

Most frequently dry spots nucleate at the edge of the contact spot because the liquid film thickness is smallest there. An example is shown in Fig. 2.5(a). In such a case, the contact line velocity exhibits a high degree of anisotropy as shown in Fig. 2.5(b-f). The dewetting speed is approximately twice as fast along the perimeter of the contact spot compared to direction radially inwards. In Fig. 2.5(a) two dry spots nucleated roughly simultaneously at the edge of the contact spot. Both dry spots grow at the same rate and the complex contact line morphology evolves in an almost perfectly mirror-symmetric fashion. This is a clear indication that the dewetting dynamics and the contact line morphology are governed by elastocapillary and elastohydrodynamic effects rather than by randomly distributed surface irregularities.

Figure 2.6 illustrates the time dependence of the arc length s representing contact line position measured both along the edge of the contact spot and radially inwards, as indicated with arrows in Fig. 2.5(e). In the very early stage of dewetting the dry spot expands roughly isotropically. Given enough time, the speed towards the center

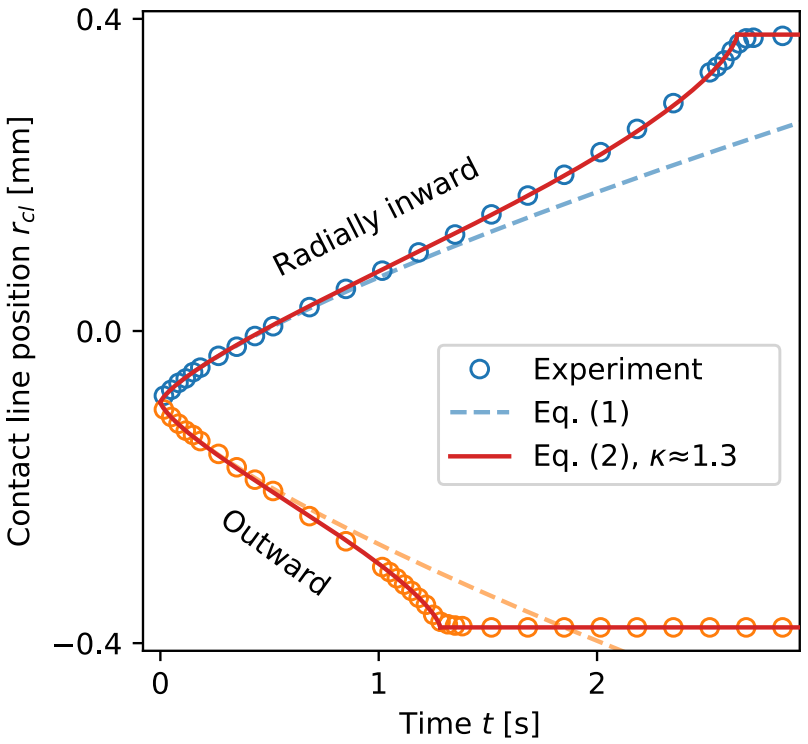

Figure 2.4: Radial contact line positions r_{cl} as a function of time determined along a diametral line connecting the nucleation center with the center of the contact spot. Dewetting started 91 μm from the center of the contact spot.

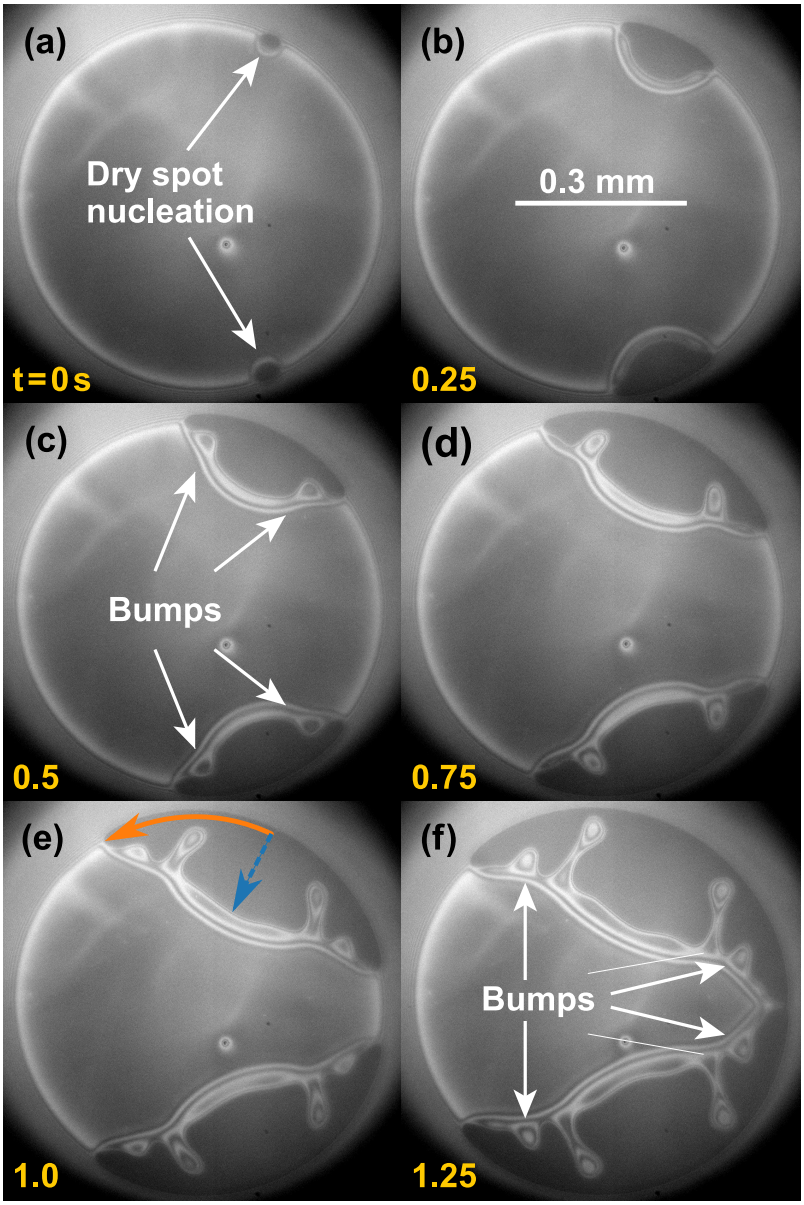

Figure 2.5: (a) Simultaneous dry-spot nucleation in two locations on the perimeter of the contact spot. (b-f) The expansion rate of the dry spots is highly anisotropic and significantly faster along the edge of the contact spot.

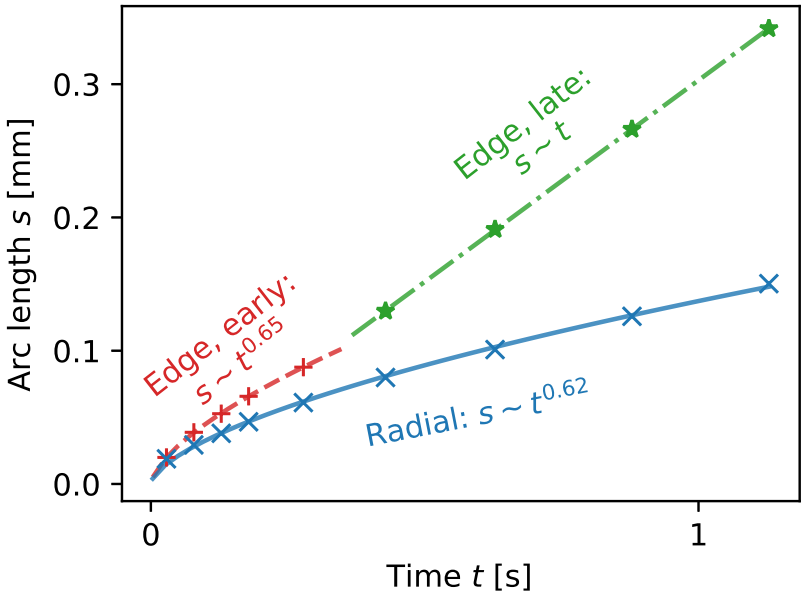

Figure 2.6: Contact line displacements measured along the solid and dashed lines in Fig. 2.5(e).

(crosses in Fig. 2.6) conforms to a power law $s \sim t^{0.62}$ (solid line), whereas the speed along the perimeter becomes a constant, $s \sim t$ (dash-dotted line), and is significantly higher. We note that near the perimeter the pressure gradient has its strongest position dependence. Therefore, it is not to be expected that the time dependence of the contact line position should follow Eq. (2.1), which assumes uniform pressure. Furthermore, we note that in our experiments the scaling exponents for the *initial* azimuthal and radial dewetting typically vary between 0.6 and 1.3, and 0.6 and 1, respectively, depending on the distance of the dewetting spot from the edge of the contact spot.

To investigate this phenomenon further, Fig. 2.7 presents high magnification images of the region near the apex of the contact line moving along the perimeter. After the initial growth of a small dry spot [Fig. 2.7(a)] the liquid film thickness distribution is constant in the immediate vicinity of the apex of the contact line. Effectively the local morphology is time-invariant and propagates with a constant shape and azimuthal velocity. Thickness nonuniformities ('bumps') form on the neighboring liquid rim [Fig. 2.5(c-f) and Fig. 2.7(c-f)].

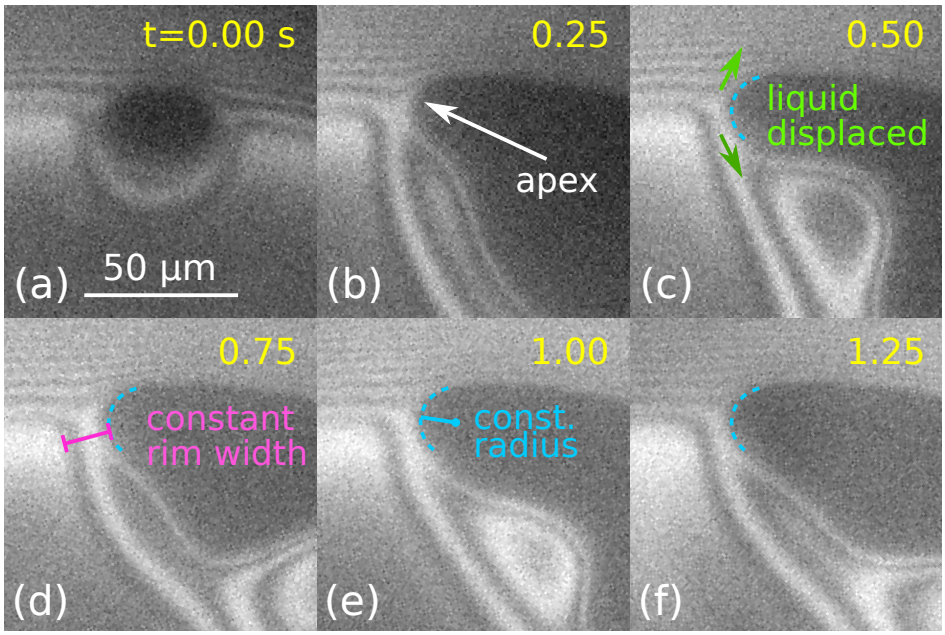

Figure 2.7: Magnified contact line region at the edge of the contact spot for the experiment shown in Fig. 2.5. After nucleation of the dry spot (a), the interference fringe pattern and thus the liquid film thickness distribution remain constant in the immediate vicinity of the apex of the contact line (b-f). The dashed circular arcs in (c-f) have a identical radius, highlighting that the contact line near the apex does not change shape.

However, these do not influence the edge dewetting speed, as they occur sufficiently far away. The azimuthal dewetting speed along the perimeter is higher for several reasons. There is relatively less liquid to displace compared to the center of the contact spot, as the film is thinnest at the edge. Moreover, approximately half of the liquid is displaced into the liquid bulk volume outside of the contact spot, which has a much smaller viscous flow resistance. Furthermore, the outwards escape of liquid does not increase the elastic nor the surface energy of the system. Therefore, the liquid rim width and height at the apex are relatively small and do not increase in time.

We have systematically measured the dewetting speed both along the perimeter of the contact spot and radially inwards as a function of the liquid film thickness. We determined the film thickness close

to the center of the contact spot. Because the liquid film thickness is essentially uniform everywhere within the contact spot (except for the region close to the edge), the exact location is immaterial. The results are presented in Fig. 2.8. Since we saw in Fig. 2.6 that $r_{cl} \sim t^{\beta}$, the dewetting speed in the radially inwards direction is not a constant but decreases as $t^{\beta-1}$. Consequently, a characteristic lengthscale or position needs to be chosen, at which to evaluate the inwards velocity. We chose the radius of the contact spot. We fitted the experimental data for $r_{cl}(t)$ with

$$r_{cl}(t) \cong \alpha t^{\beta} \,. \tag{2.20}$$

Accordingly, the contact line velocity v_{cl} at a radial distance equal to r_{cs} becomes

$$v_{cl}(r = r_{cs}) = \alpha^{\frac{1}{\beta}} \beta r_{cs}^{1-\frac{1}{\beta}} \tag{2.21}$$

which is represented by the orange rectangles in Fig. 2.8. The dewetting speed increases for thinner films. The solid lines represent the power relation $v_{\mathrm{cl,edge}} \sim h^{-3/2}$. Interestingly, the ratio between the radial and the edge dewetting speed is approximately constant for $h \leq 120\,\mathrm{nm}$.

2.5 Numerical Results

We now turn to the predictions of our numerical model presented in Sec. 2.2. For the purpose of validation we start with the axisymmetric case and compare our results with the analytical predictions of Eqs. (2.1, 2.2).

2.5.1 Axisymmetric dewetting - model validation

Figure 2.9(a-c) shows a typical time evolution of the liquid film thickness for defect-induced dewetting. For $t \leq 0.15\,\mathrm{s}$ the elastic hemisphere remains essentially undeformed and the minimum film thickness occurs on the symmetry axis at $r = 0$. For later times deformation becomes apparent and the minimum film thickness is assumed at a non-zero radial position defining the contact spot radius a. Dewetting initiates at $t_d \approx 15\,\mathrm{s}$, after which a well defined contact line is seen to propagate radially outwards. We identify the contact line position r_{cl} with the location at which $h = 1.5\,h^*$. Figure 2.9(d,e) shows the time evolution of the pressure distribution and its (negative) radial derivative.

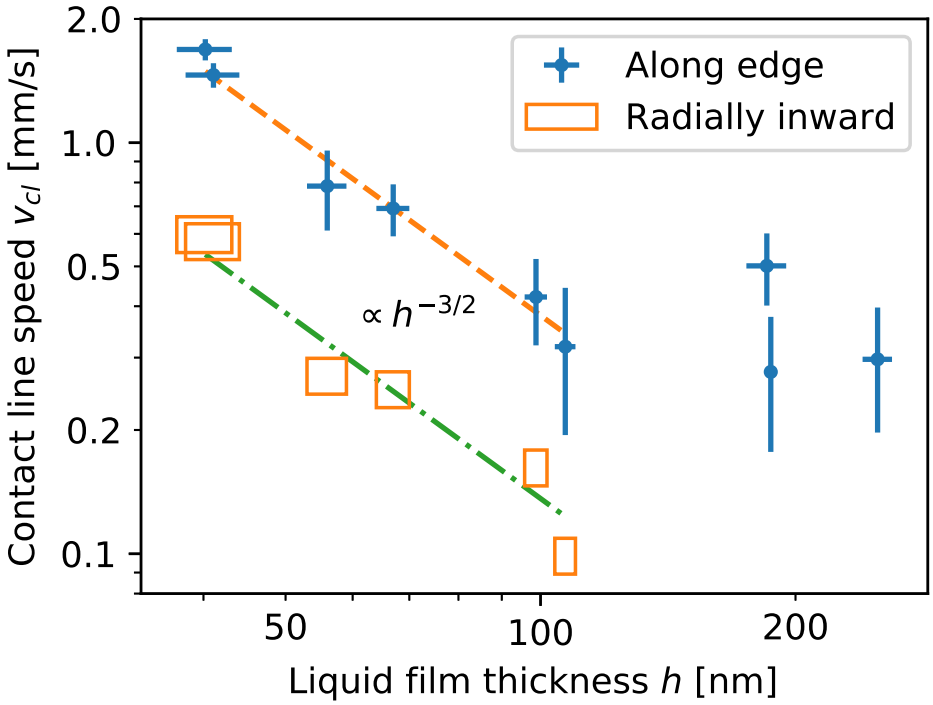

Figure 2.8: Experimental data of the azimuthal and radial dewetting speeds as a function of liquid film thickness. The ratio of contact line speed along the edge and towards the center of the contact spot appears to be approximately constant for $h \leq 120\,\mathrm{nm}$.

The pressure distribution converges to the Hertzian profile[73] with decreasing film thickness.

Figure 2.10 presents the time evolution of r_{cl} along with fits according to Eqs. (2.1, 2.2). The time t_{cs} is defined as the instant when r_{cl} reaches the edge of the contact spot for each numerical simulation. The numerical result for $(n, m) = (3, 2)$ differs significantly from the analytical solutions. This is caused by the somewhat unrealistically long range of the surface forces present in the model for $m = 2$.

We repeated the simulations using higher exponents (n, m) equal $(4, 3)$ and $(5, 4)$, which converge towards the curve corresponding to Eq. (2.2). We note that the values of n and m are especially important for dry spot nucleation at the edge of the contact spot. A value of $m = 2$ induces rapid, spontaneous dewetting and a large number of dry spots all around the perimeter. This is in contrast to the experimental observation of a low dry spot density of typically one over the entire contact spot area. Higher values of $m \geq 3$ correspond to a faster decay of the disjoining pressure isotherm with film thickness, which implies that dewetting only initiates at the introduced defect. In these cases the dry spot density in the simulation is in accordance with our experimental results.

We now investigate the dependence on the various material parameters appearing in Eq. (2.1) and compare with our numerical simulations. By differentiating Eq. (2.1) we obtain the contact line speed v_{cl}

$$\frac{\mathrm{d}}{\mathrm{d}t} r_{cl}(t) = v_{cl}(t) = \frac{3}{4} \left(\frac{|S|^5}{Y^2 \eta^3 h t} \right)^{1/4}. \tag{2.22}$$

The time t_0 required for the contact line to reach a certain radial position r_0 is

$$t_0 = \eta \left(\frac{Y^2 h r_0^4}{|S|^5} \right)^{1/3}. \tag{2.23}$$

Substituting t_0 for t in Eq. (2.22) gives the contact line speed at dry spot radius r_0

$$v_{cl}(r_{cl} = r_0) = \frac{3}{4\eta} \left(\frac{|S|^5}{Y^2 h r_0} \right)^{1/3}. \tag{2.24}$$

The liquid film thickness h is coupled with the parameters Y and $|S|$. Changing one of them will modify h at the time of dewetting as shown

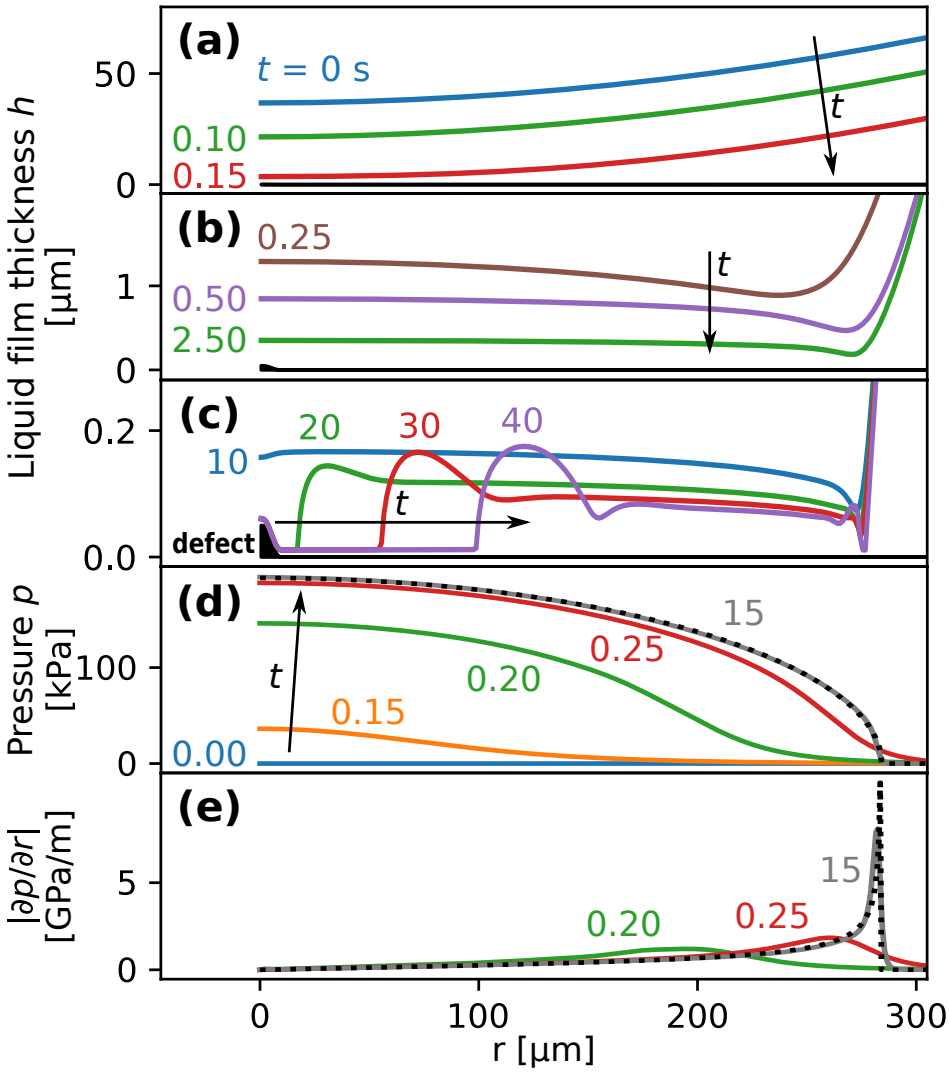

Figure 2.9: Numerical simulations of the time evolution of the (a-c) axisymmetric liquid film thickness for $R_L = 1.7\,\text{mm}$, $b_0 = 36.76\,\mu\text{m} = -b_1$, $t_c = 0.3\,\text{s}$, $\Delta h_d = 50\,\text{nm}$, $r_d = 10\,\mu\text{m}$, $|S| = 2.5\,\text{mN/m}$, $Y = 1.365\,\text{MPa}$, $\eta = 0.2646\ \text{Pa s}$, $n = 2$, $m = 3$, $h^* = 5\,\text{nm}$. Dewetting started after $t_d = 15\,\text{s}$. Distributions of (d) the pressure and (e) the pressure gradient in the liquid film for several time steps compared with the corresponding Hertzian profiles[73] (dashed lines).

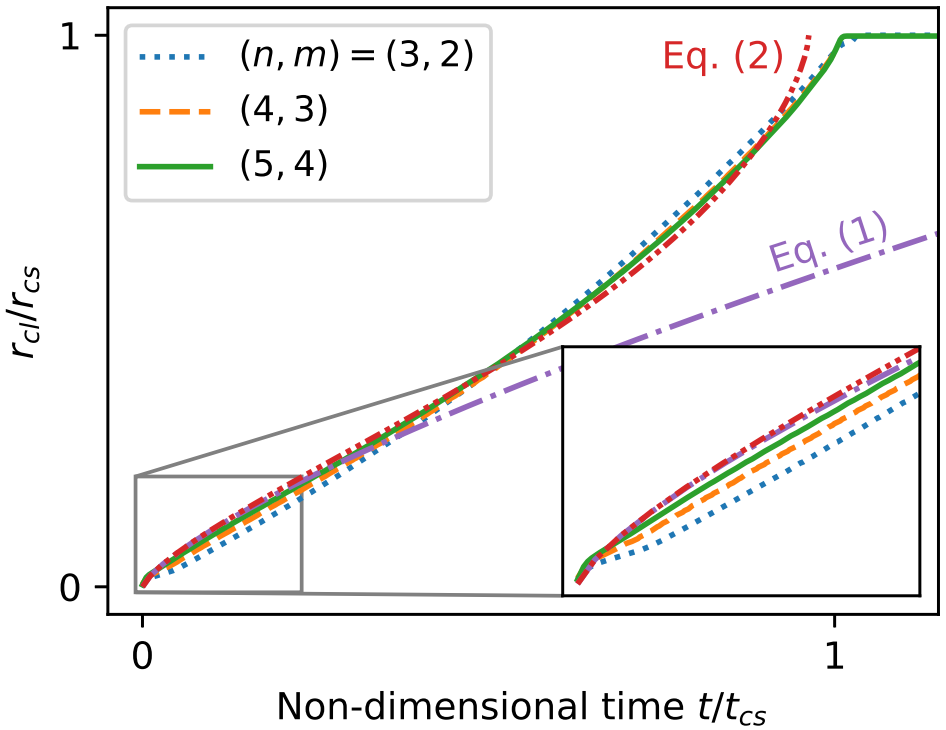

Figure 2.10: Numerical simulations of the contact line position versus time for several values of n and m. Results are compared with Eqs. (2.1) and (2.2), plotted with the dash-dotted and dash-double-dotted lines, respectively. The time t_{cs} is defined as the instant when r_{cl} reaches the edge of the contact spot for each numerical simulation.

in Fig. 2.11(a). According to Ref. [23], a dry spot will grow and initiate the dewetting process, if its radius is larger than a critical value R_{crit},

$$R_{\mathrm{crit}} \approx h^2 \frac{Y}{|S|} \,. \tag{2.25}$$

In our model, dewetting is initiated by a defect with half-width of $w_d = 5\,\mu\mathrm{m}$ when the liquid film thickness falls below a critical value h_{crit}. Assuming $R_{\mathrm{crit}} \sim w_d$, we obtain from Eq. (2.25),

$$h_{\mathrm{crit}} = \mathcal{E} \sqrt{w_d \frac{|S_{\Pi}|}{Y}} \,, \tag{2.26}$$

where $\mathcal{E}$ is a dimensionless constant. We tested the applicability of this equation in our model by investigating the relation between the average critical liquid film thickness $\langle h \rangle_{\mathrm{crit}} \equiv 2 r_{cs}^{-2} \int_0^{r_{cs}} h(r)\, r \,\mathrm{d}r$ evaluated at the time of dewetting and Eq. (2.26). Figure 2.11(b) shows the result. The solid line represents a linear fit, which indeed represents the data very well. The proportionality factor is determined to be $\mathcal{E} = 18.9$. Consequently, we can use Eq. (2.26) to eliminate h from Eq. (2.24) and obtain the following scaling law

$$v_{cl}(r_{cl} = r_0) \sim \frac{1}{r_0^{1/3} w_d^{1/6}} \frac{|S|^{3/2}}{\eta Y^{1/2}} \,. \tag{2.27}$$

Simulations were performed for different values of η, $|S_{\Pi}|$ and Y. Different values of η simply change the timescale of the dewetting process without affecting the morphology and dynamics (see Fig. 1 in the supporting information). For each set of parameters Y and $|S_{\Pi}|$, we determined the contact line speed v_{cl} at the moment when the dry spot radius reaches $r_0 = 25\,\mu\mathrm{m}$. Figure 2.11(c,d) presents the extracted values of $v_{cl}(r = r_0)$ as a function of Y and $|S_{\Pi}|$. The solid lines correspond to power laws with fitted exponents -0.505 and 1.508, respectively, which are consistent with Eq. (2.27). Therefore, v_{cl} was adjusted by multiplying it by $h^{1/3}$ to compensate for the liquid film height influence, according to Eq. (2.24).

Figures 2.9 to 2.11 provide an extensive validation of our numerical model.

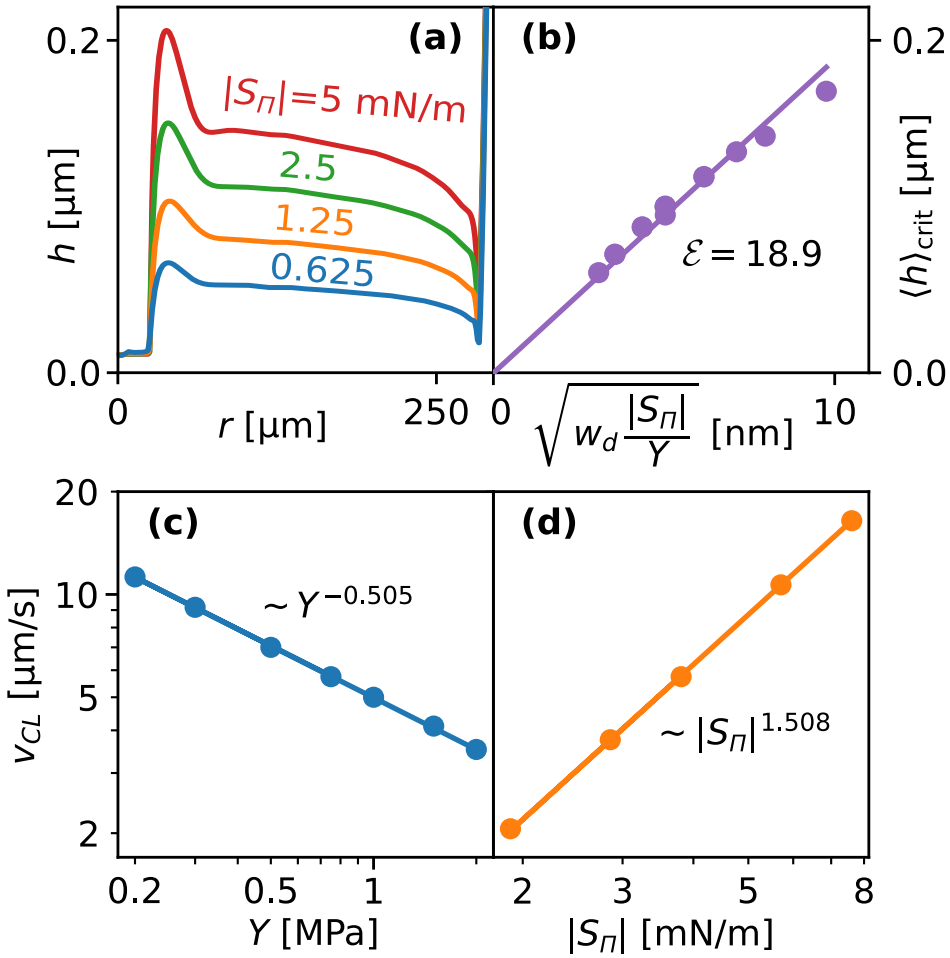

Figure 2.11: (a) Liquid film thickness profiles $h(r)$ for different values of $|S_\Pi|$ at the instant when the contact line was located at radial position $r_0 = 25\,\mu m$. (b) Average critical liquid film thickness $\langle h \rangle_{\text{crit}}$ plotted against Eq. (2.26). Solid line represents a linear fit. (c,d) Contact line speed $v_{cl}(r = r_0)$ as a function of Y and $|S_\Pi|$, respectively. Solid lines correspond to power laws with fitted exponents -0.505 and 1.508, respectively, consistent with Eq. (2.27).

2.5.2 Dry-spot nucleation at the edge of the contact spot

Three-dimensional simulations of non-axisymmetric dewetting were performed, where dry-spot nucleation was initiated by a defect at the perimeter. Figure 2.12(a-c) shows snapshots from the experiment depicted in Fig. 2.5. Figure 2.12(d-f) shows snapshots from a simulation where the dry-spot had the same radial extension as in the experiment. The simulation reproduces similar morphology and the effect of dewetting speed being higher along the perimeter. In both Fig. 2.12(c) and (f) we note that the liquid rim developed bulges near the perimeter, as indicated by the blue triangles.

In Fig. 2.13 we present the azimuthal and radial contact line displacements $s_a \equiv r_{cs}\varphi_{cl}$ and $s_r \equiv r_{cs} - r_{cl}$, respectively, for the simulation shown in Fig. 2.12(d-f). Here φ_{cl} is the azimuthal position of the azimuthal apex of the dry spot as indicated in Fig. 2.12(b). The solid lines correspond to power law relations $s \sim (t-t_0)^{\zeta}$. The exponent found for the azimuthal motion matches very well with the early-time behaviour ($\zeta = 0.65$) in Fig. 2.6. However, due to computational cost, the simulation did not reach the stage of constant azimuthal line speed observed in Fig. 2.6. The scaling exponent for the radial dynamics also matches well with the experimental value in Fig. 2.6.

2.6 Conclusion

We have studied the dewetting of thin liquid films confined between a soft solid hemisphere and an elastomeric layer. For the most frequent case of dry-spot nucleation occurring at the perimeter of the contact spot, we found the contact line speed to be significantly higher in the azimuthal than in the radial direction. The spontaneous formation of dry spots is highly sensitive to the local film thickness h and exhibits a much higher rate and probability in regions of lower h, which predominantly occur near the margin of the contact spot. We found that the height of the dewetting rim in the azimuthal direction along the perimeter of the contact spot remains essentially constant, whereas it grows both in height and width for motion in or against the radial direction. Moreover the film thickness is lowest at the edge of the contact spot. Both these effects account for the observed strong

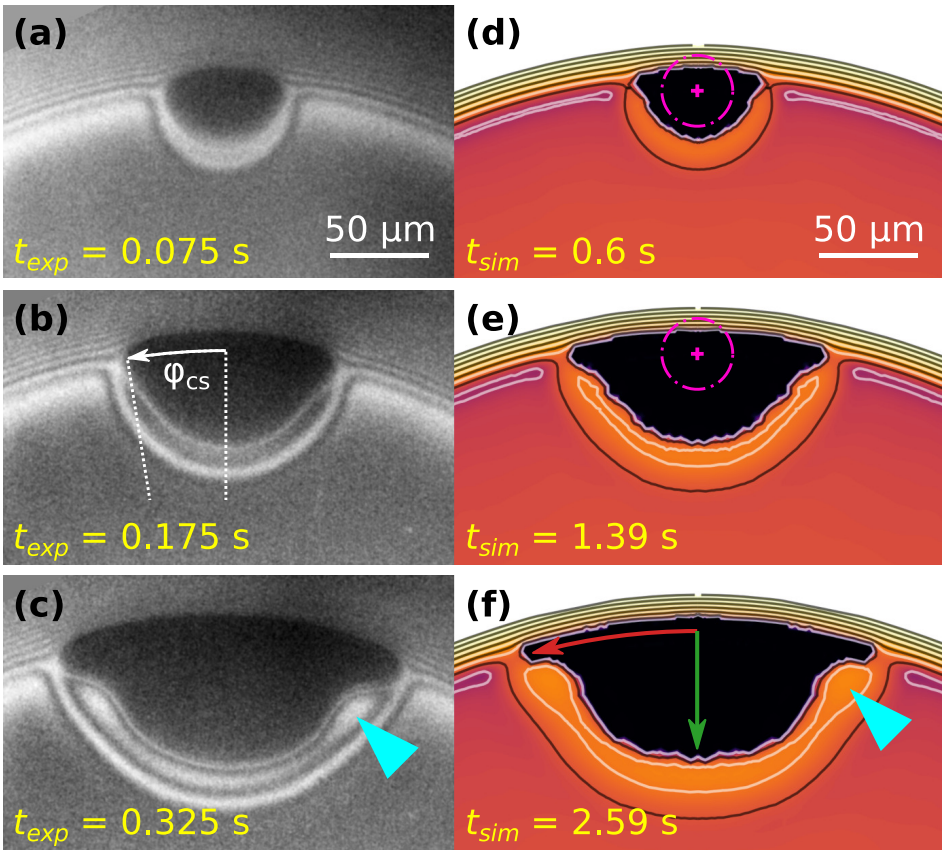

Figure 2.12: A comparison of (a-c) experimental and (d-f) simulated morphologies of dry spots that nucleated on the perimeter of the contact spot. Blue triangles in (c,f) indicate local maxima observed in the dewetting rim near the edge of the contact spot. In the simulations we used $n = 5$, $m = 4$, $S_{\Pi} = 12$ mN/m, $h^* = 10$ nm. The purple dash-dotted circle in (d,e) indicate the radius of the defect used to initiate dewetting.

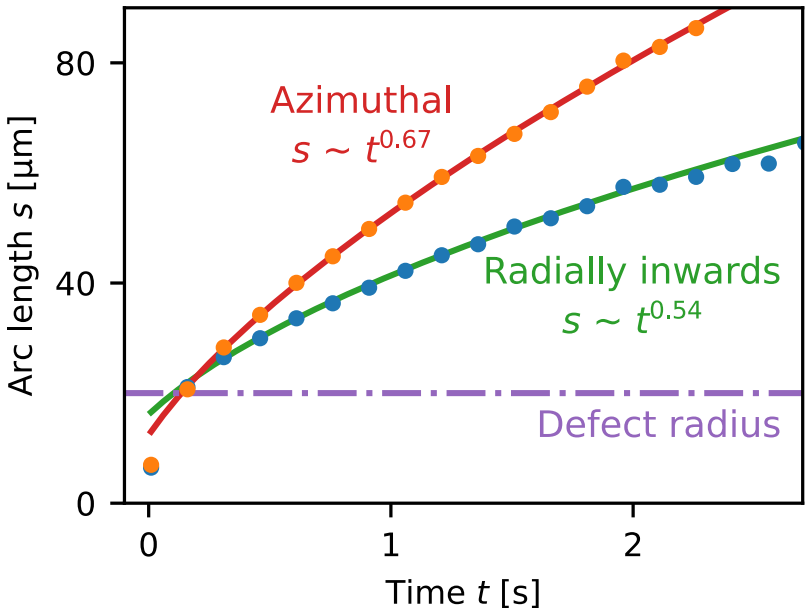

Figure 2.13: Azimuthal (orange squares) and radial (blue circles) contact line displacements s_a and s_r extracted from the simulation along the lines indicated with arrows in Fig. 2.12(f). Solid lines correspond to power law relations $s \sim (t - t_0)^{\zeta}$. The purple line indicates the radius of the defect used to initiate dewetting.

anisotropy of the contact line speed for non-axisymmetric dewetting.

We developed a fully coupled three-dimensional numerical model of the dewetting process based on a disjoining pressure formalism. We successfully validated our model using the available analytical models for axisymmetric dewetting. The model reproduces the morphology of the dewetting spots as well as their anisotropic growth dynamics very well.

The results we found for a liquid perfluoropolyether are representative of the behaviour of water and aqueous polymer solutions,[12,13] which are relevant for biological systems.

Acknowledgement

I would like to thank Jesse Kwaks for his help with the experiments and analysing experimental results.

Appendix: Arbitrary Lagrangian-Eulerian model

Model description

In order to investigate the effect of soft elastomeric substrates, we replaced the Reynolds equation (2.8) with the Stokes equation

$$0 = -\nabla p + \eta \nabla^2 \mathbf{v} \tag{2.28}$$

and employed an arbitrary Lagrangian-Eulerian (ALE) scheme to capture the deformation of the substrate. Here, $\mathbf{v}$ is the hydrodynamic velocity vector. We assume the soft substrate to have a flat, rigid support parallel to the $z = 0$ plane, which moves according to

$$z_{\mathrm{sup}}(t) = b_0 + (b_1 - b_0)\, \mathrm{f_{hs}} \left[2\frac{t}{t_c} - 1 \right]. \tag{2.29}$$

Then Eq. (2.16) is replaced by

$$z_s(r,t) = u_z^{(s)}(r,t) + z_0 + z_d(r)\,, \tag{2.30}$$

where $u_z^{(s)}(r,t)$ is the displacement of the liquid-substrate interface and z_0 is a constant. The BC at the symmetry axis $r = 0$ is

$$u_r = 0\,, \quad \frac{\partial u_z}{\partial r} = 0 \quad \text{and} \quad \frac{\partial p}{\partial r} = 0\,. \tag{2.31}$$

At the elastomer-liquid interface $z = z_e(r,t)$ the BCs are

$$v_i = v_{e,i} = \frac{\partial u_i}{\partial t}\,, \tag{2.32}$$

$$\sigma_{ij} n_i = \sigma_{ij}^{(\text{liquid})} n_i\,, \tag{2.33}$$

where $\sigma_{ij}^{(\text{liquid})}$ is the stress tensor, defined as

$$\sigma_{ij}^{(\text{liquid})} = \mu \left(\frac{\partial v_i}{\partial x_j} + \frac{\partial v_j}{\partial x_i} \right) - p\delta_{ij}\,. \tag{2.34}$$

The BC at the outlet is

$$\sigma_{ij}^{(\text{liquid})} = -p_{\text{out}}\delta_{ij}\,, \tag{2.35}$$

where p_{out} is automatically adjusted to prevent backflow.

Impact of substrate elasticity

In Fig. 2.14 we compared simulations for a rigid and soft substrate. In both cases, the film thickness in the center scales asymptotically as $h(0,t) \sim t^{-1/2}$. However, Fig. 2.14 shows that the liquid film thickness is more non-uniform for rigid substrates. In the latter case, h is thicker at the center and thinner at the edge of the contact spot. The higher degree of uniformity for soft substrates is consistent with the experimental observation that the grayscale value of the interference pattern does not vary significantly in the contact spot [see e.g. Fig. 2.1(d)]. The displacement of the substrate support was kept constant at 45 µm in the simulations shown in Fig. 2.14, resulting in a 19% larger force for the rigid substrate. Moreover, the contact spot radius is slightly larger for the soft substrate.

While the ALE simulations more faithfully represent the experimental geometry, they imply a higher computational cost. Introduction of a non-zero disjoining pressure caused convergence issues such that simulations of dewetting unfortunately were not possible.

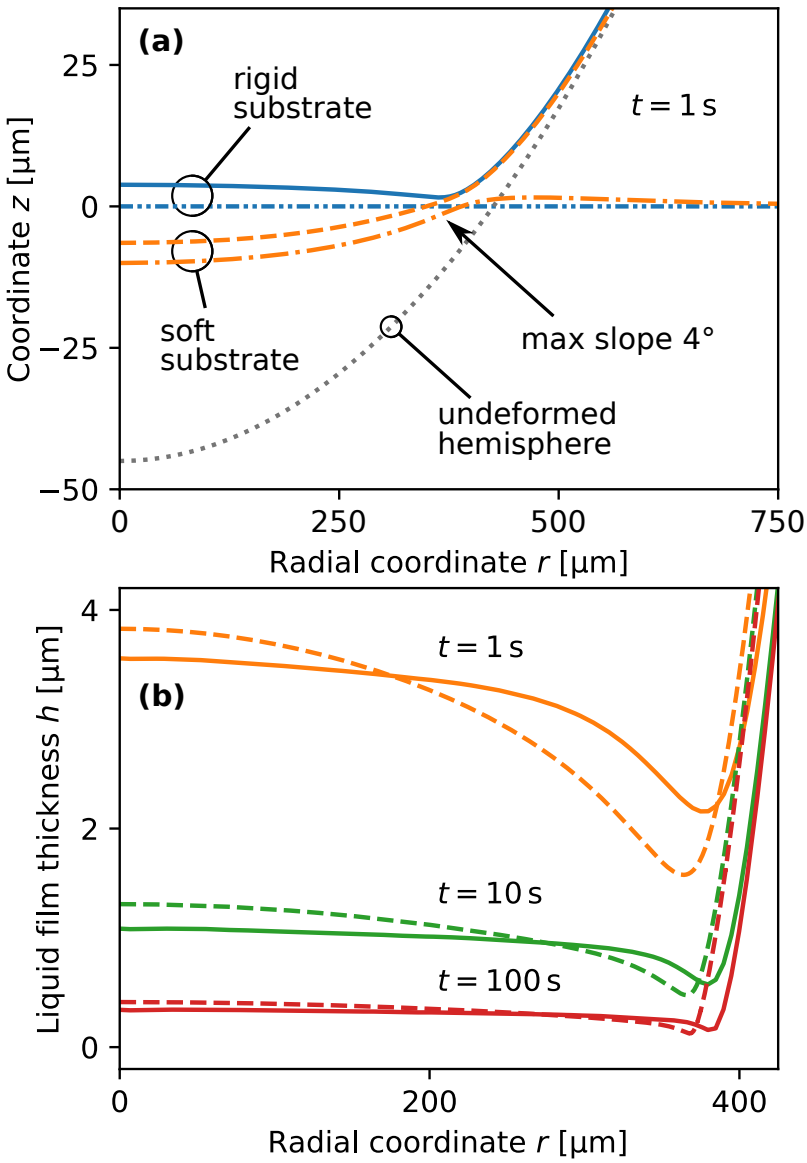

Figure 2.14: (a) Deformed interface profiles at time $t = 1\,\mathrm{s}$ for simulations performed with a rigid and soft substrate, with no disjoining pressure $S_\Pi = 0$, $R_L = 2\,\mathrm{mm}$, $b_0 = 45\,\mu\mathrm{m} = -b_1$, $Y = 100\,\mathrm{kPa}$, $t_c = 0.5\,\mathrm{s}$, $\eta = 0.2646\,\mathrm{Pa\,s}$. (b) Film thickness profiles for several times. Dashed and solid lines correspond to rigid and soft substrates, respectively.

Chapter 3

Escape dynamics of liquid droplets confined between soft interfaces: non-inertial coalescence cascades

3.1 Introduction

The behavior of liquid confined between solids, of which at least one is soft and elastomeric, is important in a number of technological applications such as aquaplaning,[3–13] tribology, printing[80–82] and adhesion.[14–19] The stability of liquid films is highly desirable in tribological applications such as contact lenses and cartilage joints, where direct solid on solid contact would induce wear and frictional heating. However, the presence of low viscosity liquids such as water is generally a nuisance in the context of the adhesive joining of two surfaces, as liquids are essentially incompressible and thus prevent close contact and moreover reduce the effective Hamaker constant by up to a factor of 10.[63] For achieving maximum adhesion in wet environments the complete removal of liquid between the contacting materials is beneficial. However, in solid-liquid-solid dewetting complete removal of liquid is rare, i.e. temporarily trapped droplets are very frequently observed in the contact spot.[79] The focus of this manuscript is on the mechanism and dynamics of the expulsion of these droplets.

Brochard and coworkers have investigated the stability of uniform

thin liquid films between soft solids and derived a scaling law for the growth dynamics of a circular dry spot.[23,24,72] They also presented a theory of spinodal dewetting of ultra thin films at soft interfaces.[20] Sneddon showed that the shape of an inclusion characterized by a constant pressure in an incompressible elastic medium is an ellipse, except very near the perimeter of the inclusion.[83] Based on his work, Martin *et al.* showed that the shape of stationary droplets confined between soft elastic solids is (semi-)ellipsoidal and that the droplet footprint radius a_d scales as the square of the center height h_d of the droplet.[79]

This manuscript deals with the *motion* of droplets confined between a flat elastomer layer and an elastic hemisphere that is pressed into the layer. The non-uniform contact pressure gives rise to a pressure gradient in the contact zone, that drives the droplets radially outward. Our key finding is that at the perimeter of the contact area they merge with the outer liquid either completely in a single coalescence event or in a cascade of sequential partial coalescence events. We give an overview of various systems for which full and partial coalescence effects have been observed in the past in section 3.6 and discuss their relevance to our findings. To gain insight into this experimental observation, we performed fully-coupled three-dimensional numerical simulations, which reproduce the droplet shape evolution very well. Moreover, we developed an analytical model that reproduces the scaling of the contact time of the droplet with the outer liquid upon coalescence well.

3.2 Experimental setup

Figure 3.1(a) shows a sketch of the experimental geometry. An elastomer half-sphere is pressed onto a flat layer of the same material with liquid confined in between. The elastomer used was a silicone-based, heat-curable, two-component polymer resin (Smooth-On, Encapso K, Young's modulus $Y = 1.365$ MPa). The liquid is a perfluoropolyether (Solvay, Fomblin Y LVAC 14/6, average molecular weight 2500, viscosity $\mu = 0.2646$ Pa s). The flat elastomer layer is attached to a glass substrate. The dynamics of the liquid is viewed from beneath the substrate with an inverted microscope. Details of the setup, the experimental procedures as well as the liquid and solid material properties

are provided in Ref. [84].

Figure 3.1(b) shows a snapshot of the contact spot shortly after a dry spot nucleation event took place. Light reflected from the silicone-liquid and liquid-hemisphere interfaces gives rise to interference fringes [Fig. 3.1(b-d)], which allow to determine the film thickness distribution $h(x, y)$ of the liquid. When dewetting starts, the liquid film thickness is essentially uniform throughout the contact spot. At this instant the liquid film thickness near the center of the contact spot was $104 \pm 2\,\mathrm{nm}$ and decreasing at a rate of $2.4\,\mathrm{nm/s}$ as[24] h evolves in time according to $t^{-1/2}$. Figure 3.1(c) visualizes the growth process of the dry spot, which is accompanied by a pronounced instability of the dewetting rim. This leads to the formation of liquid threads that subsequently break up into droplets. Due to the radially increasing pressure gradient in the contact spot, droplets move radially outwards, the faster the closer they are to the edge of the contact spot.

According to Ref. [85], silicone polymers may still contain uncrosslinked chains after curing, which can be extracted by immersing the elastomer in a good solvent and subsequently deswelling it. We swelled different samples in toluene, p-xylene, ethyl acetate and 2-propanol for several days, refreshing the solution daily, then used a 1:1 mix by volume of the good solvent and ethanol for one day and pure ethanol for another day to deswell the samples. After this procedure we noted a mass loss of $(22.5 \pm 0.1)\%$ in all cases. However, all solvents except 2-propanol induced partial disintegration or debonding of the elastomer layer. Consequently, we only used 2-propanol as the good solvent. The mass loss observed for our material system is considerably larger than that reported for Sylgard 184 in Ref. [85]. Nevertheless our layers remained optically clear and the surface remained smooth and flat.

3.3 Analytical Model

3.3.1 Movement of droplets at soft interfaces

We consider a case where droplets occur after dewetting and aim to derive a simple description of their motion induced by the pressure gradient inside the contact spot. We define the elastocapillary length as $L_{ec} = |S|/Y$, where $S \equiv \gamma_{ee} - 2\gamma_{el}$ is the spreading parameter.

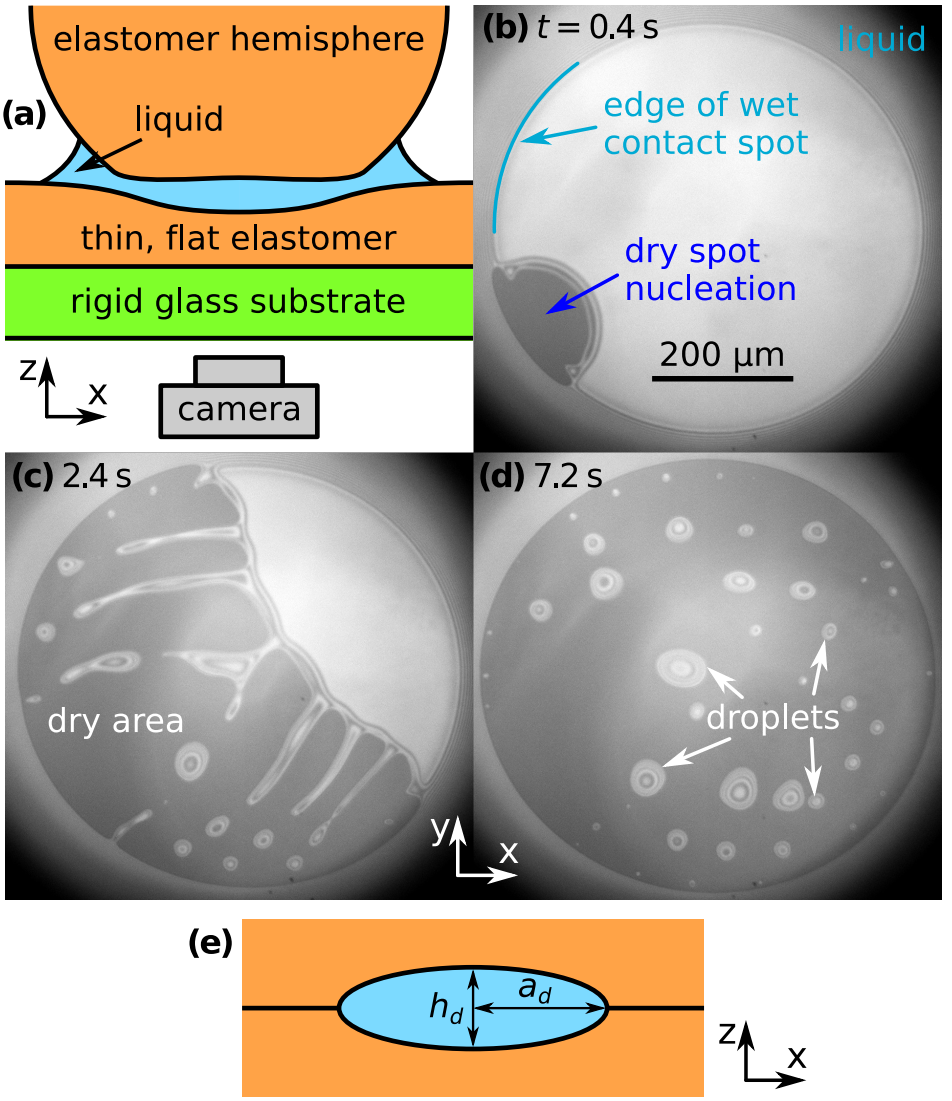

Figure 3.1: (a) Side-view sketch of the experimental geometry. (b-d) Microscope images of dry spot nucleation and dewetting in the wet contact zone between an elastic half-sphere and a flat elastic layer. Frequently droplets are created due to an instability of the dewetting rim. (e) Cross-sectional side-view sketch through a droplet with the maximum thickness h_d and footprint radius a_d indicated.

Here, γ_{ee} is the energy density of two identical elastomer surfaces in contact, and γ_{el} the elastomer-liquid surface energy density. Martin *et. al.* considered the conformation of a droplet confined by soft, elastic interfaces.[79] When L_{ec} is much smaller than the droplet footprint radius a_d, then a droplet squeezed between a rigid plane and a soft solid in a region of uniform pressure will have the shape of a flat half-ellipsoid, with height[79]

$$h_d = \sqrt{\frac{6}{\pi} L_{ec} a_d} \quad \text{(half-ellipsoid)}. \tag{3.1}$$

When considering a droplet between two soft solids, the derivation is analogous to that in Ref. [79], resulting in an additional prefactor of $\sqrt{2}$

$$h_d = 2\sqrt{\frac{3}{\pi} L_{ec} a_d} \quad \text{(full ellipsoid)}. \tag{3.2}$$

We used Eq. (3.2) to estimate the value of S from the observed droplet geometry. From our experiments we found $S = (-8 \pm 2)$ mN/m, corresponding to $L_{ec} = (6 \pm 2)$ nm. If the interfacial pressure distribution is not uniform, the droplet will move towards regions of lower pressure to minimize the elastic deformation energy. The speed of its motion will be determined by the balance of the viscous dissipation rate in the liquid and the elastic energy gain rate. Assuming that the droplet maintains a constant ellipsoidal shape, that the deformations are small and that the liquid flow inside the droplet can be determined from the Reynolds equation, an estimate of the droplet speed can be calculated.

The z-positions of the liquid-solid interfaces of the droplet in cylindrical coordinates (with origin at the droplet midpoint) are conforming to the ellipsoid shape

$$z_d(r) = \pm \frac{h_d}{2} \sqrt{1 - \frac{r^2}{a_d^2}}\,, \tag{3.3}$$

where h_d is the thickness of the droplet. The surface energy density u_A (work per unit area performed by pressure displacing the elastic surface by δ) is

$$u_A = \frac{1}{2} P_f \delta\,, \tag{3.4}$$

where P_f is the local pressure. The energy U_d needed to introduce a droplet at an interface between two elastomers is

$$U_d = 2\int_0^{a_d} \frac{1}{2} P_f z_d(r)\, 2\pi r \,\mathrm{d}r = \frac{\pi}{3} a_d^2 h_d P_f \,. \tag{3.5}$$

If the droplet is moving radially with a velocity v_d in a contact spot with pressure distribution $P_f(r)$ and radial gradient $\Omega_f(r) \equiv \frac{\partial P_f}{\partial r}$, the energy gain rate is

$$\frac{\partial U_d}{\partial t} = \frac{\partial U_d}{\partial r}\frac{\partial r}{\partial t} = \frac{\partial U_d}{\partial r} v_d = \frac{\pi}{3} a_d^2 h_d v_d \Omega_f \,. \tag{3.6}$$

Equating this expression with the total energy dissipation rate allows us to derive the droplet velocity. Following Ref. [24] the viscous dissipation rate $\dot{U}_\mu$ is $\mu(v_d/h_d)^2$ per unit volume. Thus the energy dissipation rate is approximately

$$\dot{U}_\mu \sim \mu \left(\frac{v_d}{h_d}\right)^2 \frac{2}{3}\pi a_d^2 h_d = \frac{2}{3}\pi\mu \frac{v_d^2}{h_d} a_d^2 \,. \tag{3.7}$$

Equating Eqs. (3.7) and (3.6) yields an estimate for the radial droplet velocity

$$v_d(r) \sim \frac{2h_d^2}{\mu}\frac{\partial P_f}{\partial r} = \frac{24|S|a_d}{\pi\mu Y}\Omega_f \,, \tag{3.8}$$

which is proportional to the contact pressure gradient Ω_f.

3.3.2 Coalescence with outer bulk liquid

Droplets move towards the edge of the contact spot with the velocity $v_d(r)$ given by Eq. (3.8). Assuming that after the commencement of coalescence with the outer bulk liquid, the back of the droplet keeps moving with a constant velocity, the coalescence time Δt can be estimated as

$$\Delta t \approx \frac{2a_d}{v_d} \sim \frac{\pi\mu Y}{12|S|}\left(\frac{\partial P_f}{\partial r}\right)^{-1}\Bigg|_{r=r_{cs}-a_d} . \tag{3.9}$$

Assuming a Hertzian pressure distribution inside the contact spot[73]

$$P_{\mathrm{H}}(r) = P_0\sqrt{1-\frac{r^2}{r_{cs}^2}} \,, \tag{3.10}$$

with $P_0 \equiv 2r_{cs}Y/\pi R_L$ being the maximum pressure at the center, Eq. (3.9) becomes

$$\Delta t_{\mathrm{H}} \sim \frac{\pi^2 R_L \mu}{24|S|} \frac{\sqrt{(2-\beta_d)\beta_d}}{1-\beta_d}\,, \tag{3.11}$$

where we introduced the parameter $\beta_d \equiv a_d/r_{cs}$. For small β_d Eq. (3.11) is approximately equal

$$\Delta t_{\mathrm{H}} \sim \frac{\pi^2 R_L \mu}{24|S|} \sqrt{2\frac{a_d}{r_{cs}}}\,. \tag{3.12}$$

The JKR model[86] more accurately represents our system, as it additionally considers the surface energy of adhesion. For a JKR pressure distribution

$$P_{\mathrm{JKR}}(r) = P_{\mathrm{H}}(r) + P_1 \left(1 - \frac{r^2}{r_{cs}^2}\right)^{-1/2}\,, \tag{3.13}$$

where $P_1 \equiv -\sqrt{4|S|Y/\pi r_{cs}}$, we find

$$\Delta t_{\mathrm{JKR}} \sim \Delta t_{\mathrm{H}} \left[1 + \frac{\frac{R_L}{r_{cs}}\sqrt{\frac{\pi|S|}{r_{cs}Y}}}{(2-\beta_d)\beta_d}\right]^{-1}\,. \tag{3.14}$$

In the limit of $\beta_d \to 0$ Eq. (3.14) reduces to

$$\Delta t_{\mathrm{JKR}} \sim \frac{\mu}{6}\sqrt{\frac{Y}{2}} \left(\frac{\pi a_d}{|S|}\right)^{3/2}\,. \tag{3.15}$$

We note that both the Hertzian and the JKR pressure profiles have an unphysical singularity of Ω_f at the edge of the contact spot. Both models do not represent accurately the pressure distribution around a contact line at a lengthscale equal to the elastocapillary length L_{ec}, which is approximately 10 nm for our material system. Since the droplet diameters we consider are typically a factor of thousand larger, the pressure profiles are expected to provide a suitable approximation.

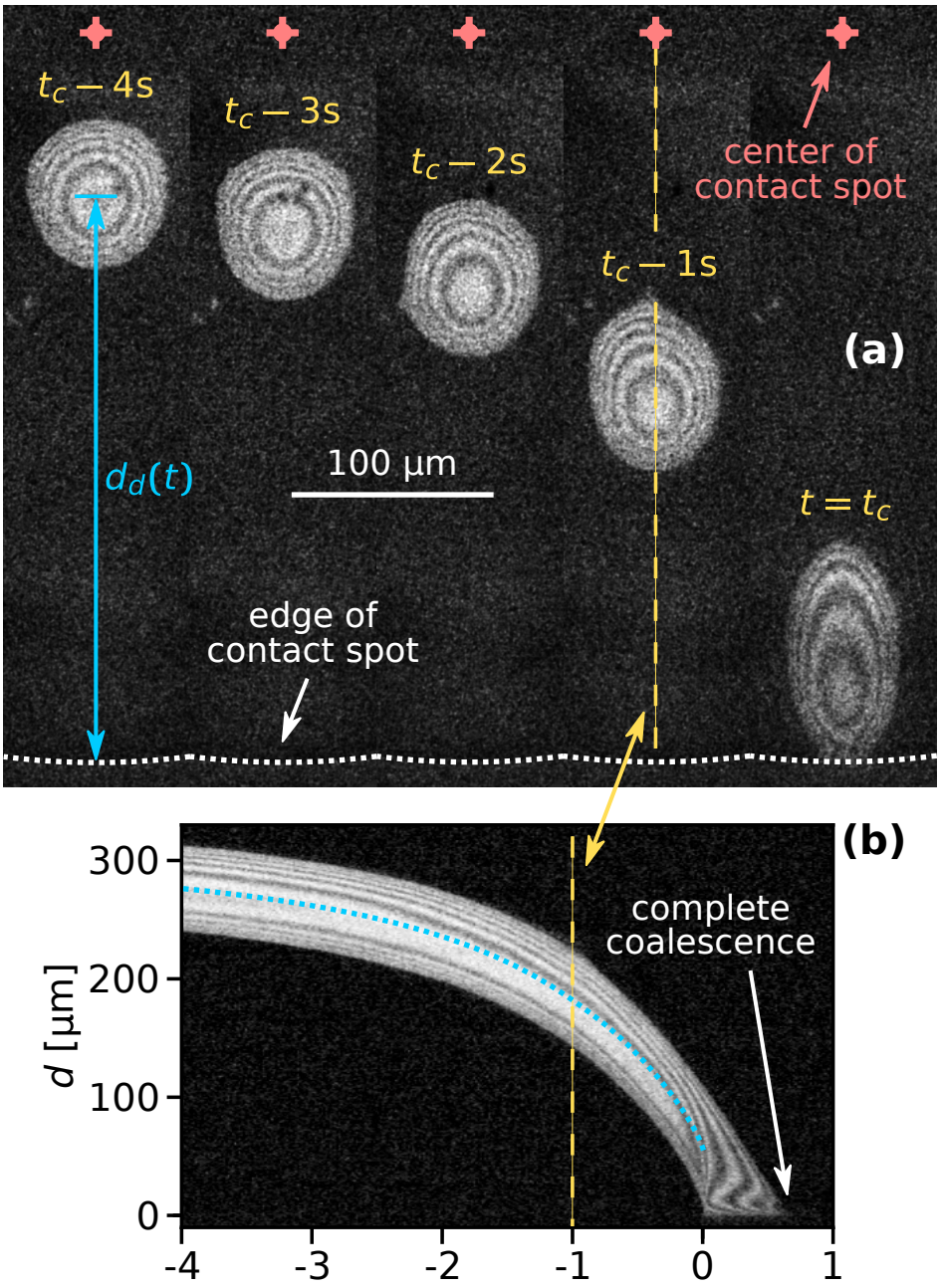

Figure 3.2: (a) Microscope images of a droplet moving towards the edge of the contact spot. (b) Time evolution of the radial intensity profile $I_c(d,t)$ through the center of the droplet visible in (a) which coalesces completely. The dashed lines both indicate $I_c(d, t - t_c = 1s)$.

3.4 Experimental Results

3.4.1 Droplet motion

Figure 3.2(a) shows microscope images of a droplet moving towards the edge of the contact spot. The red crosses denote the center of the contact spot. The white dotted line denotes the edge of the contact spot. The yellow dashed line is the centerline trajectory of the droplet in the radially outward direction. In Fig. 3.2(b), the time evolution of the radial intensity profiles $I_c(d,t)$ through the center of the escaping droplet [dashed line in (a)] is visualized. The ordinate $d \equiv r_{cs} - r$ quantifies the radial distance to the edge of the contact spot. The blue dotted line in Fig. 3.2(b) indicates the position of the midpoint of the droplet $d_d(t)$ in time. Its slope $|\dot{d}_d(t)|$ is equal to v_d.

Figure 3.3 shows the correlation between the droplet velocity v_d and the local pressure gradient. The droplet speed v_d was determined by tracking the radial position of the center of the droplet - defined as halfway between the front and back of the droplet - in time. The pressure gradient is determined from the theoretical JKR pressure profile evaluated at the droplet center location. Right after their formation droplets usually have an irregular shape. The first datapoint for each curve in Fig. 3.3 corresponds to the moment when the droplet footprint has relaxed to a round shape. The last datapoints correspond to the frames right before coalescence with the outer bulk liquid.

The velocity profile of non-cascading droplets is generally linearly proportional to the local pressure gradient before coalescence, consistent with the behavior expected on hydrodynamic grounds. Two droplets that were observed to cascade only once also moved with a velocity proportional to $|\Omega_f|$ throughout most of their lifetime. In contrast, all droplets which cascaded at least twice exhibited a qualitatively different behavior. These droplets initially moved one to two orders of magnitude slower than the velocity predicted by the hydrodynamic model. Some even show a non-monotonic behavior, i.e. an initial slow-down and subsequent acceleration.

We fitted the velocity vs. pressure gradient curves in Fig. 3.3 with linear fit functions of slope $\psi \equiv |\partial v_d / \partial \Omega_f|$. In Fig. 3.4 we present the slopes ψ of these fit functions for the single- and non-cascading droplets as a function of droplet size a_d (crosses). According to Eq. (3.8), the slope $\psi = 24|S|a_d/(\pi\eta Y)$ is proportional to a_d. The gray solid line in

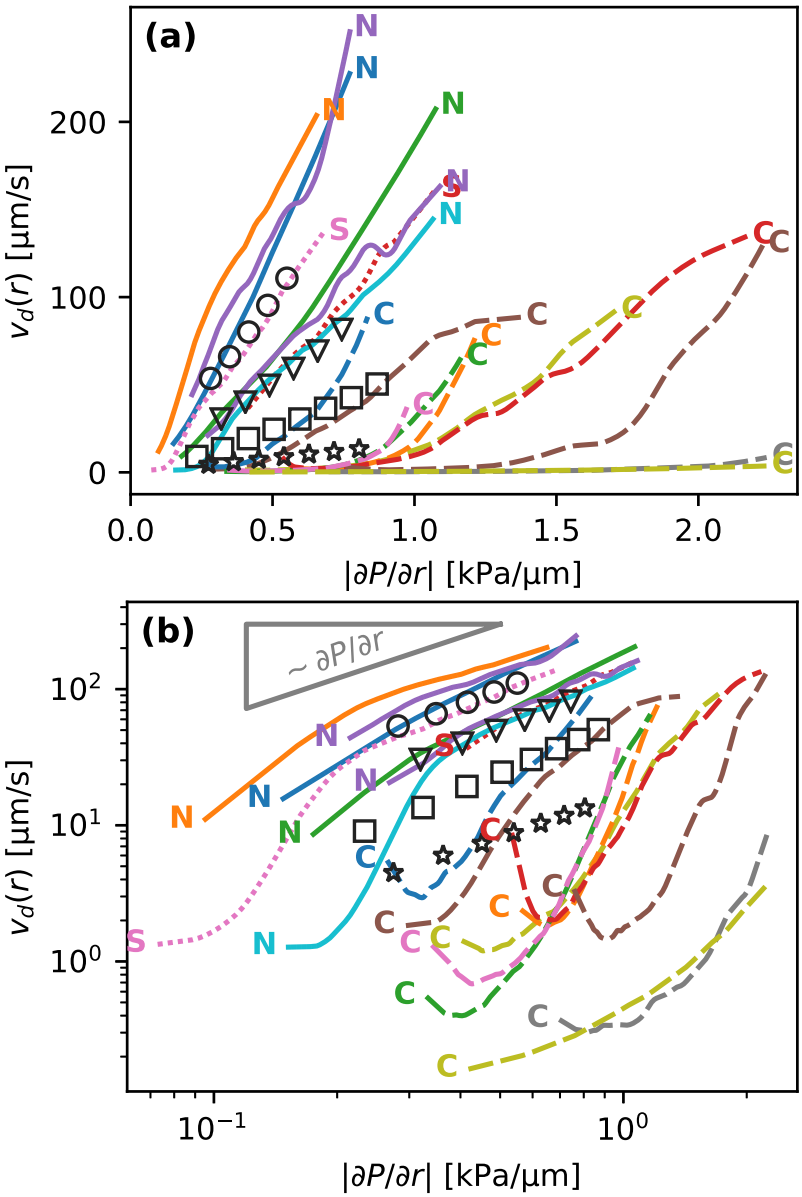

Figure 3.3: Droplet velocity v_d plotted against the pressure gradient at the droplet center using (a) linear and (b) logarithmic axes. Non-cascading droplets (solid lines) are marked with 'N". Droplets that cascaded once (dotted lines) or more than once (dashed lines) are labeled with 'S' or 'C', respectively. The open black symbols correspond to typical numerical results.

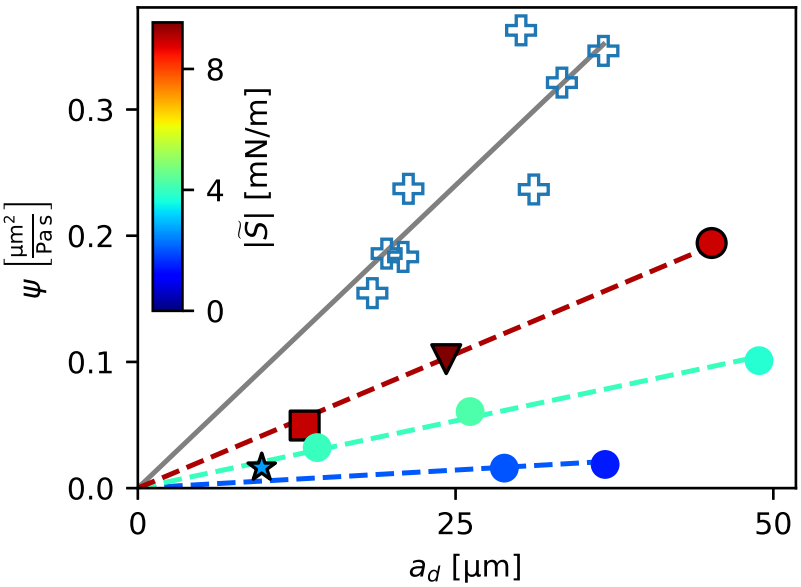

Figure 3.4: Slope ψ of the velocity-pressure gradient curves shown in Fig. 3.3(a) for single- and non-cascading droplets. Open crosses represent experiments. Filled symbols represent numerical simulations, with their color indicating the value of the parameter $|\widetilde{S}|$, to be discussed in Section 3.5. Filled symbols with black edges correspond to the numerical results in Fig. 3.3. Lines represent linear correlations $\psi \sim a_d$.

Fig. 3.4 is a linear fit, which represents the experimental data well.

3.4.2 Droplet coalescence

The time $t = t_c$ in Fig. 3.2(a) corresponds to the moment of first contact between the droplet and the outer bulk liquid. The coalescence process of radially moving droplets with the bulk liquid outside of the contact spot can proceed in a continuous or discontinuous fashion. Figure 3.5 contrasts the two observed behaviours of either complete, continuous or partial, discontinuous coalescence. In Fig. 3.5(a-i), a droplet makes contact and continuously remains in contact with the outer liquid until it is entirely absorbed. In Fig. 3.5(j-r), the liquid bridge connecting the droplet and outer liquid displays a non-monotonic behaviour. It initially grows [Fig. 3.5(k,l)] then shrinks [Fig. 3.5(m)] and eventually disintegrates [Fig. 3.5(n)]. This cascading behaviour can occur multiple times during the lifetime of a droplet. Up to nine consecutive cascades were observed for a single droplet.

Figure 3.6(a) shows a case where the droplet does not coalesce completely, but a much smaller droplet appears in proximity to the edge of the contact spot. Figure 3.6(b) shows a plot of the radial centerline intensity profiles $I_c(d, t)$ for a droplet cascading six times. Figure 3.6(c) compares the time history of the droplet footprint area of a non-cascading droplet and one that cascades five times. The latter shows a pronounced staircase-like morphology with a relatively uniform area reduction ratio $\zeta_n \equiv A_n/A_{n-1}$. Here, A_{n-1} and A_n denote the droplet footprint areas before and after its n-th cascade, respectively.

Figure 3.7(a) shows systematic experimental data of the area reduction ratio ζ_n of droplets undergoing their n-th cascade. After their first cascade most droplets become 2 to 6 times smaller. However, predominantly larger droplets (blue circles) sometimes produce secondary droplets that are more than 10 times smaller. Figure 3.7(b) shows the correlation between the area of a droplet A_{n-1} right before the n-th cascade and its contact time Δt_n, defined as the time from the start of coalescence to pinch-off, as indicated in Fig. 3.6(b). Larger droplets remain in contact with the outer bulk liquid for a longer time during a single cascade. The dashed and solid black lines and the dotted grey line represent Eqs. (3.11), (3.14) and (3.15), respectively. The black dots represent experiments using 2-propanol-treated samples,

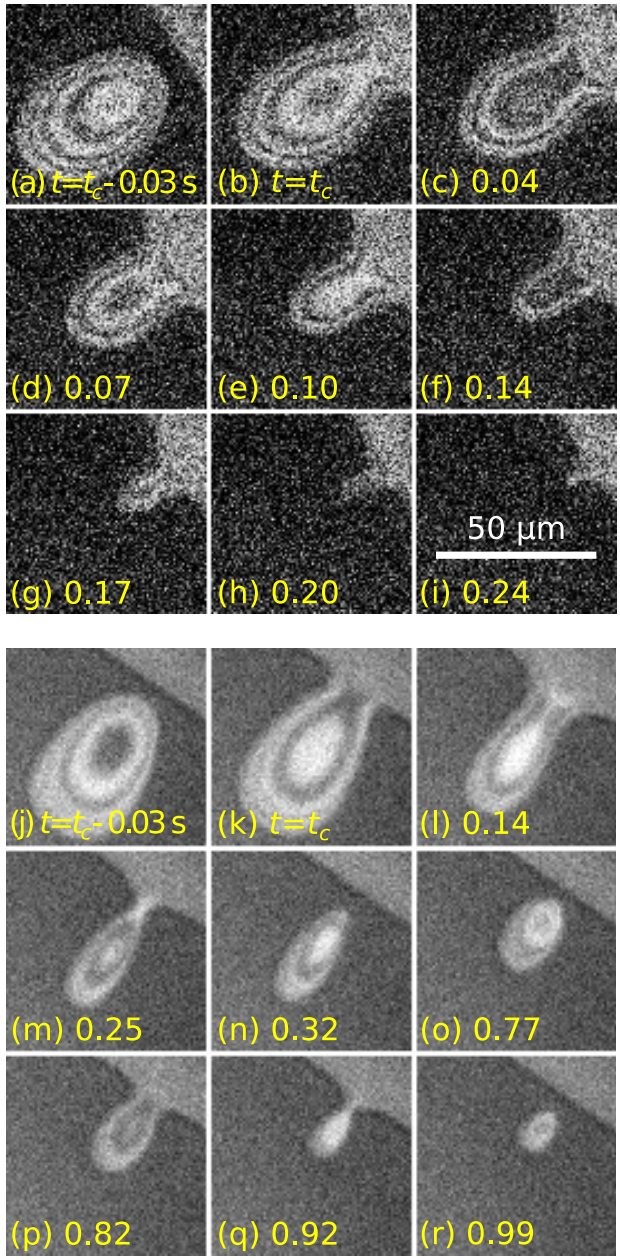

Figure 3.5: The coalescence of moving droplets with the bulk liquid outside of the contact spot can proceed in a continuous (a-i) or discontinuous (j-r) fashion. The indicated time increments are given relative to the frames (b,k) where coalescence started. The scale bar in (i) applies to all images.

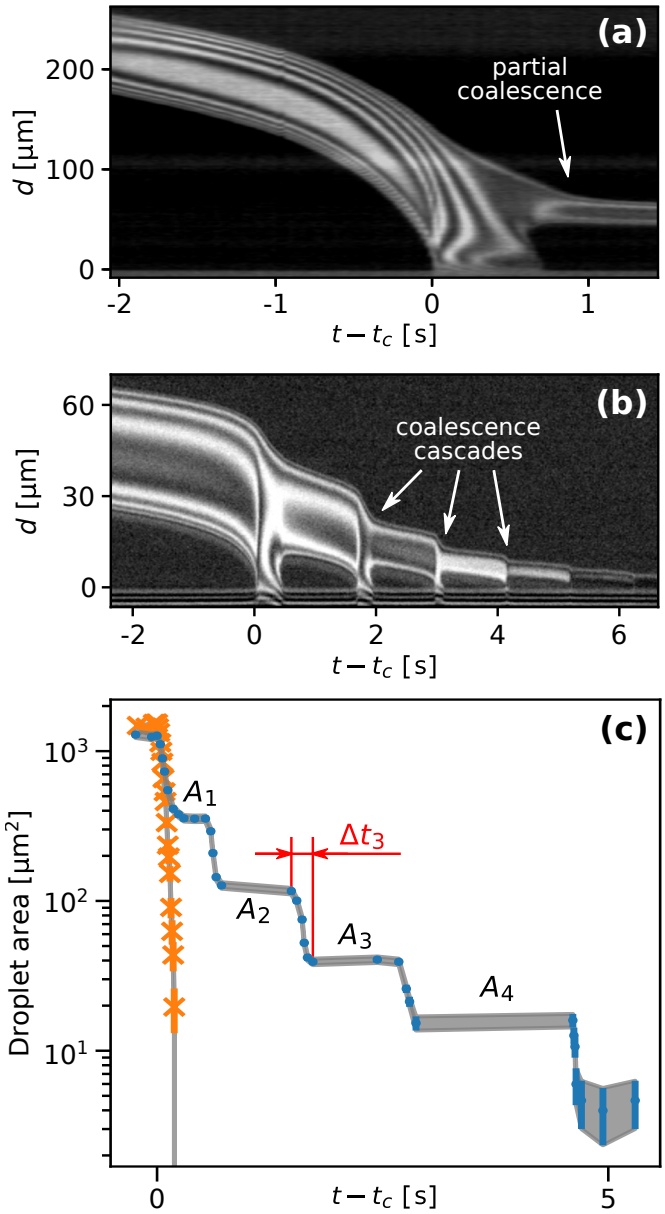

Figure 3.6: Plot of the radial centerline intensity profiles $I_c(d,t)$ for a droplet which (a) coalesces only partially and leaves a smaller droplet behind and (b) one that cascaded six times. (c) Droplet footprint area as a function of time. The orange crosses and blue circles correspond to the data shown in Fig. 3.5(a-i) and (j-r), respectively.

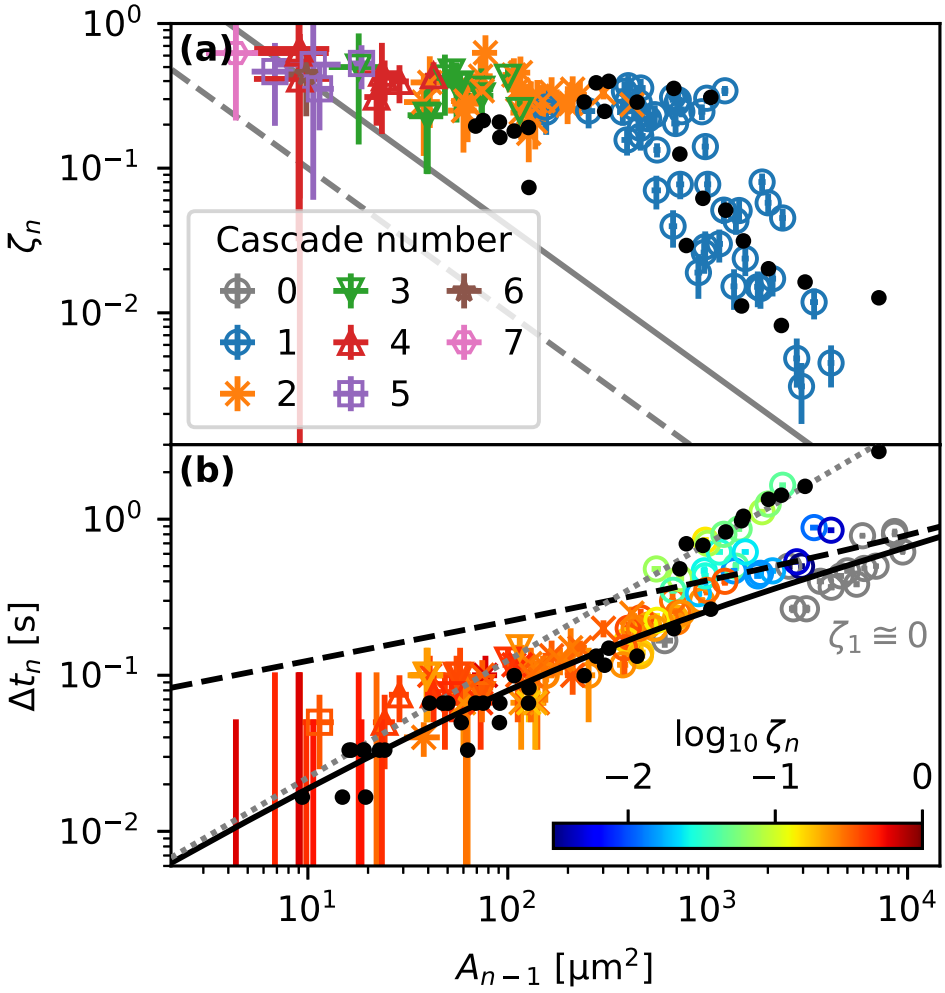

Figure 3.7: (a) Area reduction ratio ζ_n and (b,c) contact time Δt_n of droplets with footprint area A_{n-1} undergoing their n-th cascade. The solid and dashed lines in (a) represent the resolution limits of experimentally observable ζ_n values for two used microscope magnifications. The color of the symbols in (b) represents the ζ_n value as indicated by the colorbar. Gray circles in (b) correspond to fully coalescing, non-cascading droplets. The dashed and solid black lines and the dotted grey line represent Eqs. (3.11), (3.14) and (3.15), respectively. Black dots represent measurements on substrates treated with 2-propanol.

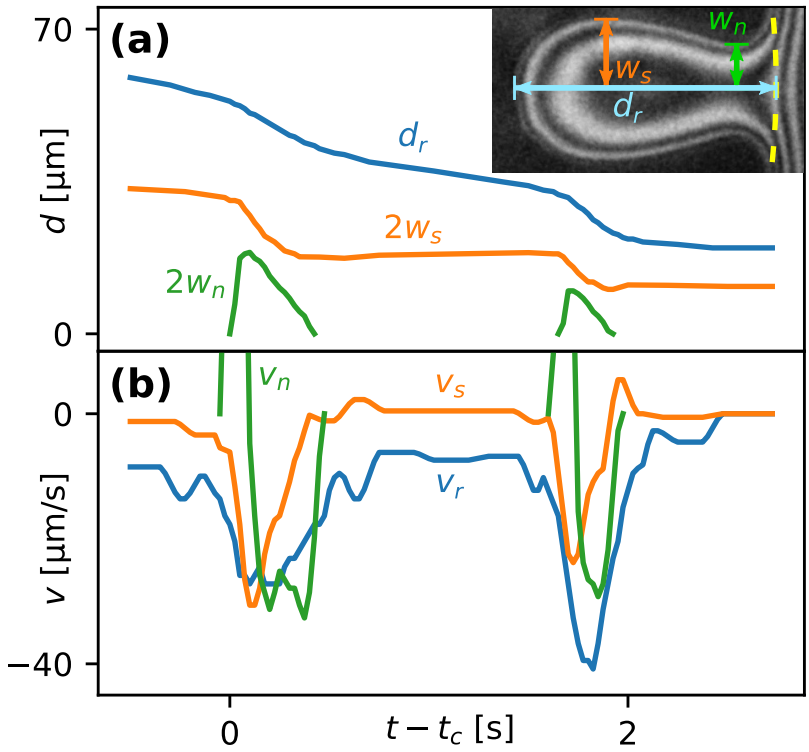

Figure 3.8: (a) Time dependence of the rear position d_r, maximal width w_s and neck width w_n of a droplet undergoing two coalescence cascades. Inset: definitions of d_r, w_s and w_n. The contact spot edge is marked with a dashed yellow line. (b) Contact line speed at the rear (v_r), side (v_s) and neck (v_n) of the droplet.

as described in Ref. [85], to investigate the influence of uncrosslinked chains on the movement of droplets.

Figure 3.8(a) shows the position of the rear d_r, the maximal half-width w_s and the neck half-width w_n of a droplet undergoing two partial coalescence cascades. The definitions of these parameters are illustrated in the inset. Figure 3.8(b) shows the contact line speed at the back ($v_r \equiv \dot{d}_r$), side ($v_s \equiv \dot{w}_s$) and neck ($v_n \equiv \dot{w}_n$) of the droplet, where a dot above a parameter indicates a time derivative. The two not visible positive maxima of v_n are at 110 and 60 μm/s, respectively. We note that v_s reacts immediately to the formation of a liquid bridge ($w_n > 0$) but v_r is delayed. This feature, as well as the positive values of v_s after breakup, is due to the droplet relaxing to a

rounder shape after becoming elongated during the coalescence. To maintain a constant aspect ratio w_s/d_r the back would need to move twice as fast as the side.

3.5 Comparison with Numerical Simulations

In order to elucidate the qualitative difference between cascading and non-cascading droplets we turn to numerical simulations for gaining further insight. We used the same fully-coupled, three-dimensional numerical model that is described in detail in Ref. [84]. We combine the stationary Cauchy momentum equation for soft, linear elastic materials with the Reynolds equation for thin film flow and apply a disjoining pressure formalism to implement the partial wettability. We solved the equations using finite element software COMSOL Multiphysics®. In our numerical simulations we disregard the dewetting process visible in Fig. 3.1(b) but rather use an initial condition analogous to the first frame of Fig. 3.2(a). A single droplet of given volume is released at a certain distance from the center of the contact spot.

The circles in Fig. 3.4 represent numerical simulations, with their color indicating the value of the parameter

$$|\widetilde{S}| \equiv \frac{\pi Y h_d^2}{6 a_d}\,, \tag{3.16}$$

obtained by extracting the footprint radius a_d and height h_d of a droplet. Equation (3.16) is derived from Eq. (3.1) for half-ellipsoidal droplets, but based on values of h_d and a_d taken from the simulations. The dashed lines are linear relations $\psi \sim a_d$, which match the numerical results reasonably well, again consistent with Eq. (3.8).

Figure 3.9 compares experimental droplet morphologies with numerical simulations. The dotted white lines in Fig. 3.9(a-e) mark the edge of the contact spot. The solid lines in Fig. 3.9(f-j) are lines of equal liquid film thickness, similar to the interference fringes in (a-e). The overall shape of the simulated droplets agrees very well with the experimentally observed ones.

Figure 3.10 shows snapshots from three different simulations of escaping droplets, where we have varied the droplet footprint radius

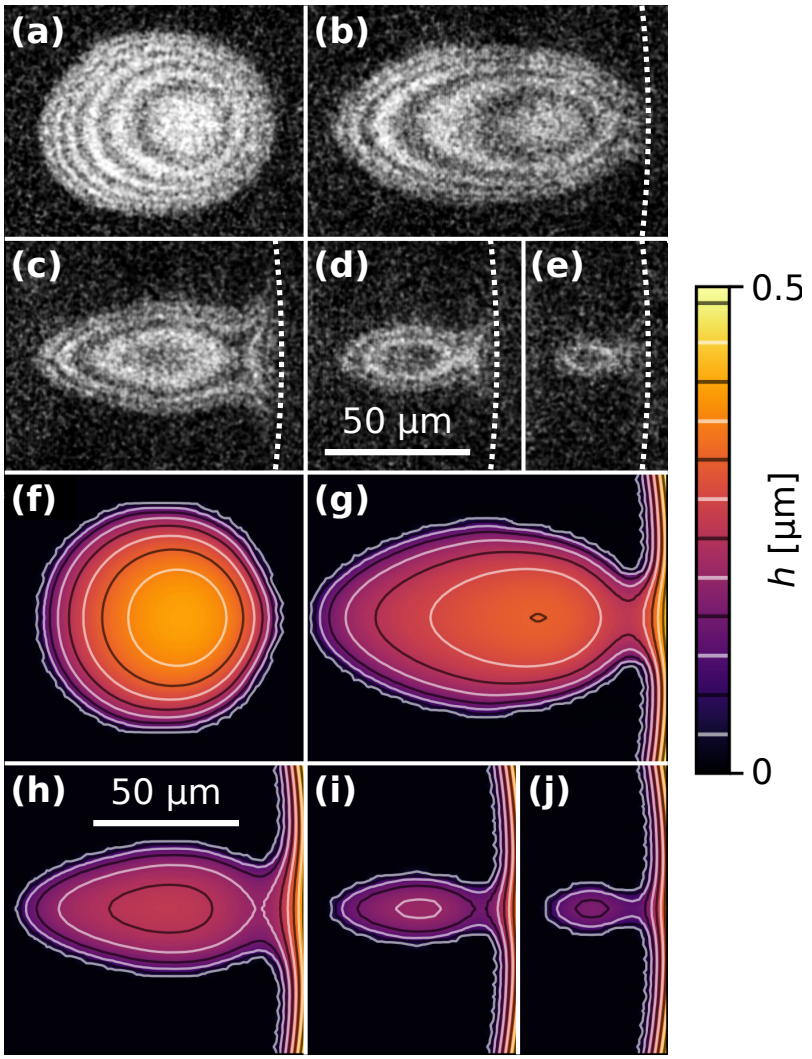

Figure 3.9: Snapshots from an experiment (a-e) and a numerical simulation (f-j) showing similar droplet morphologies before and during complete coalescence with the outer bulk liquid, i.e. without cascading. The contours in (f-j) are lines of equal film thickness, similar to the interference fringes in (a-e). The (identical) scale bars in (d) and (h) apply to all images.

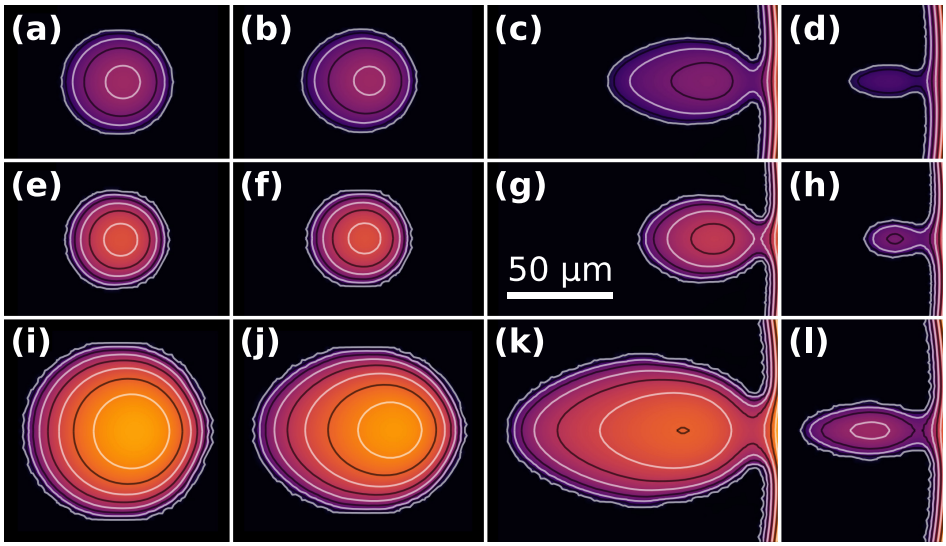

Figure 3.10: Snapshots from three numerical simulations. Columns 1-4 show droplets when $d/r_{cs} = 0.45$, 0.3, at the start of coalescence and during coalescence, respectively. Row (a-d) shows a droplet with initial length $L_d = 52\,\mu\text{m}$ and $|\widetilde{S}| = 4.2\,\text{mN/m}$. The value of $|\widetilde{S}|$ was twice as high in row (e-h) as in row (a-d), i.e. $|\widetilde{S}| = 9.5$ mN/m and $2a_d = 49\,\mu\text{m}$. The droplet was twice as wide in row (i-l) as in row (e-h), i.e. $2a_d = 90\,\mu\text{m}$ and $|\widetilde{S}| = 8.9\,\text{mN/m}$.

a_d as well as the parameter $|\widetilde{S}|$. In Fig. 3.10(i-l) a_d is twice as large as in (a-h), whereas $|\widetilde{S}|$ is twice as high in Fig. 3.10(e-l) compared to (a-d). In other words, rows (a-d) and (i-l) share the same L_{ec}/a_d ratio, whereas row (e-h) has twice as large a ratio. We note that the similar morphology evolution of Figs. 3.10(a-d) and (i-l) may be related to these cases having the same ratio of the elastocapillary length L_{ec} to the footprint radius a_d. Similarly, the higher ratio in Fig. 3.10(e-h) may be responsible for the less elongated shape throughout the droplet escape history.

3.6 Discussion

So-called partial coalescence and coalescence cascades have been observed for droplets contacting other droplets or flat liquid-liquid or

liquid-air interfaces.[87–99] Usually partial coalescence of pure liquids requires a high Weber number i.e. sufficient inertia and the propagation of capillary waves, i.e. an Ohnesorge number below a critical value. In our case $\mathrm{We} \equiv \rho v_d^2 a_d/|S| \approx 10^{-8}$ and $\mathrm{Oh} \equiv \mu/\sqrt{\rho|S|a_d} \approx 10$, therefore capillary waves are not present as the system is strongly dominated by viscous forces. Glass *et al.* studied the effect of water-soluble polymers on coalescence cascades of organic liquid drops at an organic liquid-water interface.[100] Sartor and Abbott and Beard *et al.* considered the effect of dissimilar electrical droplet charges on the coalescence of colliding droplets and found that charge differences promote complete coalescence.[101–103] Ristenpart *et al.* studied the droplet rebound from a liquid-liquid interface subject to an applied perpendicular electric field.[104] Beard *et al.* showed that a reduction in air pressure promoted contact, thereby reducing the likelihood of bouncing and increasing that of permanent coalescence.[105] Feng *et al.* investigated the effect of non-Newtonian rheology on the coalescence dynamics.[106,107] When either the drop or the surrounding phase is a polymer solution, viscoelasticity tends to delay the break-up of secondary drops and can suppress partial coalescence altogether, as large tensile polymer stresses resist the stretching and thinning of the fluid neck. Kuznicki *et al.* considered the effect of electrolyte concentration on coalescence cascades of oil droplets.[108] De Malmazet *et al.* showed that the presence of micro-particles reduces drop lifetimes and promotes coalescence.[109] Blanchette *et al.* studied the influence of solutocapillary Marangoni stresses on drop coalescence.[110] Surfactants can enhance or weaken partial coalescence effects, depending on the concentrations and the induced surface elasticity.[111–116]

For our system, inertia is negligible and there are no propagating capillary or elastic waves induced by the droplet motion. Although the dependence of contact time on droplet radius $\Delta t \sim R^{3/2}$ as observed by e.g. Thoroddsen and Takehara[88] agrees with the scaling $\Delta t \sim a_d^{3/2}$ in Eq. (3.15) this agreement is coincidental as the prefactors depend on unrelated material properties. Our material system is not susceptible to surfactant adsorption. Moreover, we have measured electric surface charge distribution induced by solid-on-solid contact and separation, but it was below the detection limit (10^{12} ions/m^2).[117,118] Since the droplets move smoothly and continuously without stick-slip behavior and since they maintain a round and mirror-symmetric morphology, it

is highly unlikely that surface irregularities and defects are responsible for the slow motion and the cascading behavior. Non-homogeneities tend to cause irregular droplet footprints and non-monotonic velocity profiles.

We speculate that the coalescence cascades are merely a consequence of the slow contact line speed. The latter implies that the aspect ratio of the liquid bridge becomes slender such that it is susceptible to break-up. This is analogous to the partial coalescence mechanism for liquid droplets suggested by Blanchette and Bigioni: if capillary waves can sufficiently delay the vertical (in our case: radial) collapse, pinch off will occur and a smaller drop will be left above the interface (in our case: near the edge of the contact spot).[92,94] Instead of capillary oscillations delaying the forward motion of the rear end of the free droplets studied by Blanchette and Bigioni, the delay in our case is likely of a different nature. This may hint at the presence of a dissipation mechanism that depends non-linearly on the droplet velocity. Such a dissipation mechanism could explain the observed variation of the droplet speeds by two orders of magnitude in Fig. 3.3.

In our numerical simulations we consider a homogeneous surface and bulk composition so far. The simulated droplets move according to hydrodynamical expectations and exhibit complete coalescence without cascading behavior. We have attempted to reproduce the slow yet smooth droplet motion seen in the experiments in Fig. 3.3 by modulating geometric and material properties of our system. Specifically, we considered the influence of surface roughness as well as spatial modulations of the spreading parameter $|S|$ and Young's modulus Y. As for the latter two, we generally found that for experimentally conceivable parameter variations, the reduction in contact line speed was far less than two orders of magnitude. In the following subsection we report on the effect of surface roughness.

3.6.1 Influence of surface roughness

In order to study the effects of surface roughness we considered a two dimensional axisymmetric system for computational efficiency. We introduced a sinusoidal surface profile of the rigid substrate with wavelength λ and amplitude A. In order to nucleate a dry spot and obtain a receding contact line, we introduce a topological defect centered

around $r = 0$ shown by the gray shaded area in Fig. 3.11(a). Dotted and dash-dotted lines indicate the sinusoidal surface profiles for two different sets of values of λ and A. In order to speed up calculations, the pattern starts at a certain radial position r_0 and extends only over a few wavelengths. The solid and dashed lines correspond to the z-position of the elastomer-liquid interface. The inset shows the entire contact spot from its center to its edge.

Figure 3.11(b) shows the time evolution of the non-dimensional elastomer-liquid interface profile. The contact line recedes to the right. For clarity, we non-dimensionalized the r and z coordinates using the scales of λ and A in order to collapse the two surface profiles. The two families of curves represent constant time increments of either 1 or 10 milliseconds, corresponding to two different sets of λ and A. In the case of the smaller amplitude ($A = 20$ nm, dashed orange lines) the contact line moves continuously, though at a non-constant speed v_{cl}. v_{cl} is considerably faster when moving up a slope compared to moving down. In the case of the larger amplitude ($A = 50$ nm, solid blue lines), the contact line gets pinned on the descending slope, despite the A/λ aspect ratio being the same as in the first case. The contact line advances by nucleating a secondary dry spot at the adjacent apex of the surface roughness profile. At the same time liquid becomes entrapped in the "valleys", as indicated by the dashed arrow.

In Fig. 3.12 is plotted the contact line speed $v_{\text{avg}} \equiv \langle v_{cl} \rangle$ averaged over two wavelengths of the roughness profile. Filled symbols signify liquid entrapment. The average contact line speed strongly decreases with increasing amplitude A, more rapidly for smaller values of the wavelength λ, i.e. higher aspect ratios A/λ. Due to computational limitations concerning the minimum mesh size, we could not explore sub-micron values of λ. However, it is clear from Fig. 3.12 that especially for small λ a significant reduction in the average velocity is observed, at least by one order of magnitude. Extrapolating towards sub-micron wavelengths, these results indicate that even with a roughness amplitude so small that it would not be noticeable using optical interferometry, the contact line speed could be reduced by a similar order of magnitude as observed in the experiments in Fig. 3.3. Due to the limited spatial resolution of our optical setup, the corresponding spatial modulation of the contact line speed v_{cl} could not be resolved and would appear as smooth. Based on these results we hypothesize

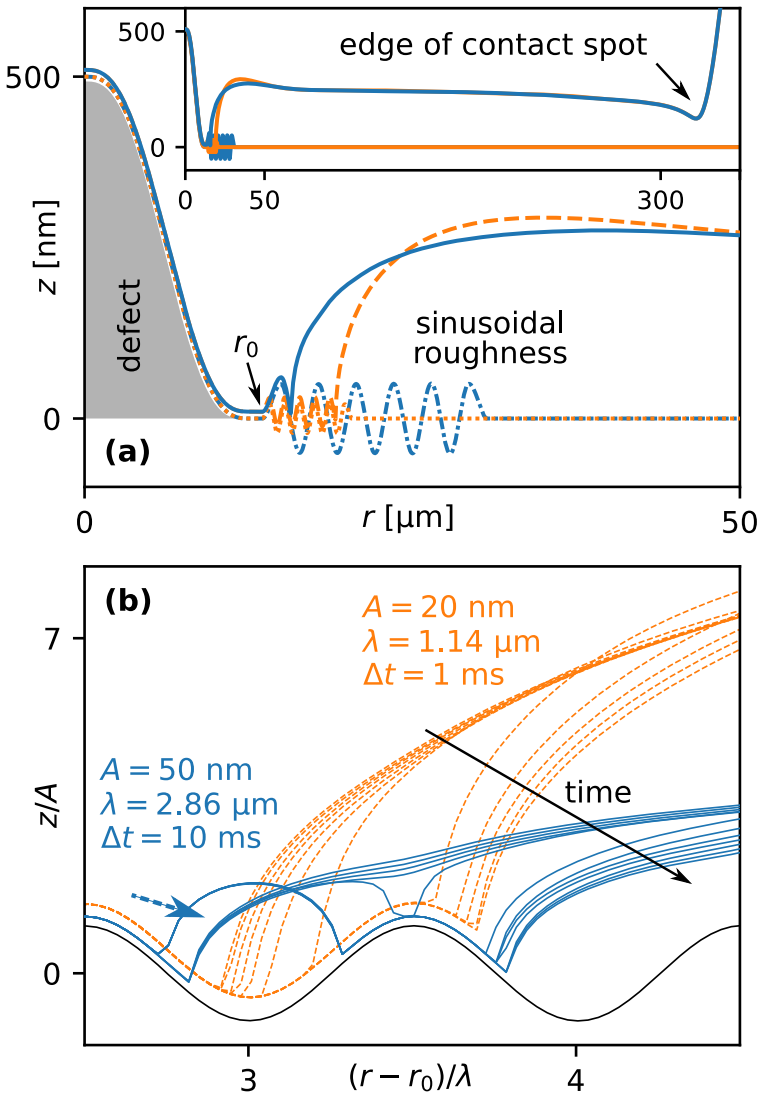

Figure 3.11: Simulated liquid film thickness profiles for non-flat substrate topologies. (a) The dash-dotted blue line shows the substrate topology, with a sinusoidal pattern of amplitude $A = 50$ nm and wavelength $\lambda = 2.86\,\mu$m. The solid blue line represents the z-position of the elastomer-liquid interface. The dashed and dotted orange lines represent a similar simulation with $A = 20$ nm and the same A/λ ratio. (b) Time evolution of the non-dimensional elastomer-liquid interface profile. The two families of curves represent constant time increments of either 1 or 10 ms.

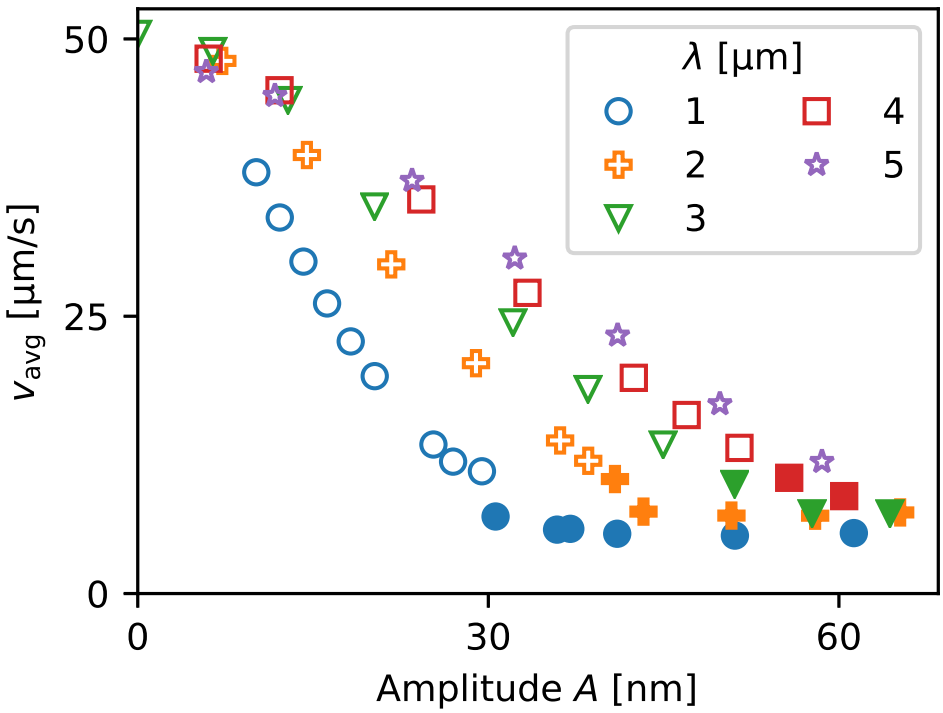

Figure 3.12: Average speed of the receding contact line moving across the pattern in Fig. 3.11(a), as a function of the pattern wavelength λ and amplitude A. Larger amplitudes and smaller wavelengths can slow down the movement by an order of magnitude. Filled points signify liquid entrapment.

that the non-hydrodynamic motion of the droplets could be caused by surface roughness.

3.6.2 Influence of uncrosslinked chains

Despite the 22.5% mass loss after 2-propanol treatment, the observed droplet dynamics remained the same. The data points in Fig. 3.7 overlap with the ones obtained with not-treated samples. We conclude that uncrosslinked chains do not influence the droplet motion in our case. In contrast, in Ref. [85] the uncrosslinked chains had a drastic effect on sessile droplet motion. We believe that this qualitative difference might be related to the much higher interfacial tension of the liquids (glycerol-water mixtures) used by these authors as well as

the presence of a deformable liquid-air interface, which is absent in our case.

3.7 Conclusion

We have studied the escape dynamics of liquid droplets from the contact zone of an elastic hemisphere pressed into a soft solid layer. The driving force of the motion is the radial pressure gradient. Upon reaching the edge of the contact spot, droplets merge with the outer bulk liquid either in a continuous or discontinuous fashion. In the first case a single 'complete' coalescence event is observed, whereas in the latter case a cascade of partial coalescence events occurs. Numerical simulations could reproduce the shape and escape dynamics of the non-cascading droplets qualitatively well. The coalescence time of these droplets are well described by a simple analytical model.

Droplets that undergo a coalescence cascade tend to move much slower than droplets that merge in a single coalescence event. Moreover, the speed of motion of the cascading droplets is not proportional to the local pressure gradient. Using numerical simulations, we have investigated surface roughness and spatial modulations of Young's modulus and the spreading parameter as potential mechanisms that could slow the droplets down. As for the latter two, we generally found that for experimentally conceivable parameter variations, the reduction in contact line speed was far less than two orders of magnitude. In contrast, surface roughness induced a speed reduction comparable with the experimental observations and is thus a viable candidate for the responsible mechanism. Solvent extraction of uncrosslinked chains in the elastomer did not have an impact on the observed droplet dynamics.

Acknowledgement

I would like to thank Jesse Kwaks for his help with the experiments and analysing experimental results.

Chapter 4

Elastohydrodynamic dewetting of thin liquid films – elucidating underwater adhesion of topographically patterned surfaces

4.1 Introduction

Surfaces with topological patterns can exhibit remarkable wetting and adhesion properties. Many examples are found in nature: geckos can locomote on a ceiling.[37, 119] Lotus leaves do not get wet in the rain.[47] Springtails can breathe underwater.[57, 120] There is ongoing interest in replicating these properties and designing bio-inspired micro- and nano-patterned surfaces.

In the context of adhesion, micropatterned surfaces commonly adhere better to smooth and even rough substrates, as stresses at the contact interface are distributed more homogeneously and cracks are blunted upon detachment of single fibrils.[41, 121, 122] Furthermore, micropatterned surfaces show great potential for improving adhesion under wet conditions and underwater.[26–29, 123–134]

At first glance, this observation is counterintuitive from a hydrodynamic perspective. The presence of liquids such as water between two surfaces is generally detrimental to achieving a high adhesion strength,

as liquids are essentially incompressible and thus prevent close contact. Moreover they can reduce the effective Hamaker constant by up to a factor of 10.[63] Consequently, the complete removal of liquid between the contacting materials is conducive to a high underwater adhesion performance. Therefore, a detailed understanding of the dewetting dynamics of micropatterned surfaces is desirable.

Arrays of pillars are often used as a model system to study the wetting of rough surfaces.[30–36] Extrand *et al.* as well as Ishino *et al.* described[44, 45] how liquid droplets in a Wenzel state can spread through a pillar array through wicking, in the form of a precursor film slightly thinner than the pillar height. Courbin *et al.* demonstrated[46] how this process can be anisotropic, with the precursor film spreading in a circular, octagonal or square shape. Chu *et al.* developed[43] a system with slanted pillars, which caused the deposited droplet to spread unidirectionally. Further research[135–137] focused on the details of anisotropy in contact line movement on patterned surfaces, showing how it can be considered as a series of pinning or depinning events.

In this manuscript we studied the dewetting dynamics of a thin, partially wetting liquid film confined between a rigid, periodic micropillar array and a soft, elastic sphere. We systematically studied the impact of the array period on the expansion rate and the morphology of the dewetted areas. Moreover, we performed fully-coupled three-dimensional numerical simulations, which reproduce the observed phenomena qualitatively well.

4.2 Experimental section

4.2.1 Experimental procedure

Figure 4.1 illustrates the geometry and the time evolution of a typical experiment. A soft elastic hemisphere (radius of curvature 2 ± 0.5 mm) is pushed onto a rigid glass substrate with an initially thick, intervening liquid layer. The elastomers used were silicone-based, heat-curable, two-component polymer resins (Smooth-On Encapso K, Young's modulus $Y = 1.365\,\mathrm{MPa}$ and Sylgard 527, $Y = 11.28\,\mathrm{kPa}$). The liquid is a perfluoropolyether (Solvay, Fomblin Y LVAC 14/6, average molecular weight 2500, viscosity $\mu = 0.2646\,\mathrm{Pa\,s}$, surface tension $\gamma_L = 22\,\mathrm{mN/m}$).

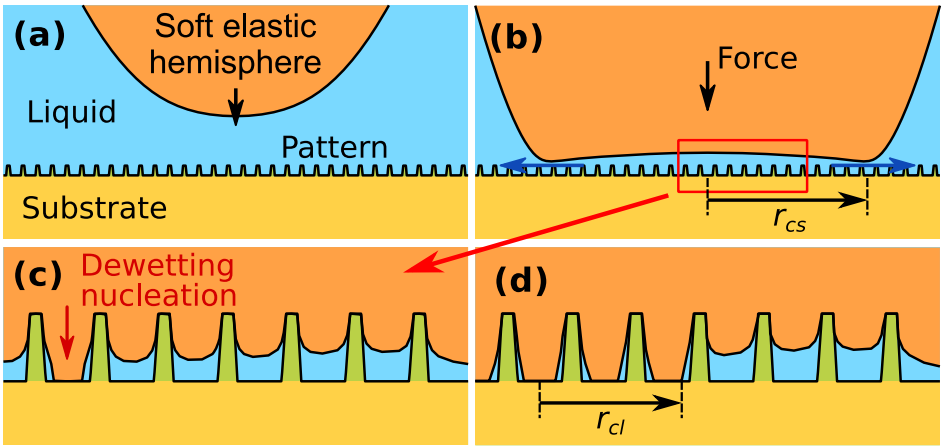

Figure 4.1: (a) Side-view sketch of the experimental geometry. A soft elastic hemisphere is pushed onto a glass substrate with an intervening liquid layer. The substrate contains a microscopic surface pattern in the form of a square array of cylindrical pillars. (b) A thin liquid film is formed in the contact spot. The radius of the contact spot r_{cs} is highlighted. (c) Magnified view of the nucleation of a dewetted area. (d) The dewetted area grows over time, pushing liquid out of the contact spot. The extension of the dewetted area radius r_{cl} is highlighted, defined relative to the nucleation center.

Its contact angles on the elastomer surface and the substrate base plane are both $\theta = 30° \pm 10°$. The substrate contains a microscopic surface pattern in the form of a square array of cylindrical pillars.

Upon approaching the substrate, the bottom of the hemisphere elastically deforms. This leads to the formation of a well-defined contact spot [Fig. 4.1(b)] that defines the lateral extension r_{cs} of the sub-micron thick liquid film [dashed lines in Figs. 4.1(b) and 4.2(b)]. The compressive force acting exerted on the hemisphere is in the range of 0.1–30 mN and is kept constant during an experiment. The specific value is chosen to obtain a contact radius of 250 ± 50 μm depending on the Young's modulus of the elastomer used. We have monitored the thickness of the ultra-thin liquid film using optical interferometry (450 nm wavelength). The experimental setup is described in detail in Ref. [84].

4.2.2 Micropillar array fabrication

Microscopic pillars were made from a negative tone photoresist (IP-Dip, Nanoscribe) using a two-photon lithography system (Professional GT, Nanoscribe). The nominal pillar height h_p and diameter $2r_p$ were 1 μm and 7 μm, respectively. The pillars were arranged in a square array with center-to-center distance d_p varied between 10 and 50 μm. Fused silica slides with a coating of 3-methacryloxypropyl trichlorosilane (product number AB109004, abcr) were used as substrates. The structures were generated using the so-called "dip-in mode", where the objective was dipped directly into the resist. Exposure parameters were a power scaling of 0.86, a laser power of 25 mW and a scan speed of 10 mm/s. After exposure, the micropillars were developed using propylene glycol monomethyl ether acetate (product number 484431, Sigma Aldrich) for 20 minutes and post-cured to enhance the mechanical stability.[138] For post-curing, the micropillars were exposed to 365 nm ultraviolet light (OmniCure S1500A, 200 W, igb-tech) in a nitrogen atmosphere. The elastic modulus of the micropillars is approximately 1 GPa.[139]

4.3 Numerical models

4.3.1 Dewetting simulations

We developed a three-dimensional, fully coupled finite element method model of the elastic deformation of the hemisphere, the thinning and dewetting of the thin liquid film. The model combines the stationary Cauchy momentum equation for soft, linear, non-dissipative, isotropic and homogeneous elastic materials

$$\sum_{i=1}^{3} \frac{\partial \sigma_{ij}}{\partial x_i} = 0 \tag{4.1}$$

in the absence of body forces, with the Reynolds equation for thin film flow

$$\frac{\partial h}{\partial t} + \nabla_{||} \left[h \frac{\mathbf{v}_e + \mathbf{v}_s}{2} - \frac{h^3}{12\eta} \nabla_{||} p_f \right] = 0 \ . \tag{4.2}$$

Here, σ_{ij} is the stress tensor, h is the liquid film thickness, t is time, η is the dynamic viscosity of the liquid, p_f is the pressure in the liquid film, and $\mathbf{v}_e$ and $\mathbf{v}_s$ are the tangential velocities of the liquid-elastomer interface and the substrate surface, respectively, which are computed from the elastic displacements. The partial wettability of the liquid is implemented using a disjoining pressure formalism. All simulations have been performed for the material parameters $Y = 1.365\,\mathrm{MPa}$ and $\nu = 0.499$, which is close to the value of 0.5 corresponding to incompressible elastomers.[140, 141]

The geometry of the pillar array and the computational domain used in the model are sketched in Fig. 4.2. We assume that the pillar array has an even number of columns and rows and that the apex of the hemisphere is moving vertically downward along the surface normal of the substrate above the center of the array. In this fashion the system exhibits mirror symmetry planes parallel to the axes and the main diagonals of the square array. The existence of these symmetry planes allows us to restrict the computational domain to the 45° slice shown in Fig. 4.2(b). Outside of the contact spot, a Dirichlet boundary condition for the pressure $p = p_{\mathrm{amb}}$ is applied, where the constant ambient pressure p_{amb} is set to zero.

Details of the model can be found in Ref. [84]. Only Eq. (16) in Ref. [84] requires modification to account for the non-flat topography:

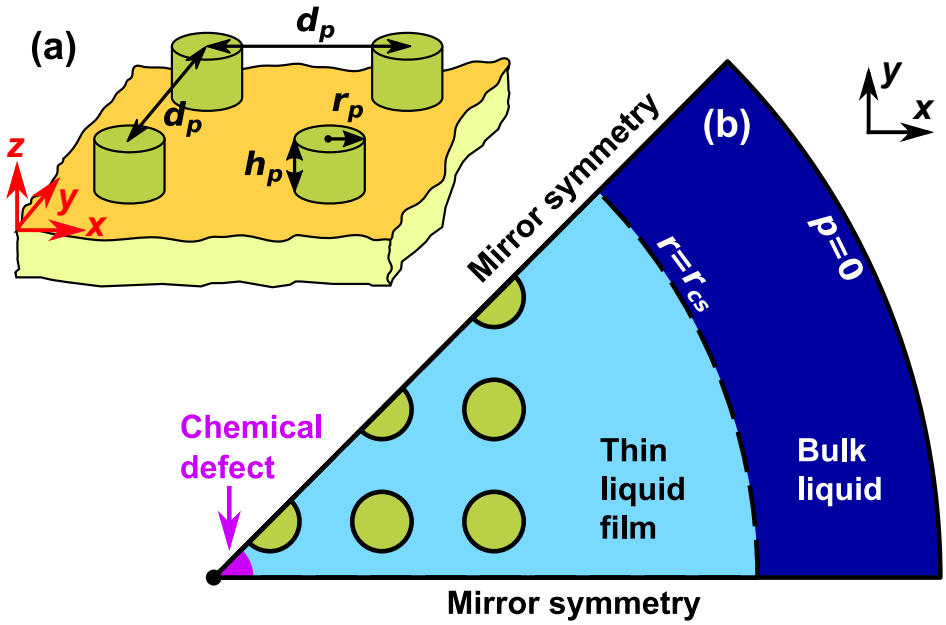

Figure 4.2: (a) 3D sketch of the pillar array. (b) Bottom-view sketch of the computational domain. The dashed line corresponds to the radius of the contact spot.

the function $z_d(\mathbf{r})$ is replaced by

$$z_{\text{topo}}(\mathbf{r}) \equiv \sum_i z_p(|\mathbf{r} - \mathbf{r}_i|) \ , \tag{4.3}$$

where the summation is over all micropillars in the array with corresponding center positions $\mathbf{r}_i$. The function

$$z_p(r) = h_p f_{hs}[2(r_p - r)/s_p] \tag{4.4}$$

describes the axisymmetric shape of a single pillar, where $s_p = 2.5\,\mu$m is the radial distance over which z_p changes smoothly from h_p to 0 and f_{hs} is the smoothed Heaviside function, defined by Eq. (14) in Ref. [84]. The nucleation of dewetting was induced by a topographic defect in Ref. [84]. In contrast, we now used a small chemical defect, i.e. a circular region with locally higher contact angle, in the center of the domain.

4.3.2 Contact mechanics simulations

In addition to the fully-coupled model described above, we also performed contact mechanics simulations of a single unit cell of the micropillar array. We solve the stationary Cauchy momentum equation (4.1) in the absence of any intervening liquid. This implies that the resulting elastomer configuration corresponds to the long-time limit of a simulation including liquid, if permanent trapping of liquid cannot occur. The latter condition is fulfilled in our model including liquid, because in the context of the disjoining pressure formalism, an ultrathin precursor layer is present, which provides a small but nonzero hydraulic conductivity towards the surrounding liquid bulk.

The conceptual setup, the computational domain and relevant boundary conditions (BCs) of the contact mechanics simulations are illustrated in Fig. 4.3(a-d). Typically, one unit cell of the micropillar array is much smaller than both the radius of curvature of the elastomer hemisphere and the radius of the contact spot. Therefore, for simplicity we have assumed that the elastomer is an elastic layer of large thickness $H \gg d_p$ and $H \gg h_p$, approximating the behavior of an elastic halfspace. This allows us to reduce the size of the computational domain [indicated by the red triangle in Fig. 4.3(c)] to one eight of a unit cell by exploiting symmetry boundary conditions. The elastic

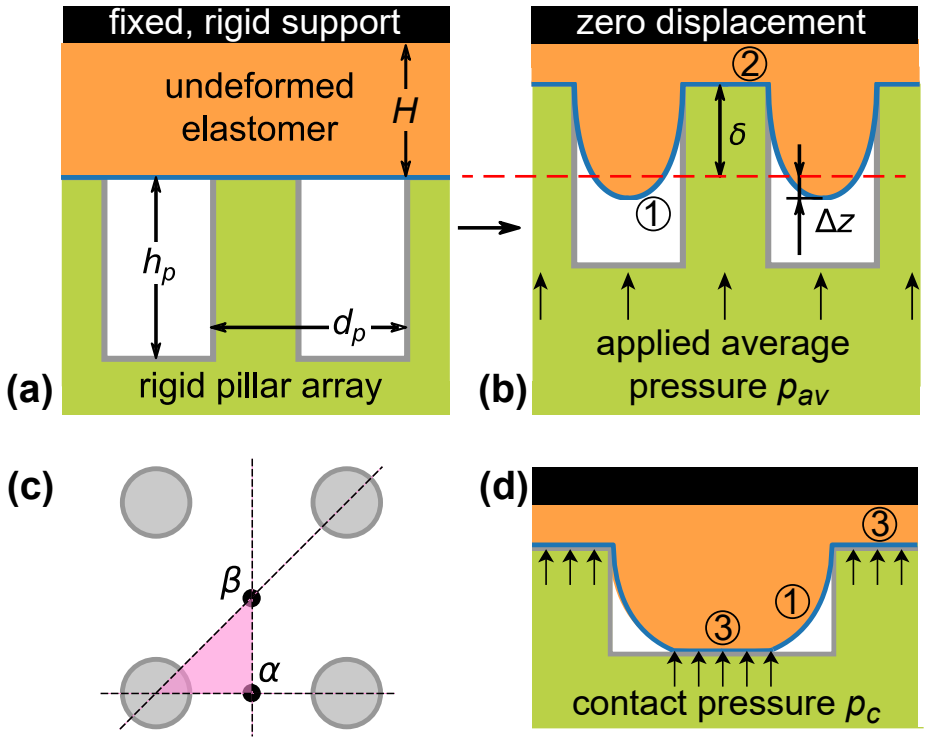

Figure 4.3: (a) At zero applied pressure the pillar array just touches the elastomer layer of thickness $H \gg d_p$ without deforming it. The elastomer is backed by a fixed, rigid support. (b) Definition of the protrusion depth $\delta + \Delta z$ of a deformed elastomer layer in contact with a rigid pillar array. The red dashed line indicates the position of the elastomer-pillar interface for zero applied pressure. (c) Top-view of the three-dimensional computational domain (red triangle) of the contact mechanics simulations. Its vertical boundaries (indicated by the dashed lines) are mirror-symmetry planes of the micropillar array. The points labeled α and β are the midpoints between pairs of neighboring pillars along the x-axis and the array diagonal, respectively. (d) Illustration of the contact pressure BC for the case where the elastomer protrusions contact the substrate base plane.

displacements vanish normal to the vertical mirror symmetry planes of the micropillar array indicated by the dashed lines in Fig. 4.3(c). The elastomer is assumed to be attached to a rigid support. Consequently, zero displacement BCs apply at large depths $z = H$.

The rigid pillar array is pushed upwards with an applied average pressure p_{av} and thereby indents and deforms the elastomer. Figure 4.3(b) provides a definition of the protrusion depth $\delta + \Delta z$ of the deformed elastomer layer. Here, δ is the (position-independent) indentation depth of the tops of the pillars and $\Delta z(x, y)$ the (position-dependent) protrusion amplitude relative to the surface level of the undeformed elastomer (as indicated by the red dashed line).

We have implemented two different models depending on whether the pillar height was larger or smaller than the protrusion depth $\delta+\Delta z$. In the first case, the applicable BCs sketched in Fig. 4.3(b) are zero shear stress $\sigma_{xz} = \sigma_{yz} = 0$ and constant vertical displacement $u_z = \delta$ at the tops of the pillars (indicated by ②) and zero shear and zero normal stress at the elastomer-air interface (indicated by ①). The average applied pressure p_{av}, which is linearly related to the indentation depth δ, is determined from the computed stress distribution σ_{zz} at the tops of the pillars. In the second case, where the protrusion depth is sufficient to make contact with the base plane of the pillar array, we implemented an empirical contact pressure p_c boundary condition [indicated by ③ in Fig. 4.3(d)] at the solid-elastomer interfaces. The contact pressure p_c dependends on the overlap distance δ_w that the elastomer and the substrate would have in the absence of a contact condition

$$p_c(\delta_w) = \begin{cases} 0 & \text{if } \delta_w \leq 0 \\ C_f \delta_w^{3/2} & \text{if } \delta_w > 0\,. \end{cases} \tag{4.5}$$

Here, $C_f = 10^{17}\text{Pa}\,\text{m}^{-3/2}$ is an interaction stiffness parameter, chosen to be as high as possible without foregoing the model's convergence. All elastomer-solid interfaces are assumed to be frictionless. At the elastomer-air interfaces, again zero shear and zero normal stress BCs apply.

4.4 Results and discussion

4.4.1 Experimental results

The elastic deformation of the hemisphere induces a non-uniform pressure distribution, with a local maximum in the center and ambient pressure just outside the contact spot.[73, 86] The ensuing pressure gradient pushes the intervening liquid out of the contact spot. At some point the deformed hemisphere contacts the top of the pillars. Since the height $h_p = 1\ \mu$m of the pillar array is much smaller than the array period $d_p = 15 - 50\ \mu$m, the deformed elastomer squeezes into the interstitial region between neighboring pillars and eventually contacts the glass substrate [Fig. 4.1(c)]. Since the liquid is partially wetting, the liquid film becomes unstable and dewets below a minimum film thickness determined by the disjoining pressure.[24, 72, 84, 142] The dewetted area grows over time, pushing further liquid out of the contact spot [Fig. 4.1(d)].

Depending on the pillar array period, dewetted areas with very different morphologies were observed during dewetting. For large pillar spacing, the dewetting dynamics is similar to that of a flat surface.[24, 72, 84] Figure 4.4(a) shows the anisotropic growth of a dewetted area for pillar spacing $d_p = 21\,\mu$m and a very soft polymer $Y = 11.28\,$kPa. The non-circular shape of the dewetted area is caused by an anisotropy of the time-averaged contact line speed. Its motion is essentially unhindered along the axes, but slowed down along the main diagonal of the square array. In the experiment shown in Fig. 4.4(b), a more rigid polymer ($Y = 1.365\,$MPa) and a denser array ($d_p = 14\,\mu$m) were used, which gave rise to the occurrence of many irregular-shaped dry spots.

The expansion of the dewetted area in Fig. 4.4(a) proceeds in a concerted and time-correlated fashion all along its perimeter, otherwise the square shape would randomize and be lost. In contrast, the expansion of the dewetted area in Fig. 4.4(b) occurs in a spatially uncorrelated fashion, leading to the irregular shape. The red arrow indicates the localized spreading of the dewetted area into a neighboring unit cell of the array.

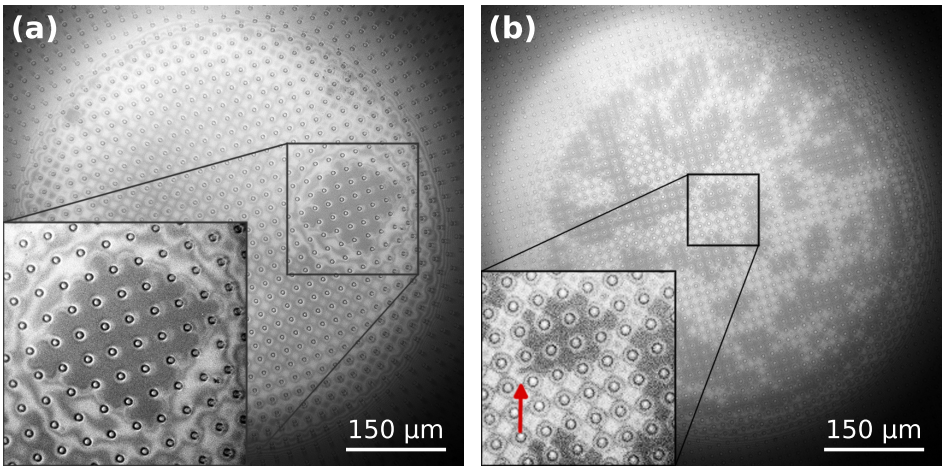

Figure 4.4: (a) Square-shaped dewetted area observed 14 s after dewetting nucleation in a system with pillar spacing $d_p = 21\,\mu$m and elastic modulus $Y = 11.28\,$kPa. (b) Using a denser array ($d_p = 14\,\mu$m) and a more rigid polymer ($Y = 1.365\,$MPa) results in the formation of a multitude of irregular-shaped dewetted areas that grow relatively slowly. The image was acquired 12 s after dewetting nucleation.

4.4.2 Numerical results

Figure 4.5 shows snapshots during the expansion of dewetted areas nucleated in arrays with different pillar spacings. The five columns represent the moments when the advancing contact line reaches distances r_{cl}/h_p of 20, 40, 60, 80 and 100 measured from the center of the array along the x-axis. The scale bar applies to all images. For $d_p/h_p \geq 25$ the dewetted area is diamond-shaped. For $d_p/h_p \leq 20$ it appears more round and $d_p/h_p = 22$ is an intermediate case, where the dewetted area is initially square but gets rounder as it grows.

Figure 4.6 shows a comparison between the dewetting mode in Fig. 4.4 and analogous numerical results. Figure 4.6(b) shows anisotropic growth of a dewetted area, similar to one in Fig. 4.4(a). The contact line moves faster along the axes of the square array, and slower along its main diagonal, resulting in a square shape. Figure 4.6(c,d) shows in magnification how a dewetted area expands from one unit cell of the array to a neighboring one. The colorbar in Fig. 4.5 also applies to Fig. 4.6(b,d).

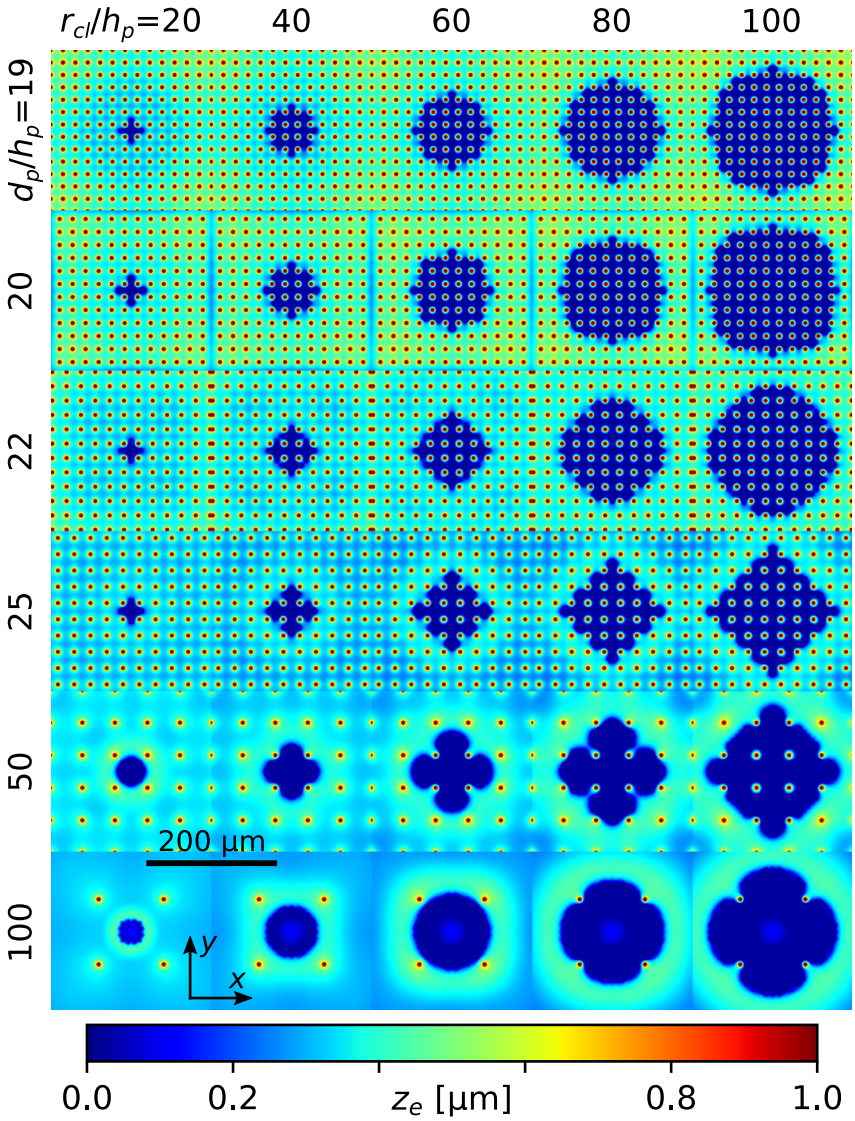

Figure 4.5: Numerical simulations of the expansion of the dewetted areas for different pillar spacing d_p. The five columns correspond to the moments when r_{cl}/h_p is equal 20, 40, 60, 80 and 100. The shape of the dry spot changes qualitatively for d_p/h_p between 22 and 25. The colors represent the liquid film thickness as indicated by the colorbar underneath the figure. The scale bar applies to all images.

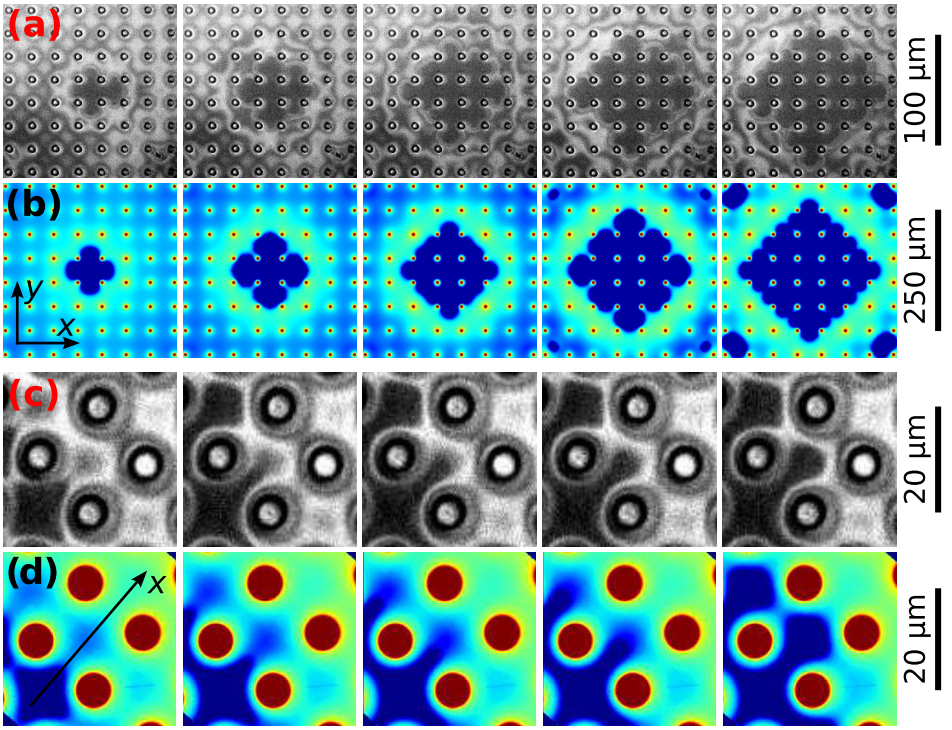

Figure 4.6: (a) Time evolution of the dry spot in Fig. 4.4(a). The panels correspond to 2.8, 5.3, 7.9, 9.8 and 11.8 s after dewetting nucleation. (b) A numerical simulation for $d_p = 50\,\mu$m and $Y = 1.365$ MPa yields similar results, a square-looking dry spot. (c) Magnification of Fig. 4.4(b) illustrating the dry spot growth mechanism. The contact line slowly advances between pillars to a neighboring unit cell of the array. The panels correspond to 11.8, 11.9, 12, 12.1 and 12.2 s after dewetting nucleation. (d) A numerical simulation for $d_p = 15\,\mu$m and $Y = 1.365$ MPa predicts a similar behavior. The colorbar in Fig. 4.5 also applies to (b,d).

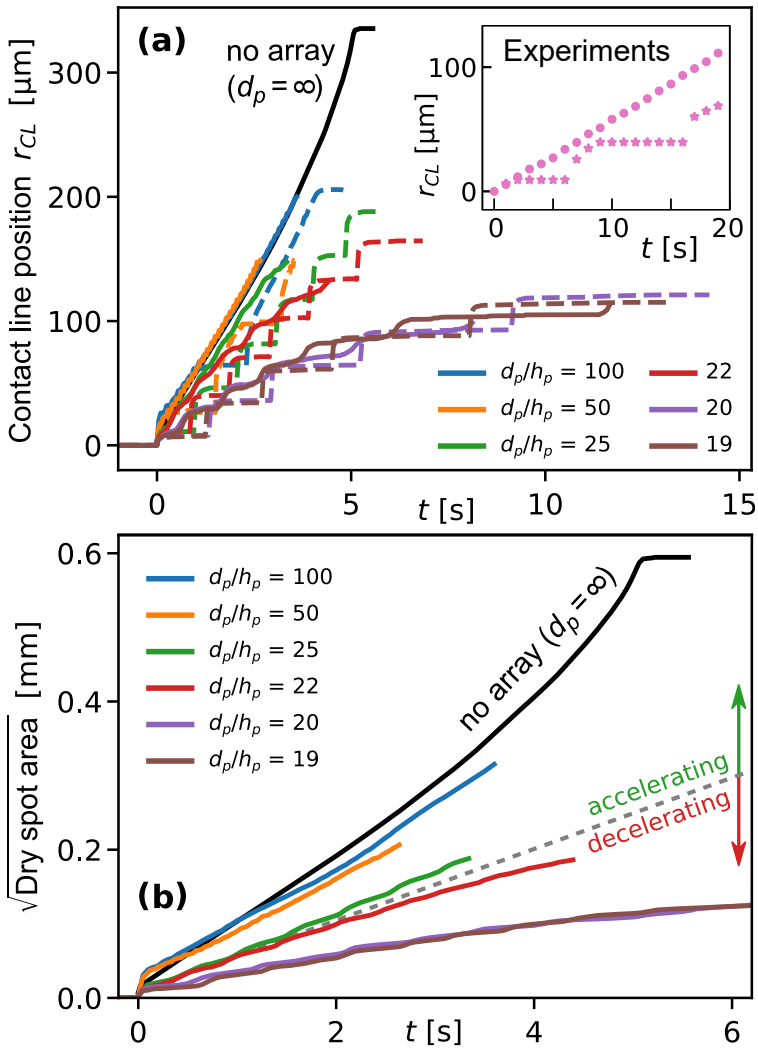

Figure 4.7: (a) Position of the contact line measured along the 'fast' direction (x-axis, solid lines) and the 'slow' direction (main diagonal $y = x$, dashed lines) in simulations with varying pillar spacing. Inset: equivalent experimental data corresponding to Fig. 4.4(a). (b) Square root of the dry-spot area as a function of time extracted from numerical simulations with varying pillar spacing. The curves are accelerating for $d_p \geq 25\,\mu$m (above dashed gray line) but decelerating for $d_p \leq 22\,\mu$m (below the dashed gray line). An analogous simulation with a flat substrate ($d_p = \infty$) is shown for comparison.

Figure 4.7(a) shows the position of the advancing contact line as a function of time measured along the x-axis (solid curves, circles) and along the main diagonal of the array ($y = x$, dashed lines, stars). The solid black line corresponds to a flat substrate without pillar array ($d_p = \infty$). Along the main diagonal [solid lines in Fig. 4.7(a)], the contact line moves until it reaches a pillar, where it gets pinned temporarily. It propagates around the pillar and eventually reaches the other side of the pillar, where it detaches and continues its motion. Along the x-axis [dashed lines in Fig. 4.7(a)], the contact line moves faster and with relatively uniform speed for $d_p \geq 25\,\mu$m. For $d_p \leq 22\,\mu$m the speed shows strong modulations due to the influence of nearby pillars.

The inset in Fig. 4.7(a) presents equivalent experimental data corresponding to Fig. 4.4(a). The qualitative behavior is completely analogous to the simulations, however, the timescales do not match. This discrepancy is mainly due to the large number of input parameters of the numerical model that are not accurately known, such as the disjoining pressure parameters and the interfacial energies.[84] Moreover, the nucleation point of dewetting was located off center in Fig. 4.4(a), which implies that the contact line could only be traced for a fraction of r_{cs}. In contrast, in the simulations the nucleation center was located in the center of the contact spot, such that the contact lines could be traced along the entire contact spot radius r_{cs}.

Figure 4.7(b) shows time dependence of the square root of the dry area $\sqrt{A_{\mathrm{dry}}}$ at the glass-elastomer interface, not including the dry pillar-elastomer interface. The origin of the abscissa $t = 0$ corresponds to the time at which the dewetting started. For $d_p \geq 25\,\mu$m (i.e. for curves above dashed gray line), $\sqrt{A_{\mathrm{dry}}}$ is accelerating in time, but for $d_p \leq 22\,\mu$m (curves below the dashed gray line) it is decelerating. The black line shows the result from an analogous simulation with a flat substrate (i.e. without micropillars, $d_p = \infty$). The initial jump at $t < 0.1\,$s is due to the chemical defect.

Figure 4.8(a,b) shows profiles of the liquid-elastomer interface and the pressure along the x-axis (i.e. inbetween two rows of pillars), right before dewetting commenced. For $d_p = 50$ and $100\,\mu$m, the liquid film thickness decreases towards the edge of the contact spot, similar to the case of a flat substrate. For $d_p \leq 25\,\mu$m, the liquid film thickness increases towards the edge of the array. The liquid film outside of

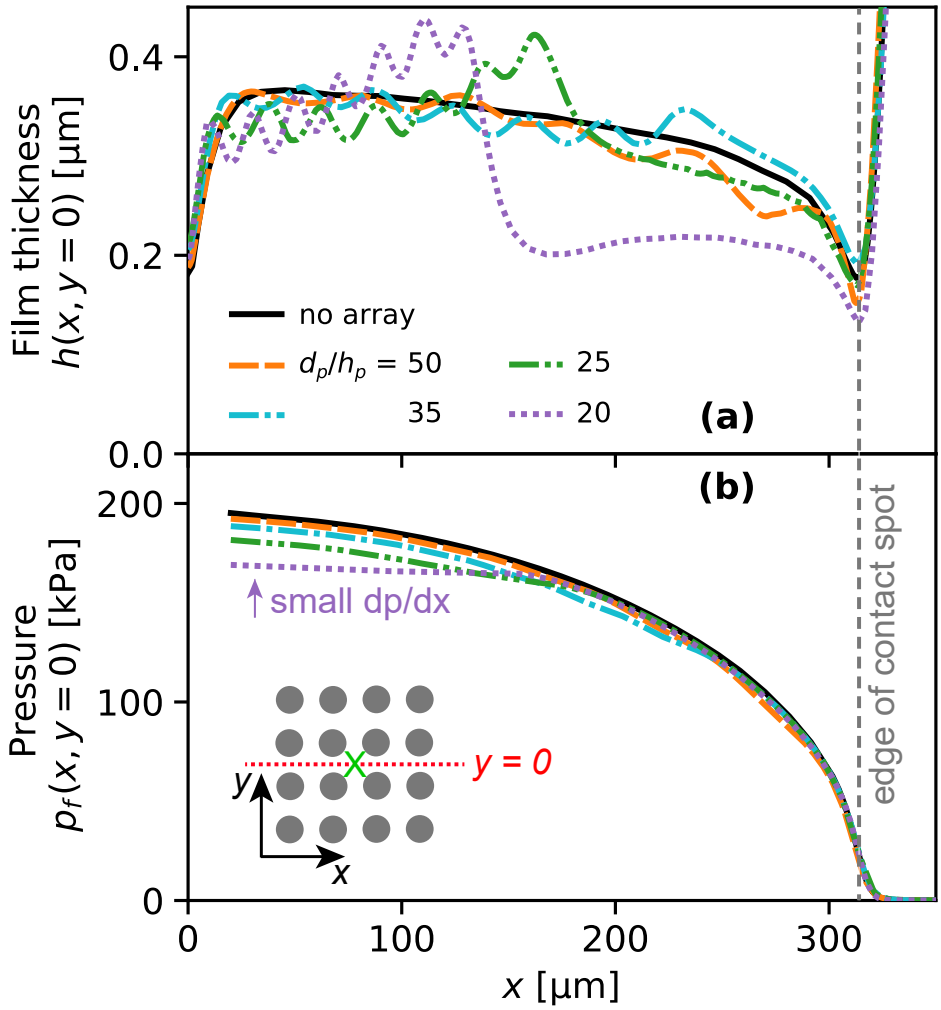

Figure 4.8: Numerical simulations of (a) the liquid film thickness $h(x, y = 0)$ and (b) the pressure $p_f(x, y = 0)$ right before dry spot nucleation for $h_p = 1\,\mu$m and different values of d_p. The red dotted line in the inset of (b) defines the cross-section, along which h and P_f are plotted. The green cross indicates the origin $(x, y) = (0, 0)$, i.e. the center of the contact spot.

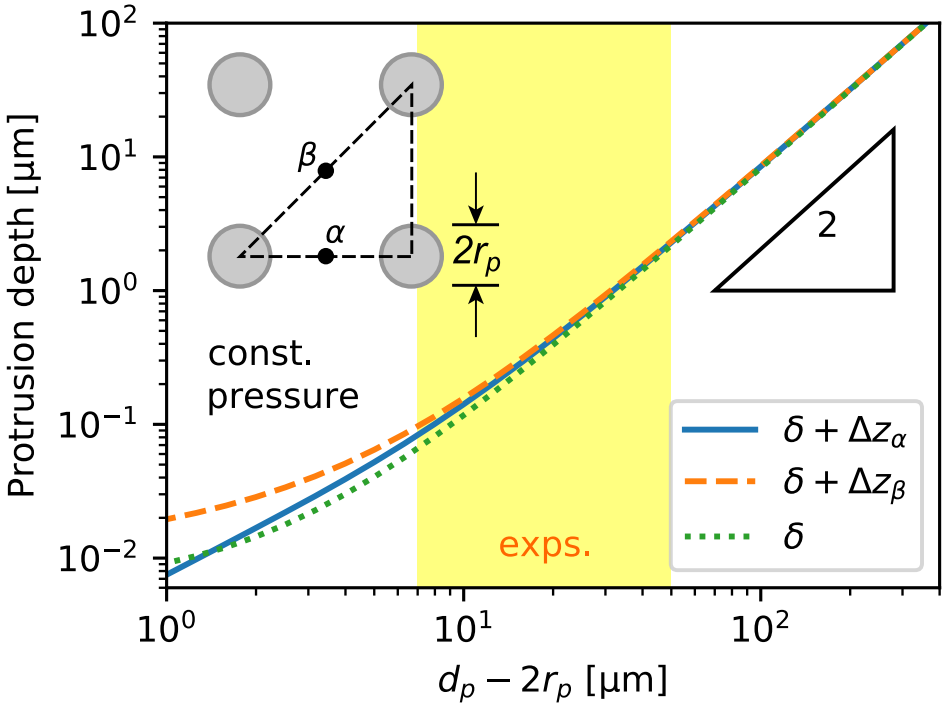

Figure 4.9: Numerical simulations of the deformation amplitude of a soft elastic halfspace ($Y = 1.365\,\mathrm{MPa}$, $\nu = 0.499$) indented by a rigid pillar array as a function of the gap width between neighboring pillars at constant average pressure. The inset defines the points α on the axis and β on the main diagonal of the square array. The yellow shaded area indicates the range of array periods used in the experiments. The triangle indicates a powerlaw scaling of $\delta + \Delta z \sim (d_p - 2r_p)^2$.

the array, but inside the contact spot, is thinner for $d_p \leq 22\,\mu\mathrm{m}$, because the dewetting starts later in these cases. The primary reason for the delay is the reduced squeeze-out flow speed for a denser array of micropillars.

Figure 4.9 presents numerical simulations of the dependence of δ and $\delta + \Delta z$ on the gap width between neighboring pillars at constant average pressure. The data correspond to a system in steady state, after transient effects have faded. The curves labeled α and β correspond to the symmetry points on the axis and the main diagonal of the square array, respectively, as illustrated in the inset. We conclude that for large array periods, Δz becomes negligible compared to δ.

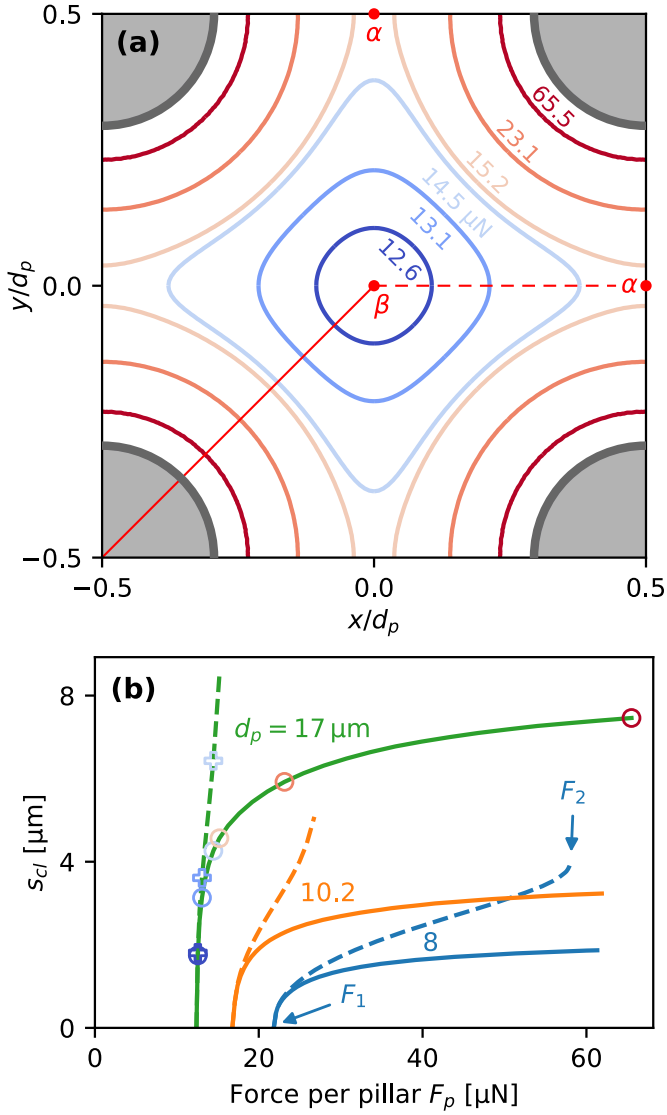

Figure 4.10: (a) Numerical simulations of the extension of the elastomer-substrate dry contact region for $d_p = 17\,\mu$m and different values of the force per pillar F_p. The gray shaded areas represent the pillars. (b) Extension of the dry contact spot along the main diagonal (solid lines) and the axis (dashed lines) of the square array for different values of d_p. The symbols overlaid on the lines for $d_p = 17\,\mu$m correspond to the data shown in (a).

In the stationary simulations shown in Fig. 4.9, the pillar height h_p was assumed to be essentially infinite, i.e. a possible solid-on-solid contact in the valleys between the pillars was not taken into account. A finite h_p would imply that $\delta + \Delta z$ does not exceed a maximum value of h_p in Fig. 4.9. This is rectified in the steady-state simulations in Fig. 4.10, where we allowed for a frictionless solid-solid contact according to Eq. (4.5).

In Fig. 4.10(a) we plot the shape and size of the elastomer-substrate dry contact region for $d_p/h_p = 17$ and different values of F_p. At a certain critical value F_1 of F_p, the elastomer makes contact with the substrate in the center of a unit cell of the square array, i.e. in the point labeled β in Fig. 4.10(a). For larger values of F_p, the dry contact region increases in size. At a second critical value F_2 of F_p, the previously disconnected contact of neighboring unit cells merge and become connected over a lengthscale by far exceeding the array period d_p. This is a prerequisite for dewetting the entire pillar array. For $F_p < F_1$, the regions available to the liquid are continuous and connected, whereas for $F_p > F_2$, they become disconnected rings around the individual pillars as visible in Figs. 4.4 to 4.6.

Figure 4.10(b) shows the extension of the dry contact spot s_{cl} relative to the point labeled β along the main diagonal (solid lines) and the axis (dashed lines) of the square array for different values of d_p. The dashed lines terminate at a value of $s_{cl} = d_p/2$. The solid lines asymptote to a value of $\frac{\sqrt{2}}{2} d_p - r_p$ in the limit of $F_p \to \infty$. For $d_p \gg 2r_p$, the critical values F_1 and F_2 are of similar magnitude, whereas F_2 can greatly exceed F_1 for $d_p \approx 2r_p$.

4.4.3 Discussion

There exists a minimum value of d_p or conversely maximum values of h_p or Y, below or above which dewetting of the interstitial regions can no longer occur. The reason is that the applied force becomes insufficient for the protrusions of the deformed hemisphere to reach the bottom of the substrate.

To develop intuition, we consider the classical problem of contact mechanics of a single, rigid cylindrical punch indenting an elastic halfspace.[143] In this case, the steady-state indentation depth $\delta \sim F_p/Y$ is proportional to the applied force and inversely proportional

to Young's modulus. We expect that this scaling applies to the case of a pillar array indenting an elastic halfspace at large values of the array period d_p. In this case, the force per micropillar is given by $F_p \sim d_p^2 p_{\mathrm{av}}$, where p_{av} is the average pressure acting on the pillar array. Consequently, we expect the indentation depth to scale as

$$\delta \sim d_p^2 / Y \ . \tag{4.6}$$

The triangle in Fig. 4.9 indicates that for large periods a powerlaw relation $\delta + \Delta z \sim (d_p - 2r_p)^2$ is a good approximation to the numerical data. Since in the limit of large periods $\Delta z \ll \delta$ and $d_p \gg 2r_p$ hold, we indeed recover the expected scaling. We note that in our experiments we kept the contact spot radius constant, which implies that the average pressure scales with Young's modulus. This does not affect the $\delta \sim d_p^2$ scaling, however it makes the static deformation insensitive to Y.

For dense arrays the non-linear relation (4.6) implies that locally larger periods induce locally larger protrusion amplitudes $\delta + \Delta z$ and locally higher film pressures p_f, both of which speed up film thinning and dry-spot nucleation. In other words, unavoidable fluctuations in the pillar spacings or pillar dimensions are amplified in terms of their impact on where dewetted areas nucleate for small values of d_p/h_p. We believe that this increased sensitivity to the array imperfections is a contributing factor to the irregular shapes of the dewetted areas observed in Fig. 4.4(b) as d_p/h_p decreases.

As indicated by Figs. 4.7(a) and 4.8(a), the dewetting time and the expansion rate of the dewetted area along the array axes are almost the same for sparse arrays $d_p/h_p \geq 25$. For dense arrays $d_p/h_p \leq 22$, the dewetting time increases and the expansion rate significantly decreases. The origin of the slowdown is the concomitant reduction of the pressure p_f inbetween rows of pillars as visible in Fig. 4.8(b) for $d_p \leq 25\,\mu$m. A larger fraction of the externally applied, overall contact force is acting on top of the pillars and used up in generating the protrusions, which explains the decreased values of p_f and $\mathrm{d}p_f/\mathrm{d}x$. It is the gradient of the pressure distribution, which determines the speed with which the liquid is driven out of the array and out of the contact spot.

In our experience, dewetting in an elastomer - Fomblin Y - glass system in the absence of pillars suffers from sensitivity to surface heterogeneities and the boundaries of the contact area tend to have a

ragged morphology. For a system containing micropillars, as pointed out above, the contact pressure in the interstitial space between neighboring pillars is greatly reduced for small values of d_p. Consequently, we expect an increased sensitivity of the dry spot morphology to surface imperfections in this regime. Besides geometric fluctuations, therefore, also fluctuations in the elastic properties and the surface energies can contribute to the irregular growth mode observed in Fig. 4.4(b).

An interesting question concerns the nature of the correlation between the dewetting behavior studied in this manuscript and the achievable adhesion strength. Li *et al.* presented experiments of the adhesion between a flat elastomer layer and a plano-convex glass lens.[144] They observed dewetting of the contact spot for pure water, whereas for SDS surfactant concentrations exceeding 0.03% dewetting no longer occurred, which they attributed to the stabilizing effect of double-layer repulsion. The measured adhesion strength diminished by a factor of 4 compared to the case of pure water.

Generally, dewetting is controlled by the disjoining pressure isotherm, which is a material property reflecting molecular interactions between all solid and liquid phases involved. The same interactions also govern the van der Waals attraction responsible for the dry adhesion of molecularly smooth solid surfaces. In practice surfaces are rarely molecularly flat and a plethora of other phenomena determine the effective strength of adhesion, such as surface roughness,[145, 146] viscous forces,[147, 148] surface tension forces,[148, 149], non-Newtonian liquid rheology,[150] the three-dimensional surface geometry,[151] or viscoelastic bulk properties of soft materials.[145, 152] Therefore, the correlation between dewetting and adhesion needs to be studied separately in each case.

For technological applications, the time required until a high adhesive state is reached and dewetting is complete is relevant. This lag time is composed of the thinning time of the liquid film inbetween the objects until dewetting commences and the subsequent dewetting time until the dewetted area reaches the edge of the contact spot. As shown in Fig. 4.7 the dewetting time increases with decreasing pillar spacing. The thinning time can be divided into the time Δt_{top} until the tops of the pillars dewet and Δt_{base} until the base plane of the pillar starts dewetting. Δt_{top} benefits from larger d_p due to channeling,[153–155] i.e. the efficient removal of the intervening liquid

through the interstitial space between the pillars. Δt_{base} increases with decreasing d_p, due to the reduced effective contact pressure inbetween the pillars. In our experiments using Fomblin Y, the overall time scale typically ranged from 0.5 to 5 minutes. For water, which has a much lower viscosity, we expect this time to be reduced by two orders of magnitude.

4.5 Summary and conclusions

The morphology of dewetted areas forming in a thin liquid film confined between a periodic micropillar array and a soft, elastic surface depends sensitively on the pillar height and spacing. For large ratios of array period to micropillar height and width, the dewetted areas tend to be diamond-shaped and expand at a rate almost the same as for a flat, unpatterned substrate. For a small ratio, the shapes of the dewetted areas become irregular and their expansion rate is significantly reduced.

We developed a fully-coupled numerical model based on linear elasticity, the Reynolds equation and a disjoining pressure formalism. The simulations reproduce the key features observed in the experiments very well. We found that for the smallest array periods studied, the pressure gradient becomes noticeably smaller inside the array, which explains the observed delay of the onset of dewetting. For a larger average contact pressure, the elastomer protrudes further into the gap space between neighboring pillars. We found that the protrusion amplitude scales to good approximation as the square of the array period at constant pressure. This non-linear dependence implies an increased sensitivity of the dewetting dynamics to fluctuations in the pillar shape, height and spacing in the limit of small periods. Furthermore, systems with small pillar spacing exhibit a reduced interstitial contact pressure, which makes them more sensitive to any material or surface irregularities. These two effects combined are the likely origin of the observed morphological difference.

In underwater adhesive systems, the adhesion force is usually provided by solid-solid contact of the tops of the pillars. The interstitial space between the pillars has a passive role of enabling a fast and efficient drainage of the liquid phase[153–155]. Micropillar arrays are advantageous in that respect due to the connectedness of their interstitial space. We have considered a very soft material with a Young's

modulus comparable to human skin[156] that deforms elastically upon contact and thereby induces dewetting in-between the pillars. In this fashion the area of solid-on-solid contact is increased thereby likely enhancing adhesion. Moreover, we expect that the elastic deformation of the soft surface increases the stability of the adhesive contact to lateral motion due to mechanical interlocking.

Acknowledgement

Vaishali Chopra prepared the samples and helped me with the experiments. I would like to thank her, Dr. René Hensel and Prof. Eduard Arzt from the Leibniz-Institut für Neue Materialien, Saarbrücken, for their contribution.

Chapter 5

Enhancing Dry Adhesion of Polymeric Micropatterns by Electric Fields

5.1 Introduction

In the course of the automation of industrial manufacturing processes, the handling of components is increasingly realized by machines and robots. The size of objects and components ranges from several microns to meters. To date, vacuum grippers are widely used in pick-and-place applications with high precision in positioning.[157] Mechanical, magnetic and electromagnetic grippers offer alternatives for specific applications, but are used less frequently. Another fairly new approach is the utilization of micropatterned adhesives.[158–161] Their performance relies mainly on van der Waals interactions and contact mechanics, which are controlled by mechanical properties and the proper design and arrangement of the microstructures within the adhesive array.[122,162,163]

Pick-and-place applications necessitate a controllable switch between a high (pick) and a low (release) adhesive regime. Several examples for external stimuli to switch adhesion of micropatterned adhesives have been reported, including compressive loads,[164,165] thermal heating,[166,167] magnetic fields,[168,169] pneumatic control,[161,170] and UV exposure.[171] Almost all mentioned strategies require specific designs or material selection, which potentially limit the range of application. In addition, most concepts allow switching between "on" and "off" states,

but no specific adjustability to the required adhesion performance.

An approach to control adhesion during operation is electroadhesion. Here, the adhesion force nominally scales (among other parameters) with $|\mathbf{E}|^2$, where $\mathbf{E}$ is the applied electrical field.[172] Electroadhesion functions for both conductive and insulating targets[173–175] and is, for example, used in semiconductor wafer handling[176] or microhandling.[177] Recently, electroadhesion has been combined with micropatterned adhesives for applications such as wall climbing robots[178] and flexible grippers.[179] Spenko et al. and Menon et al. have successfully demonstrated that the combination of both concepts improves shear adhesion, as the normal force induced by electrical fringe fields enables closer contacts with higher friction.[180,181]

Electroadhesion devices typically make use of interdigitated electrode arrays to maximize the spatial extent of regions with high electric field strength and high field gradients.[174] The traditional electrostatic models predict a dependence of the electroadhesion force on the square of the applied voltage difference.[172] In contrast, our experimental data and many experimental data reported in literature do not exhibit such a square dependence.[173,182–184] No explanation for this discrepancy has been suggested to date. In this manuscript we demonstrate for the first time that a non-square dependence can arise by considering miniscule, but non-zero, *field-dependent* electrical conductivities of the materials involved.

Below we present details of the experimental setup and the electroadhesion device fabrication in Section II as well as extensive experimental results in Section III. A description of theoretical models both for electrically insulating and electrically conductive materials is given in Section IV, followed by an in-depth numerical evaluation of the models and a comparison with the experimental data in Section V.

5.2 Materials and methods

5.2.1 Device fabrication

For the micropatterned-electro adhesive device, micropatterned adhesive films were transferred onto interdigitated comb electrodes. Micropatterned adhesive films consisting of microarrays of cylindri-

cal pillars were fabricated by replica molding. The diameter and height of each pillar was 7 µm (aspect ratio 1:1). Micropillars were arranged in a hexagonal lattice with 14 µm center-to-center distance. The backing layer thickness was . For replica molding, UV-curable perfluoropolyether-dimethacrylate (Fomblin MD40, Solvay, Bollate, Italy) was used as template material. The pre-polymer contained 0.5 wt% of a photoinitiator (2-hydroxy-2 methyl-propiophenone, Sigma Aldrich, Taufkirchen, Germany). The mixture was poured over a micropatterned silicone master structure and covered with a microscope glass slide. The pre-polymer mixture was exposed to UV (wavelength 365 nm, Omnicure S1500, Excelitas Technologies) in a nitrogen atmosphere for 5 min. The cured template was carefully peeled and served as template for the adhesive films. Micropatterned adhesive films were made from polydimethylsiloxane (PDMS, Sylgard 184, Dow Corning, Midland, MI, USA). PDMS was prepared by mixing ten parts of the base material with one part of the curing agent using a speed mixer (DAC600.2 VAC-P, Hauschild Engineering, Hamm, Germany) at 2350 rpm for 3 min. The mixture was poured over the template and covered with interdigitated electrodes (IDEAU200, Deutsche METROHM GmbH & Co. KG, Filderstadt, Germany). Prior to this, the electrodes were treated with oxygen plasma for 3 min. Electrodes had a width of 220 µm and a gap between oppositely charged electrodes of 160 µm. A fixture was used to clamp the Fomblin MD40 template, the electrodes and the intermediate liquid PDMS layer to set the desired back layer thickness of the micropatterned adhesive film. The whole setup was placed into an oven and thermally cured at 95 °C for 20 minutes and finally demolded.

5.2.2 Electroadhesion setup

The normal adhesion was characterized using a custom built setup. A spherical glass lens with a curvature radius of 15.5 mm (Edmund Optics GmbH, Mainz, Germany) was used as probe. The probe was mounted to a load cell (KD 34s ME-Meßsysteme, Hennigsdorf, Germany) to measure normal forces. Probe and load cell were displaced using a linear stage (Q-545 Q-Motion, Physik Instrumente GmbH & Co. KG, Karlsruhe, Germany). The micropatterned electro-adhesive device was mounted below the probe and connected to a DC high-voltage power

supply (HCN 14-3500, FuG Electronik GmbH, Schechen, Germany). A LabVIEW program was developed to control the electro-adhesion setup. To reduce residual charges upon each measurement in the presence of an electrical field, probe and adhesive film were treated by an antistatic gun (Zerostat 3 Anti-Static, SPI Supplies, Glasgow, UK). All experiments were performed in a laboratory with controlled temperature and relative humidity (RH) at 21 °C and $50 \pm 5\%$.

During approach, the spherical probe was brought in contact with the adhesive film. At maximum indentation depth, the compressive preload is highest. This position was held for 1 s, before the probe was retracted. In all experiments, approach and retraction velocities were 1 µm/s. The displacement of the probe, u, was calculated as follows: $u = u_M - F/k$, where u_M is the displacement of the motorized stage, F is the force and $k = 6.17$ kN/m is the machine stiffness. The absolute value of the maximum adhesive force at detachment was defined as pull-off force. Pull-off forces were converted into pull-off stresses by dividing them with the projected contact area A_p at maximum compressive preload. The projected contact area was determined by the geometrical formula $A_p = \pi \left[R_p^2 - (R_p - u_p)^2\right]$, where $R_p = 15.5$ mm is the curvature radius of the probe and u_p is the distance from contact to maximum indentation of the probe into the micropatterned adhesive film.

5.3 Experimental results

The micropatterned-electro adhesive device was fabricated by combining an elastomeric micropatterned film with an interdigitated comb electrode array as shown in Fig. 5.1. The diameter and height of the micropillars were 7 µm. The pillars were arranged hexagonally with a center-to-center distance of 14 µm, which is one order of magnitude smaller compared to the width (220 µm) and distance (160 µm) between the electrodes. In addition, the backing layer was 55 ± 5 µm, which again is one order of magnitude larger than the pillar height. Thus, we assume that the characteristics of the electrical fringe field were not influenced by the spatial orientation of the pillar array in relation to the direction of the electrodes.

Results of adhesion tests for different applied voltages are shown in Fig. 5.2. Figure 5.2(a) compares results with (1.8 kV) and without

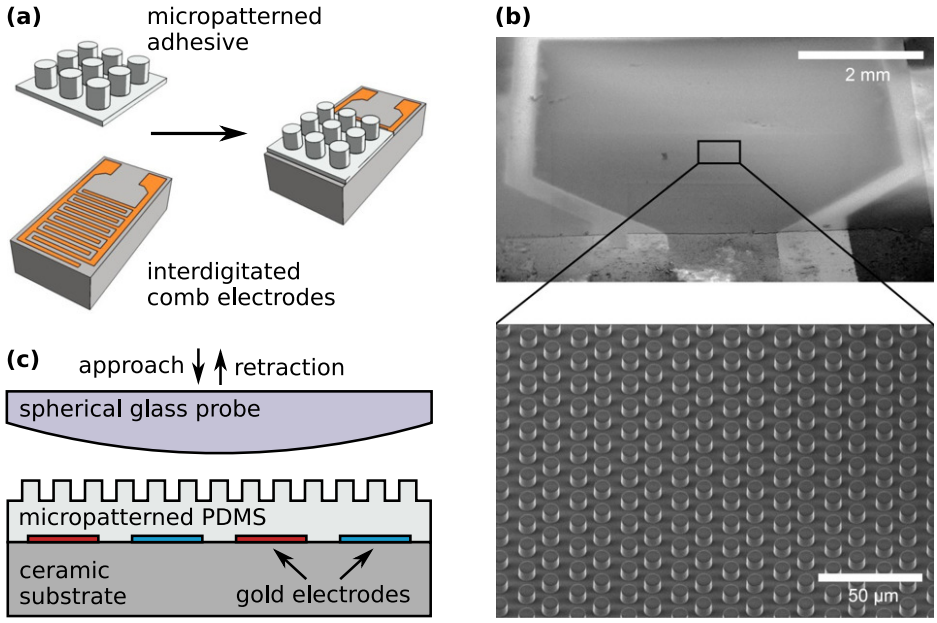

Figure 5.1: The micropatterned-electro adhesive device. (a) Illustration of the fabrication process. A micropatterned adhesive film was generated via replica molding and, subsequently, deposited on the interdigitated comb electrodes. (b) Scheme of the adhesion test setup to record normal force acting on the probe and the probe displacement u. During the test a spherical glass probe was attached (approach) and detached (retraction) at different applied voltages. (c) Scanning electron micrograph of the micropatterned-electro adhesive device. The inset shows the micropillars.

(0 kV) applied electrical field. Without applied field (black curve), the normal force was zero before the probe contacted the micropatterned surface ($u \geq 0$ µm). Contact was established by pressing the probe into the adhesive film (indentation) with a preset displacement of -2.3 µm. At that position, the maximum compressive preload of 30 mN was achieved. Upon holding for 1 s, the probe was retracted. The probe detached from the surface at a maximum tensile force of -7 mN, i.e. a pull-off force of 7 mN. In the presence of an electrical field (red curve), the probe already experienced an attractive force before contact (for $u \lesssim 70$ µm). At contact, the attractive force due to the electrical field was -5 mN. The maximum compressive preload reduced apparently to 25 mN for a similar indentation of -2.3 µm in relation to the experiment without electrical field. The attractive electrostatic force further caused earlier contact at $u = 1.1$ µm. This effect is related to the elastically deformable setup with a machine stiffness of 6.17 kN/m and constant motor displacement for all measurements. The maximum tensile force was -12 mN, that is a pull-off force of 12 mN. Upon detachment, the force gradually decreased with increasing distance between the probe and the adhesive, similarly compared to the approach. The slightly higher attractive force (about 1 mN) during retraction compared to the approach is most likely related to residual charges upon separation of contact.

Figure 5.2(b) shows the pull-off force as a function of the net preload for various applied voltages. The pull-off forces increased with the applied voltage and at 2 kV were twice as high as at 0 kV. With increasing voltage, the net preload decreased for constant displacements due to increasing electrostatic attraction between the adhesive and the probe. Although the probe was spherical, pull-off forces were insensitive to preload, as all measurements were performed in saturation conditions, i.e. pull-off force is larger than preload.[185] Figure 5.2(c) summarizes the pull-off forces in terms of applied voltages. Pull-off forces and stresses increased with increasing electric fields, which suggests that the electrostatic forces superimpose the van der Waals forces.

Importantly, the electrostatic force contributed to the contact formation of the probe with the adhesive, which led to a reduced net preload although the displacement form first contact to maximum indentation was kept constant. Thus, the net preload reduced with

increasing voltage as shown in Fig. 5.2(d). For small indentations such as 0.9 µm, the net preload turns negative for voltages larger 1.5 kV. Here, the requisite compressive force of the probe to adhere to the surface was realized solely by electrostatic forces without mechanical compression. For applications, this offers an opportunity to adhere to very fragile objects without applying mechanical compression or to enhance adhesion to rough surfaces.[175]

5.4 Theoretical models

The achievable adhesion force can be enhanced by a switchable electric field-induced force exerted on the target object. Below we present theoretical models for different types of materials as well as their numerical implementation to predict the steady-state values of the electroadhesion force. We used the finite-element software Comsol 5.2.

5.4.1 Electrostatic interaction – insulating materials

We first consider a stationary electrostatic system that is composed of purely dielectric, i.e. electrically insulating materials. The electric field distribution is governed by Poisson's equation

$$\nabla \cdot (\varepsilon_0 \varepsilon_r \nabla V) = -\rho, \tag{5.1}$$

where ε_0 is the vacuum permittivity, ε_r is the relative permittivity of the respective material, V is the electric potential, ρ is the volume charge density. We assume the dielectric materials to be linear, non-dissipative, isotropic, and homogenous. We assume all material properties to be independent of elastic deformations. Moreover, we assume all surface and volume charge densities to be zero, except at the surface of the electrodes.

5.4.2 Bulk-conductive materials

We now consider all materials to be electrically conductive. This is motivated by the fact that, in the experiments, the electric field strength is comparable to or even above the dielectric breakdown

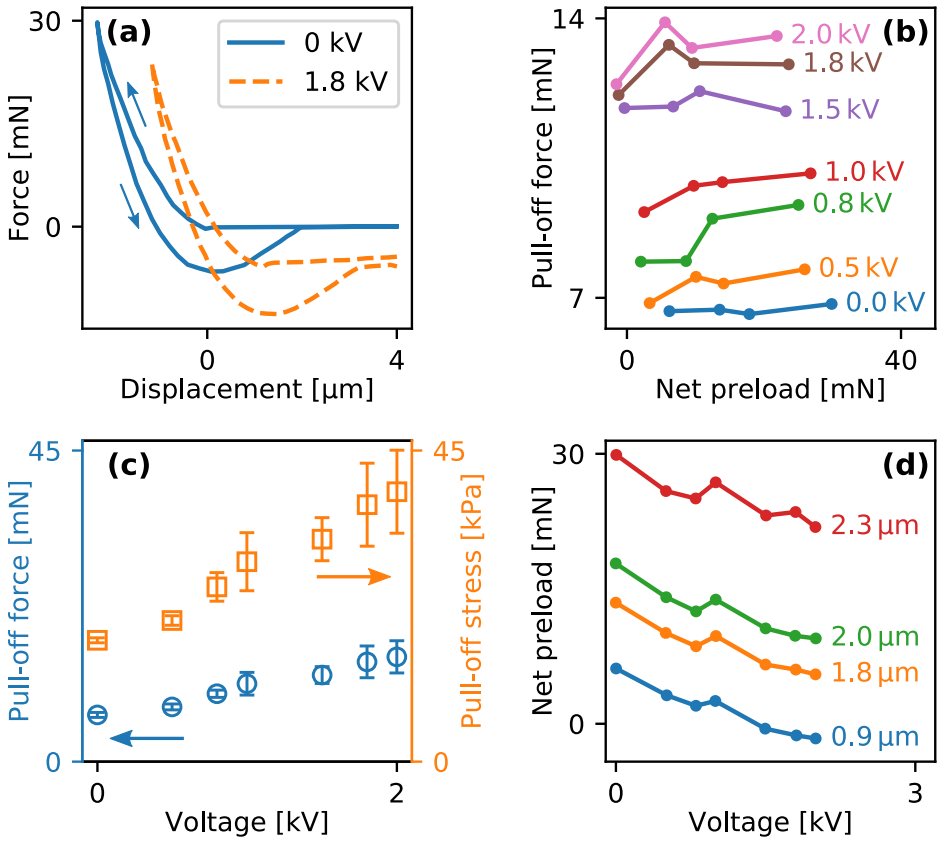

Figure 5.2: Experimental electroadhesion measurements. (a) Force-displacement curves for 0 kV (black) and 1.8 kV (red). Positive and negative forces are compressive and tensile forces, respectively. The inset presents data close to the contact of the probe with the micropatterned adhesive film. Arrows indicate the path during approach and retraction. (b) Pull-off forces in terms of net preloads for various applied voltages. Dashed lines highlight data for constant indentations. (c) Pull-off force (solid squares) and pull-off stress (open circles) as function of the applied voltage. (d) Net preload as function of the applied voltage. Numbers present the indentation into the micropatterned adhesive.

strength of air of approximately 3 MV/m. At such high electric fields many materials that are normally considered electrically insulating actually behave as weak conductors. This applies to air, the elastomer and possibly also the glass.[186–188]

We assume no external currents. We solve the continuity equation in steady state

$$\nabla \cdot \mathbf{J} = 0, \tag{5.2}$$

where $\mathbf{J} \equiv \sigma \mathbf{E}$ is the current density and σ is the electrical conductivity. Equation (2) is equivalent to

$$\nabla \cdot (-\sigma \nabla V) = 0\,. \tag{5.3}$$

5.4.3 Surface-conductivity of glass-air interfaces

In our experiments, we used glass lenses as substrates. The electrical bulk conductivity of glass at room temperature is almost unmeasurably small, i.e. essentially zero.[189] However, there is a significant electrical surface conductivity due to moisture adsorption that must be taken into account.[190–193]

The surface conductivity is implemented by assuming an ultralow low bulk conductivity of the lens (10^{-30} S/m) and an additional interfacial condition at the glass-air interface

$$\mathbf{n} \cdot \left(\mathbf{J^a} - \mathbf{J^b}\right) = \mathbf{n} \cdot \left(\sigma^a \mathbf{E^a} - \sigma^b \mathbf{E^b}\right) = -\nabla_t \cdot (\sigma_s \nabla_t V) \tag{5.4}$$

where ∇_t is a surface gradient operator, $\mathbf{n}$ is the unit normal vector of the interface and σ_s is the surface conductivity.

5.4.4 Variable air conductivity

At very high electric fields approaching the dielectric breakdown limit, the electrical conductivity of air σ_{air} is dependent on the electric field strength. Carlon has measured the electrical conductivity of air at very high relative humidities RH $\geq 66\%$.[194] He found that σ_{air} was constant for low fields and increased rapidly for $|\mathbf{E}|$ exceeding a certain threshold value E_c. The blue symbols in Fig. 5.3 are extracted from his measurements for RH = 66%. In this case, E_c is approximately 0.1 MV/m, which is substantially lower than the breakdown strength. He also observed very strong humidity dependence of the low field

conductivity. Several groups reported low field conductivities of air between 1 and 100 fS/m, depending on the geographic location, air pollution and atmospheric conditions.[186,187,195,196] Since quantitative measurements of field-dependent conductivity are scarce, we use an empirical relation that increases essentially linearly with field strength. For computational efficiency we assume the following empirical relation, which gives a smooth transition between the constant and linear regimes

$$\frac{\sigma_{\text{air}}}{\sigma_0} = 1 + s_L E_0 \log\left[1 + \exp\left(\frac{|\mathbf{E}| - E_c}{E_0}\right)\right], \tag{5.5}$$

where σ_0 is the zero-field air conductivity, E_c is a critical field strength below which conductivity is constant and above which it increases, $E_0 = 0.1$ MV/m defines the width of the transition region and s_L defines the slope. Curves of $\sigma_{\text{air}}(|\mathbf{E}|)$ for different values of E_c and s_L are illustrated in Fig. 5.3. We assume $\sigma_0 = 4$ fS/m as standard laboratory conditions usually correspond to relatively dry air (RH 30 to 40%).[186]

5.4.5 Electroadhesion force

The electroadhesion force F_{es} acting on a target object in a non-uniform electric field is derived from the Maxwell stress tensor T_{ij}, given as

$$T_{ij} = D_i E_j - \frac{1}{2}\delta_{ij} \sum_{k=1}^{3} D_k E_k \,, \tag{5.6}$$

where $E_i \equiv -\partial V/\partial x_i$ is the electric field, $D_i \equiv \varepsilon_0 \varepsilon_r E_i$ is the electric displacement field and δ_{ij} is the Kronecker delta. At a boundary between two materials a and b of different permittivities, the stress tensor T_{ij} is discontinuous, which causes a mechanical force density S_i to act on the boundary

$$S_i = \left(T_{ij}^a - T_{ij}^b\right) n_j \,. \tag{5.7}$$

The Maxwell stress vector S_i represents the electromechanical coupling. The total electroadhesion force is calculated by integrating S_z over the surface area A of the lens:

$$F_{es} = \oint S_z \mathrm{d}A. \tag{5.8}$$

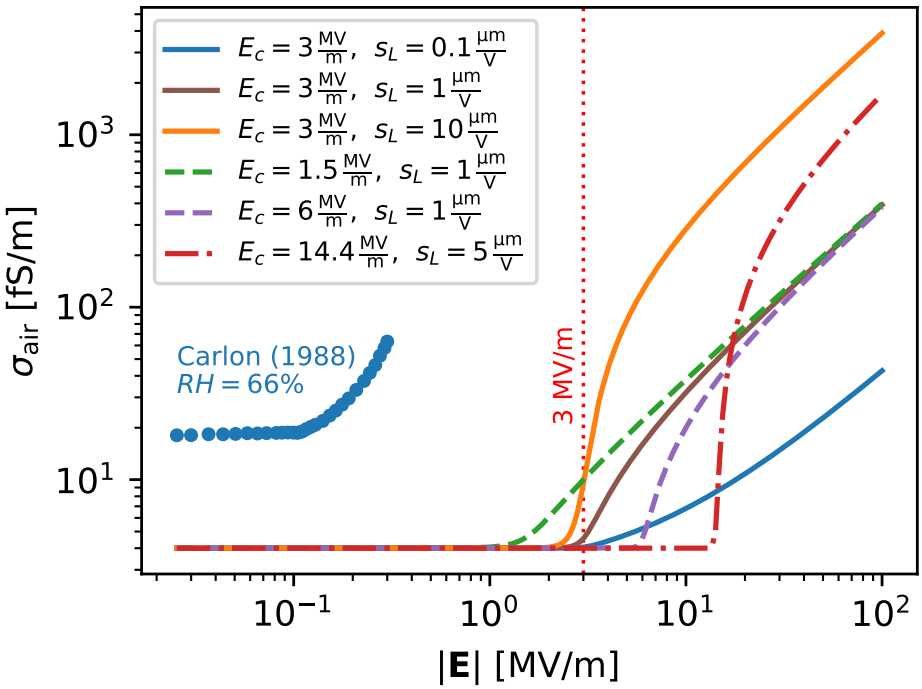

Figure 5.3: Models for the electric field-dependence of the air conductivity σ_{air} [Eq. (5.5)]. Solid lines vary the slope s_L for threshold value $E_c = 3$ MV/m, dashed lines vary E_c for $s_L = 1$ µm/V. The dash-dotted red line was found to match experimental results with $E_c = 14.4$ MV/m and $s_L = 5$ µm/V. Blue symbols are extracted from measurements in Carlon, H. R. (1988) for moist air (RH = 66%).[194]

5.4.6 Computational domain, boundary conditions and material properties

Figure 5.4 shows the model geometry. A glass lens is positioned above the electrode array. The width and length of the electrode array is $w_a = 2b\,(n-1) + 2a$ with n interdigitated stripe electrodes of width $2a$ and period $2b$ [Fig. 5.4(a)]. The electrode array is deposited on a ceramic substrate with thickness $h_c = 3\,\mathrm{mm}$, relative permittivity $\varepsilon_r = 10$ and conductivity $\sigma = 100\,\mathrm{fS/m}$. The array is covered with an elastomer layer of thickness $h_e = 55\ \mu\mathrm{m}$, relative permittivity $\varepsilon_e = 2.5$ and conductivity $\sigma_e = 25\ \mathrm{fS/m}$. The elastomer is covered with a hexagonal array of cylindrical micropillars. Due to the pillars being too small to be considered individually, we use an effective medium approximation. The effective medium has a thickness equal to the pillar height $h_p = 7\ \mu\mathrm{m}$. Its permittivity and conductance are derived from that of the elastomer and air, equal $\varphi\varepsilon_e + (1-\varphi)\,\varepsilon_{\mathrm{air}} \approx 1.34$ and $\varphi\sigma_e + (1-\varphi)\sigma_{\mathrm{air}} \approx 8.76\ \mathrm{fS/m}$, where $\varphi = \frac{\pi\sqrt{3}}{6}\left(\frac{2r_p}{d_p}\right)^2 \approx 0.227$ is the pillar array volume filling ratio, $r_p = 3.5\ \mu\mathrm{m}$ is the pillar radius and $d_p = 14\ \mu\mathrm{m}$ the spacing of the pillars. The glass lens has a relative permittivity $\varepsilon_L = 5$, conductivity $\sigma_{\mathrm{L}} = 1\ \mathrm{pS/m}$, radius of curvature $R_L = 15.5\ \mathrm{mm}$, diameter $2a_L = 16\ \mathrm{mm}$, thickness $h_L = 4\ \mathrm{mm}$ and is placed $\delta = 1\,\mu\mathrm{m}$ above the pattern. Air is assumed to have a relative permittivity of 1 and conductivity $\sigma_{\mathrm{air}} = 4\ \mathrm{fS/m}$ at zero field strength. All geometric and material parameters are summarized in Tab. 5.1.

Due to symmetry we only consider a cuboidal quarter of the system with width $x_m = 20\ \mathrm{mm}$, length $y_m = 20\ \mathrm{mm}$ and height $z_m = 40\ \mathrm{mm}$. The glass lens is positioned above the electrode array [Fig. 5.4(b)]. A quarter of the electrode array has width and length $\frac{w_a}{2} = 3\ \mathrm{mm}$ and is composed of $n = 8$ electrodes of width $2a = 220\ \mu\mathrm{m}$ and period $2b = 380\ \mu\mathrm{m}$. At $y = 0$ there is a symmetry plane where $\mathbf{n}\cdot\mathbf{E} = 0$ holds. At $x = 0$, there is an antisymmetry plane where $V = 0$ holds. All other external boundaries are also considered to be symmetry planes and positioned distant enough (i.e. $x_m,\ y_m,\ z_m \gg \frac{w_a}{2}$) to have no influence on the solution.

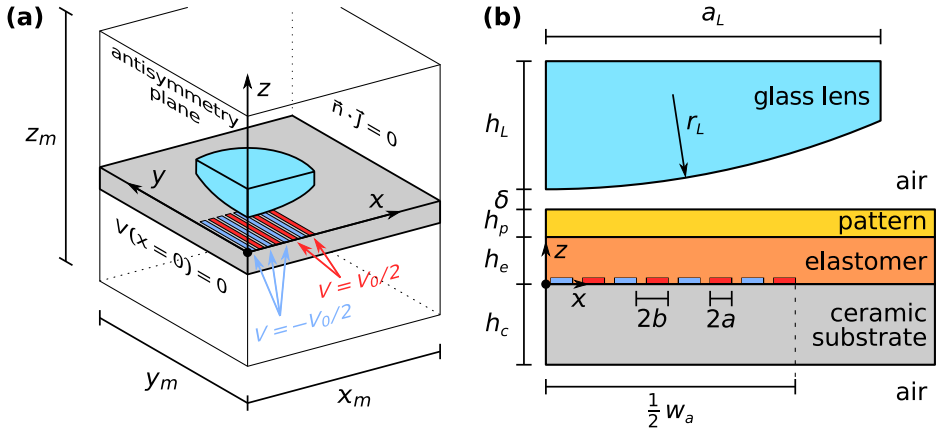

Figure 5.4: Schematic illustration of the computational model. (a) Cross-section ($y = 0$ plane) of the glass lens (purple, curvature radius R_L) placed above oppositely charged electrodes (red and blue stripes) located on a ceramic substrate (grey). The electrode array is covered with a thin elastomer layer with thickness h_e. The patterned surface is approximated by a thin homogenous effective medium layer with thickness h_p. (b) In the simulations, a cuboidal quarter of the experimental setup is considered, with a symmetry plane at $y = 0$ and an antisymmetry plane at $x = 0$.

Table 5.1: List of variables as well as geometric and material parameters used in the numerical simulations.

Material	Property	Symbol	Value	Unit	Ref.
Air	relative permittivity	ε_{air}	1	–	–
	conductivity	σ_{air}	$4 \cdot 10^{-15}$	S/m	[186]
	gap thickness	δ	10^{-6}	m	–
Lens	relative permittivity	ε_L	5	–	[197]
	conductivity	σ_L	10^{-12}	S/m	–
	surface conductivity	σ_s	$10^{-13\ldots-8}$	S	[198,199]
	radius	a_L	$8 \cdot 10^{-3}$	m	–
	radius of curvature	R_L	0.0155	m	–
	thickness	h_L	$4 \cdot 10^{-3}$	m	–
Pattern	pillar radius	r_p	$3.5 \cdot 10^{-6}$	m	–
	pillar height	h_p	$7 \cdot 10^{-6}$	m	–
	pillar spacing	d_p	$1.4 \cdot 10^{-5}$	m	–
Elastomer	relative permittivity	ε_e	2.5	–	[188]
	conductivity	σ_e	$2.5 \cdot 10^{-14}$	S/m	[188]
	thickness	h_e	$5.5 \cdot 10^{-5}$	m	–
Electrode array	electrode half-width	a	$1.1 \cdot 10^{-4}$	m	–
	half-period	b	$1.9 \cdot 10^{-4}$	m	–
	number of electrodes	n	16	–	–
	applied voltage	V_0	2000	V	–
Ceramic substrate	relative permittivity	ε_c	10	–	[200]
	conductivity	σ_c	10^{-13}	S/m	[201]
	thickness	h_c	$3 \cdot 10^{-3}$	m	–
Computational domain	width, length	x_m, y_m	0.02	m	–
	height	z_m	0.04	m	–

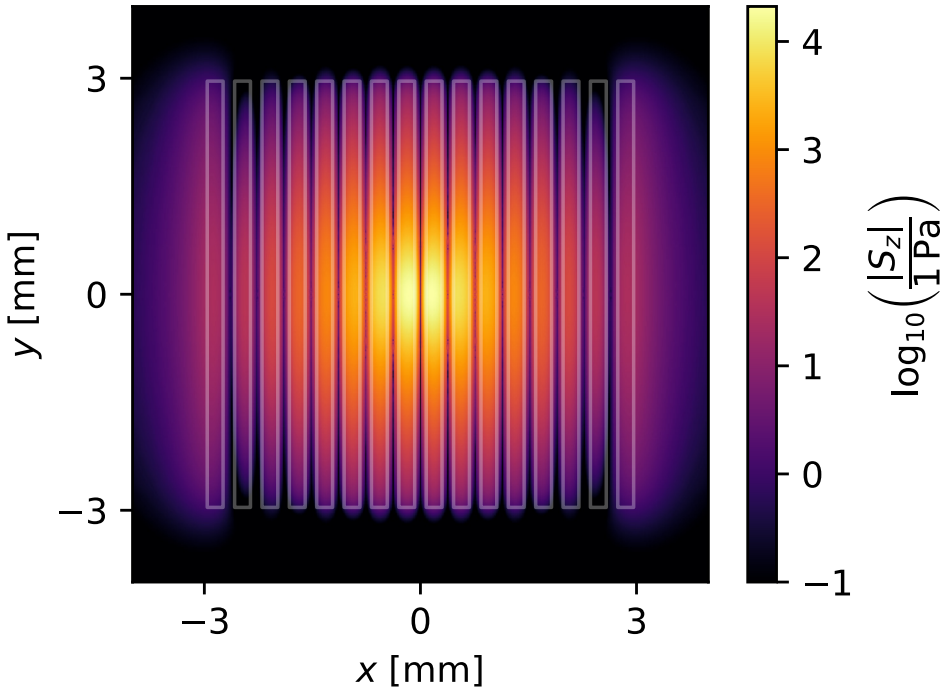

Figure 5.5: Logarithmic Maxwell stress map on the surface of the lens being located 1 µm above the micropatterned-electro adhesive device. The white lines indicate the shape and location of the electrode array.

5.5 Numerical results

Figure 5.5 shows an example of the Maxwell stress distribution $|S_z|$ on the lower surface of the lens. Faint white lines indicate the shape of the electrode array. Most of the attraction is concentrated directly above each electrode and near the center of the lens being located 1 µm above the micropatterned adhesive. The outermost electrodes exhibit a weak long-range attraction due to fringe fields.

Figure 5.6 shows the extracted electroadhesion force F_{es} acting on the lens in terms of the applied voltage, see Eq. (5.8). The black circles represent our experimental measurements. The dashed and dash-dotted black lines, both scaling as $F_{es} \sim V_0^2$, correspond to a constant air conductivity and the electrostatic model for insulating materials, respectively. It matches the experimental data well up to 800 V. Above that voltage the experiments no longer follow the quadratic

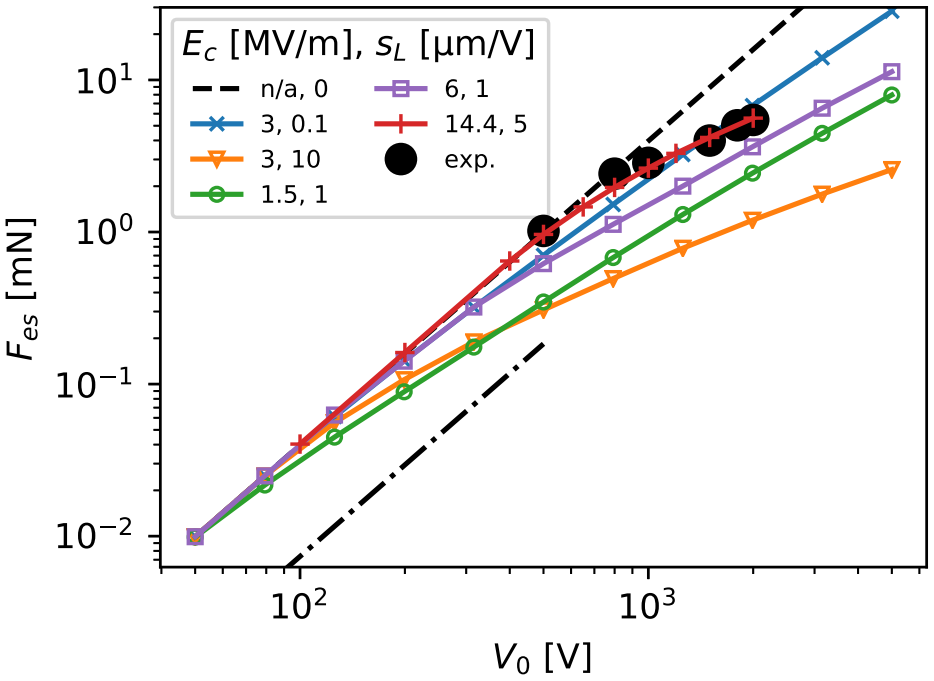

Figure 5.6: Numerical results of electroadhesion force as function of applied voltage for variable air conductivity according to Eq. (5.5) with threshold value E_c and slope s_L (compare Fig. 5.3). Black circles represent experimental results. The dashed black line assumes constant air conductivity. The dash-dotted black line corresponds to the electrostatic model.

force-voltage dependence predicted by this model. Other symbols in Fig. 5.6 correspond to a field-dependent air conductivity according to Eq. (5.5). The electroadhesion force is proportional to V_0^2 for low voltages, but exhibits a weaker scaling when $E > E_c$. The best fit is obtained for parameter values $E_c = 14.4$ MV/m and $s_L = 5$ µm/V (red crosses). A comparison of the data for $E_c = 3$ MV/m and $s_L = 0.1$ and 10 µm/V (orange and blue lines) illustrate that larger value of s_L induces a weaker dependence of F_{es} on V_0 for $E \gg E_c$. Variations of E_c (green and violet lines) determine at which voltage level the deviation from the square scaling occurs.

A comparison of the models introduced in section 4 and specifically the effect of air conductivity and electric parameters are shown in

Figs. 5.7 and 5.8. First, the influence of the field-independent surface conductivity of the lens σ_s (blue crosses) and the field-independent bulk conductivity of the lens σ_L (red circles) on the electroadhesion force F_{es} is displayed in Fig. 5.7. In both cases, F_{es} increases for a more conductive lens. We conclude that the two models give virtually identical results, if the value of σ_s is chosen as $\sigma_s = \lambda\sigma_L$, where $\lambda \approx 122$ µm for our system. The line represents a fit based on the function

$$F_{es}(\sigma) = c_0 + \frac{c_1}{1 + c_2/\sigma}\,, \tag{5.9}$$

where c_0, c_1 and c_2 are fit parameters. The dashed vertical line corresponds to the (field-independent) air conductivity σ_{air}. When $\sigma_L = \sigma_{\text{air}}$, the force crosses zero. Due to lower computational cost, the bulk conductivity model was chosen for further calculations, though the surface conductivity model being more physically relevant.

In Fig. 5.8(a), we show the dependence of F_{es} on the (field-independent) conductivity of air σ_{air} (red points) and the elastomer σ_e (violet squares). F_{es} decreases with increasing σ_{air}. Consequently, if σ_{air} increases with field strength, the force will be lower. F_{es} substantially increases with increasing σ_e, which can provide an additional parameter for tuning electroadhesion devices. Figure 5.8(b) shows the increase of F_{es} with increasing relative permittivities of the lens ε_L and the elastomer ε_e for purely dielectric materials. Figure 5.8(c) shows F_{es} in terms of the entire electrode array width and length w_a while keeping the number of electrodes and the ratio $\frac{a}{b}$ constant. The electroadhesion force increases with larger w_a. For $w_a \approx 5$ mm, the force saturates as the array is much larger than the area of low separation and high attraction due to the curvature of the lens (compare Fig. 5.5). Figure 5.8(d) shows how F_{es} varies with elastomer thickness h_e. For large thickness, this relation is exponential as illustrated with exponential fits (solid lines). For small separation the extracted force is higher than the long-range exponential fit. The dependence of the force on electrode width-period ratio $\frac{a}{b}$ is given in the Electronic Supporting Information.

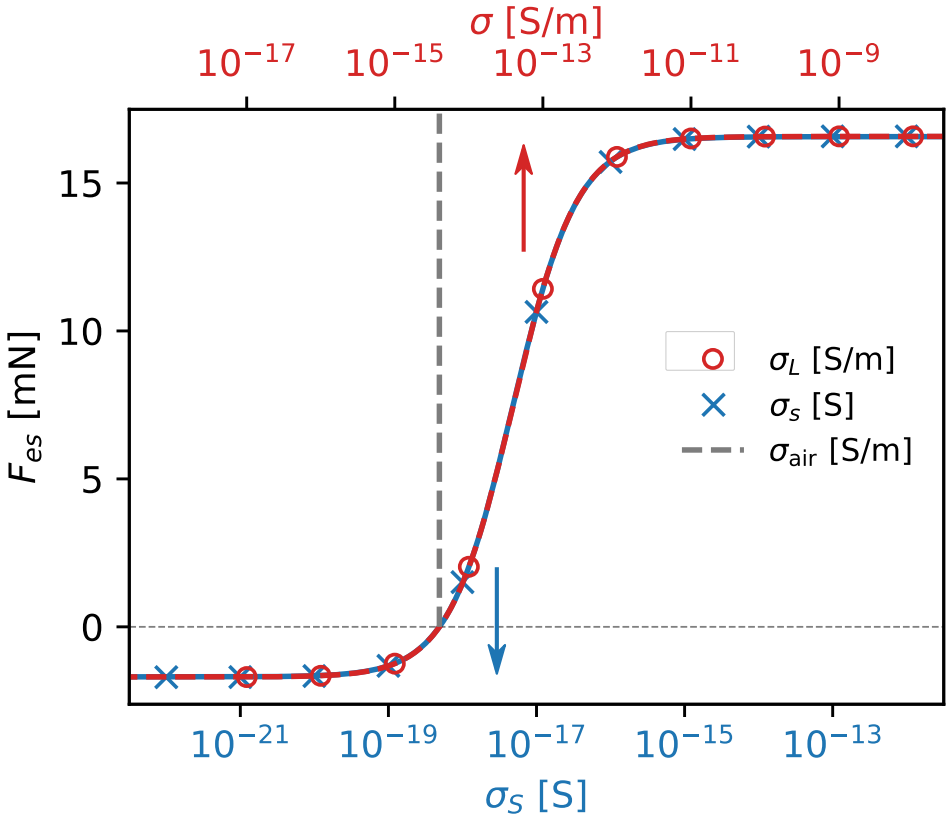

Figure 5.7: A comparison of the surface and bulk conductivity models: F_{es} in terms of the field-independent surface (σ_s, blue crosses) or bulk (σ, red circles) conductivity of the lens. Solid blue and red dashed lines are fits based on the logistic function, compare Eq. (5.9). In the bulk conductivity model, the fitted function crosses zero force for a lens conductivity being equal to that of air (dashed grey line).

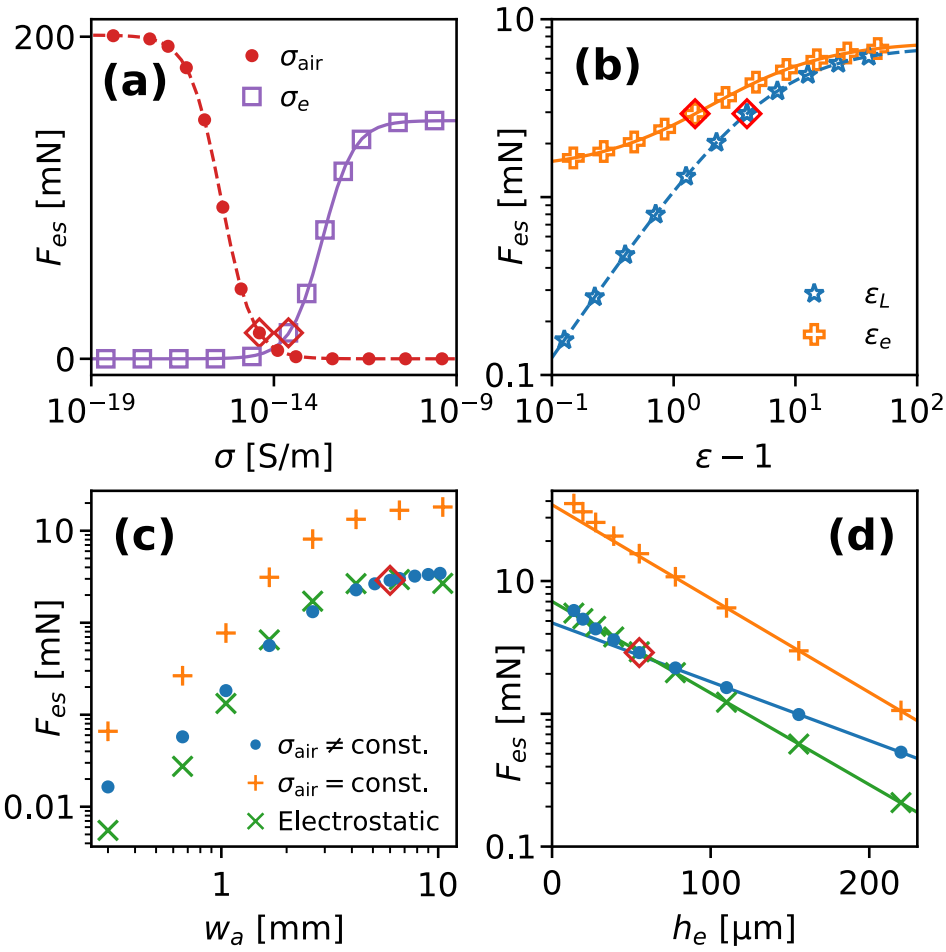

Figure 5.8: Effect of air conductivity and influence of electric parameters on electroadhesive force. (a) Electroadhesive force as a function of air conductivity (σ_{air}, red circles) and elastomer conductivity (σ_e, blue squares). (b) Electroadhesive force as a function of lens permittivity (ε_L, brown squares) and elastomer permittivity (ε_e, violet circles). (c,d) Electroadhesive force in terms of (d) the size of the electrode array w_a and (d) the thickness of the elastomer film h_e for linearly varying air conductivity (red stars, $E_c = 3$ MV/m and $s_L = 1$ µm/V), field-independent air conductivity (orange pluses) and in the electrostatic model (blue circles). The lines in (d) represent exponential fits to the three thickest films of each data set. As a reference, the green diamonds in (a-d) represent the parameter values stated in Tab. 5.1.

5.6 Discussion

We have fabricated and evaluated a micropatterned electroadhesion device based on an interdigitated electrode and a polymer micropillar array. Attractive forces before and after contact were caused by long-range electrostatic forces, while during contact the short-range van der Waals forces additionally contribute to adhesion. The traditional theoretical models for electroadhesion consider purely dielectric materials, i.e. electrical insulators, for which the electroadhesion force scales quadratically with applied voltage. This is however in contrast to our experimental results as well as previous ones reported in literature,[182–184] where a weaker force-voltage scaling has been observed. We have shown that accounting for minute but finite electric field-dependent electrical conductivities of air and the solid materials used for the electroadhesion device can quantitatively reproduce the experimental results.

The conductivities of the typical materials involved in an electroadhesion device can vary vastly. The surface conductivity of glass can change by seven orders of magnitude depending on the relative humidity and is sensitive to surface contamination e.g. due to fingerprints or residues upon repeated attachment and detachment cycles.[202] The bulk conductivity of polymers can vary strongly depending on impurity concentrations and production methods. Moreover, the conductivity of air depends on the relative humidity and the geographic microlocation of the measurement. Guo et al[183] reported a drop in electroadhesion force exerted on a glass target substrate by approximately a factor of 3 over the course of 3 days when the relative humidity decreased from approximately 64% to 43%. This is qualitatively consistent with the variation observed in Fig. 7(a). These results and considerations point at the need for tightly controlled environmental parameters to achieve a stable and reproducible electroadhesion performance.

5.7 Conclusions

Our experimental and numerical approach successfully revealed how short-range van der Waals interactions can be superimposed by long-range electrostatic forces, which enables in-line regulation of preload and adhesion forces. The following conclusions can be drawn:

1. The presence of electrostatic fields enhances adhesion. Up to 800 V, the adhesion force scales with square of the applied voltage. For voltages larger 800 V, the scaling is weaker, which is likely due to a small, field-dependent electrical conductivity of the materials involved.

2. Numerical results were similar for bulk-conductive materials and a model presuming surface-conductivity of glass-air interfaces. The latter has physical relevance due to possible adsorbed water films or residues through repeated adherence and detachment cycles.

3. Numerical results indicate that the electrical adhesive force increases with decreasing thickness of the micropatterned elastomer film and its increasing permittivity and conductivity. The electroadhesive force is highly sensitive to the environmental conditions. In particular, the force decreases with increasing air conductivity, which is directly related to humidity.

Acknowledgement

Vaishali Chopra performed all the experiments. I would like to thank her, Dr. René Hensel and Prof. Eduard Arzt from the Leibniz-Institut für Neue Materialien, Saarbrücken, for their contribution.

Chapter 6

Conclusions and suggestions for future work

Dewetting at soft interfaces is a broad field, where a variety of phenomena can be observed and studied. The movement of the contact line can be strongly influenced by the contact pressure distribution, surface morphology or roughness. These effects could be utilized to develop functional surfaces with predictable and reproducible mechanisms of liquid removal or retention upon contact. This in turn can be used for instance to allow strong and switchable underwater adhesion.

Soft elastohydrodynamic dewetting phenomena observed in experiments can be reproduced with a numerical model, solving linear elastic deformation coupled with the Stokes equation of liquid flow and using the disjoining pressure formalism to include contact line movement. The influence of pressure distribution on contact line speed was confirmed experimentally. Dewetting along the rim of a contact spot exhibits constant contact line speed.

Liquid droplets at soft interfaces can move with a velocity proportional to the local contact pressure gradient and exhibit total coalescence or move much more slowly and undergo non-inertial partial coalescence cascades. The proposed numerical model reproduces the total coalescence.

Dewetting on patterned surfaces tends to be anisotropic, with contact line moving faster along the rows of the micropillars in a sparse square array. Dense square arrays of pillars can lead to irregularly-shaped dry spots.

Adhesion to micropatterned surfaces can be enhanced by static electric fields. Simple analytical models predict that the electroadhesion strength should scale with the square of the voltage, but experimental results show less-than-quadratic scaling. This discrepancy can be explained by considering low but electric field-dependent conductivity of air at high field strengths.

6.1 Instability of liquid rims and threads

When a thin film dewets by nucleation and growth of dry spots, the displaced liquid accumulates in a liquid rim near the contact line [see Fig. 2.1(e)]. We observed that the liquid rim and liquid threads which are often observed in experiments undergo instabilities. This process likely happens to minimize not only surface energy, but also the elastic energy in the system, at least when the rim and thread sizes are much larger than the elastocapillary lengthscale $\sim S/E$. Further research could try to determine the scaling of the instability wavelength with the rim or thread width.

As an example, Fig. 6.1 shows snapshots from an experiment where dewetting started with liquid film thickness of 250 μm. The liquid rim was very unstable and produced many liquid streaks. As the liquid film is displaced into these streaks, the rim is not growing in size. The resulting liquid threads undergo another instability and break up into droplets.

Furthermore, we observed several distinct features reoccurring across experiments which could be an interesting research topic. The blue arrows in Fig. 6.1(a) point out thin streaks produced in areas where the dry spot edge is convex. This local geometry is observed in many experiments and results in relatively thin threads of liquid which break up into very regular lines of small droplets. Instabilities in other parts of the liquid rim, where the dry spot edge is not convex, are more unstable in time [red arrow in Fig. 6.1(b)]. They produce short, thick liquid threads which often break off and result in large, irregular puddles and droplets. Trying to reproduce these features numerically could help to understand how the two types of liquid threads form.

Figure 6.2 shows snapshots from a numerical simulation of a liquid thread at a soft interface. The initially uniform thread (a) starts rippling (b,c) and breaks into droplets (d-f) which relax to a round

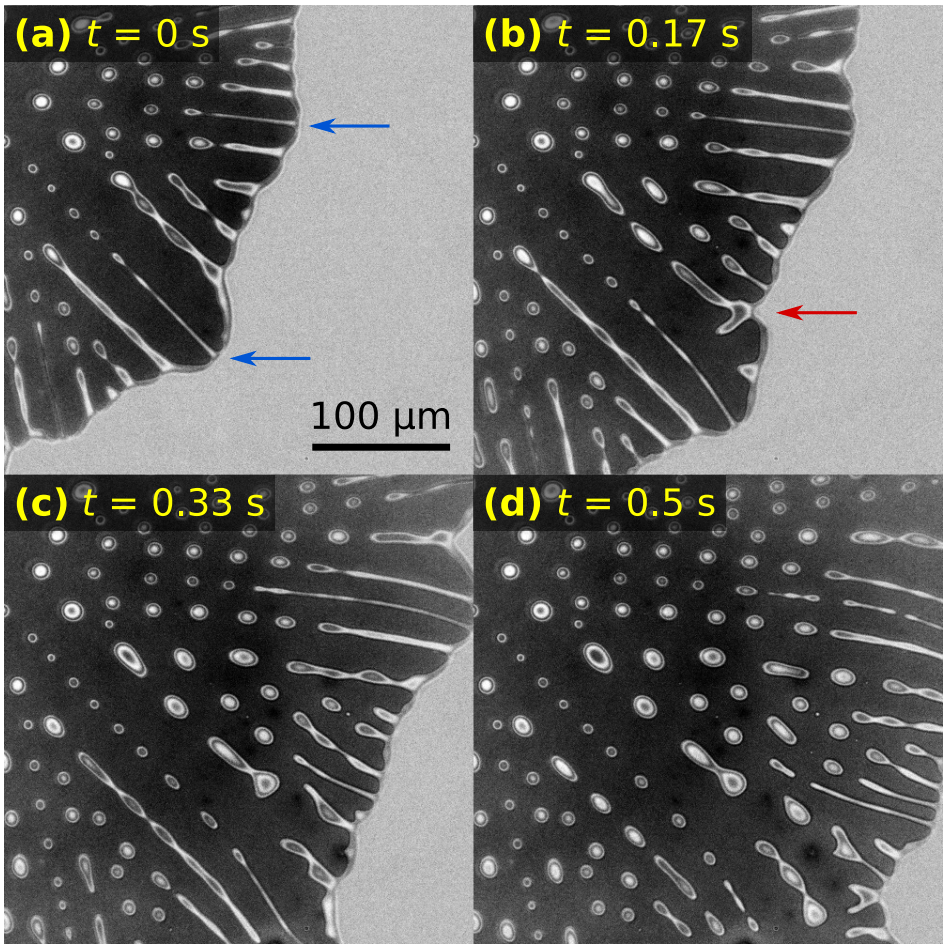

Figure 6.1: Snapshots from an experiment showing instabilities of the liquid rim and the liquid threads. Liquid film thickness at the start of dewetting was 250 µm.

shape (g). Similar simulations of larger systems, done systematically for a range of parameters, could be used to study this instability phenomenon. Care needs to be taken to develop a model which is accurate enough to predict the contact line motion correctly but which can also be solved quickly enough with given computational resources to allow solving for a sufficient range of parameters. Furthermore, the model domain needs to be large enough to exclude non-physical boundary interactions.

6.2 Viscous energy dissipation within a moving droplet at the contact line

The numerical model used to study the movement of droplets at soft interfaces matched well with some experimental results, where droplets moved with speed proportional to the local pressure gradient and coalesced fully with the outer bulk liquid in one motion. It couldn't predict the droplets which were observed to move much slower and undergo a partial coalescence cascade. The model could be expanded to feature some effect slowing down contact line movement in effort to reproduce the partial coalescence. We proposed surface roughness as a viable candidate, but considering rough surfaces in a three-dimensional numerical model is computationally expensive. Research could focus on developing a feasible model of contact line motion on a rough surface.

The velocity of droplets moving due to a pressure gradient depends on a balance of the elastic energy gain rate in the elastomer and viscous dissipation rate in the liquid. In chapter 3.3.1 we considered energy dissipation only in the bulk of the liquid. Further efforts could focus on studying the liquid motion at the contact line in the case of a moving droplet at a soft solid interface.

The difficulty in considering this case, compared to similar droplets moving in a solid-liquid-air system, is in problematic boundary conditions. If we consider an ellipsoidal droplet moving with the speed magnitude u in the $+x$ direction, the boundary velocities at the

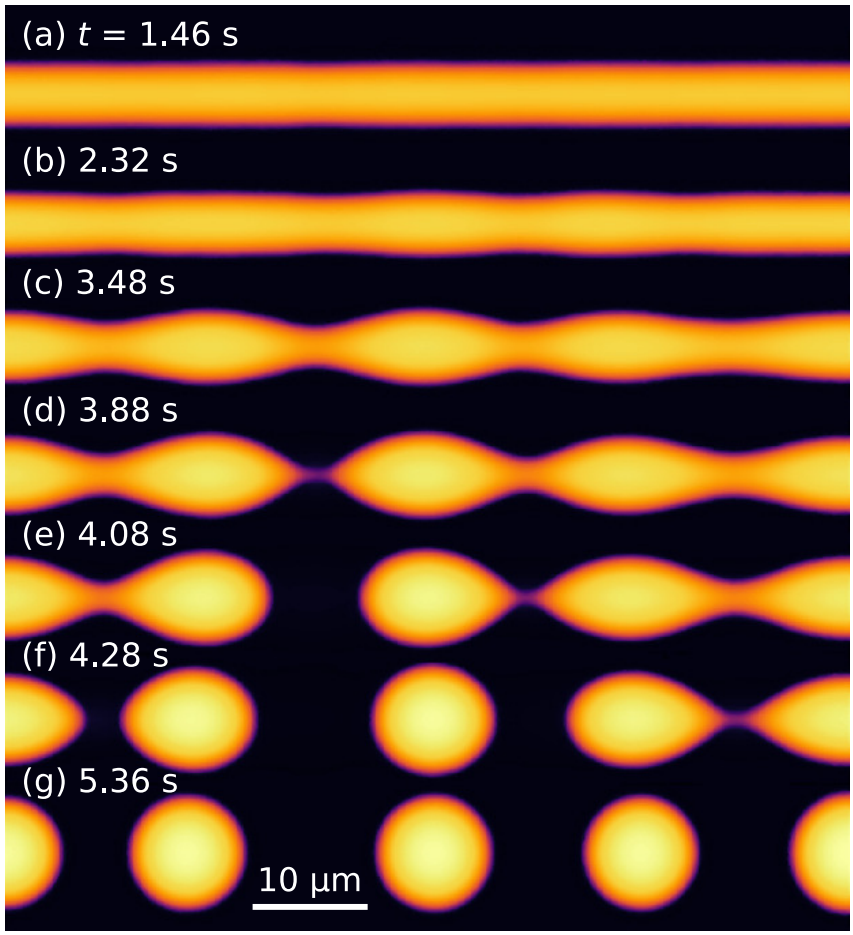

Figure 6.2: Numerical result showing breakup of a confined liquid thread. The initially uniform thread (a) starts rippling (b,c) and breaks into droplets (d-f) which relax to a round shape (g).

elastomer-liquid interfaces would be

$$\mathbf{v}_w = u \begin{pmatrix} -1 \\ 0 \\ \frac{h_d x}{a_d \sqrt{a_d^2 - x^2}} \end{pmatrix} \quad \text{and} \quad \mathbf{v}_b = u \begin{pmatrix} -1 \\ 0 \\ 0 \end{pmatrix}, \tag{6.1}$$

where we consider a reference frame where the droplet is static and the wall and base interfaces are sliding with velocities $\mathbf{v}_w$ and $\mathbf{v}_b$, respectively. In that case, at the contact line a classical corner flow problem arises with one boundary condition of constant imposed speed and the other one imposing zero normal flow. However, one of these boundaries is difficult to define analytically in a realistic manner. Using the approximate formula for $\mathbf{v}_w$ from Eq. (6.1) would introduce a spatial scale and a wall speed singularity to the problem, preventing the use of classic scale-independent corner flow solutions.

This problem could be approached for instance my means of molecular dynamics, trying to model liquid flow at a moving contact line between a soft polymer, a simple or complex polymeric liquid and a rigid wall or a symmetry plane. In that case, research could also focus on finding whether the chosen liquid will be fully pushed out from the closing gap at the receding contact line, or will it enter the dewetted area, forming a monolayer or even undergoing a confinement-induced phase transition.

We tried to tackle this issue only considering bulk liquid flow. The following results are included in effort to further illustrate the problem. Figures 6.3 and 6.4 show numerical results of solving the Stokes equation in the described droplet. In Fig. 6.3 we consider an elastomer-liquid-elastomer system which has a symmetry plane through the middle of the droplet. Due to symmetry, in (b-f) we only show the $z, y \geq 0$ part of the droplet. In Fig. 6.4 we consider an elastomer-liquid-rigid substrate system. The considered droplets are very flat and for clarity all illustrations are stretched in the z-direction tenfold. In Figs. 6.3(a) and 6.4(a) we present the boundary conditions as seen in the droplet's frame of reference. In Figs. 6.3(b-f) and 6.4(b-f) we show the flow lines [black, red in (d)] and speed magnitude (color cross-sections) from the Stokes equation solutions.

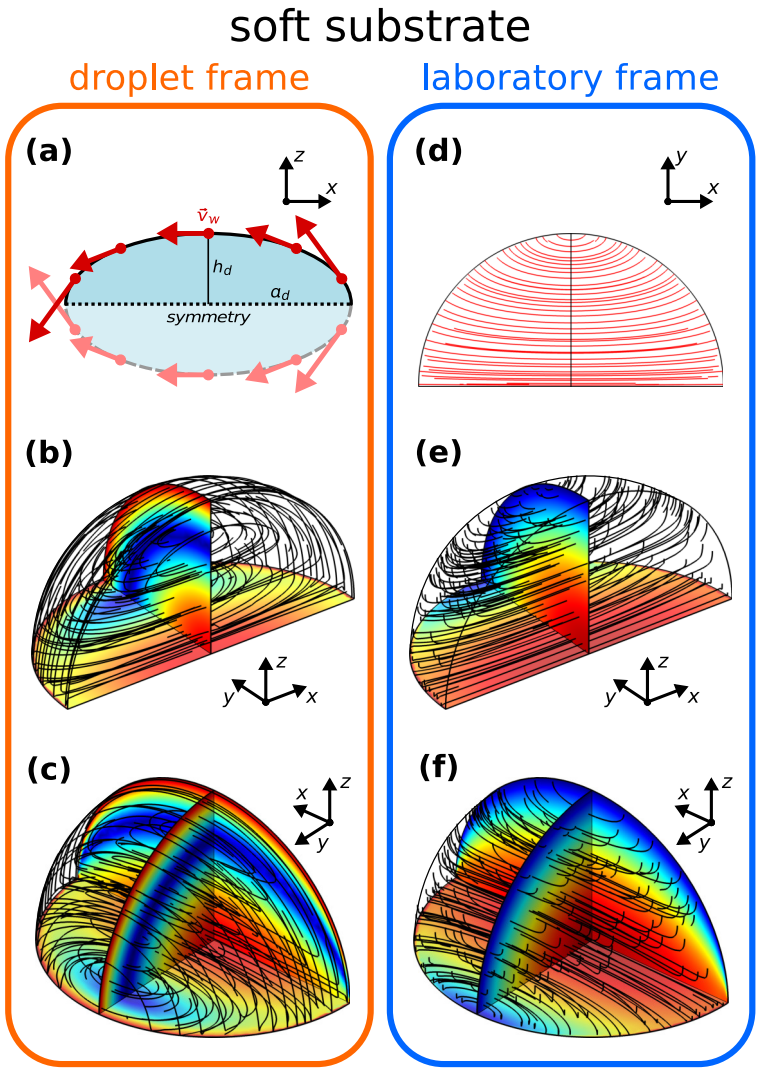

Figure 6.3: Flow pattern inside a droplet moving at an elastomer-elastomer interface. The droplet is ellipsoidal. Due to symmetry, only a quarter of the droplet is shown. In (g-l) the driplet is half-ellipsoidal, between a soft and a rigid material. (a,g) illustrate the sliding wall boundary conditions. (a-c) and (g-i) are in the droplet's moving frame of reference. (d-f) and (j-l) are in the laboratory frame. Hue at the cross-sectional planes indicates flow speed.

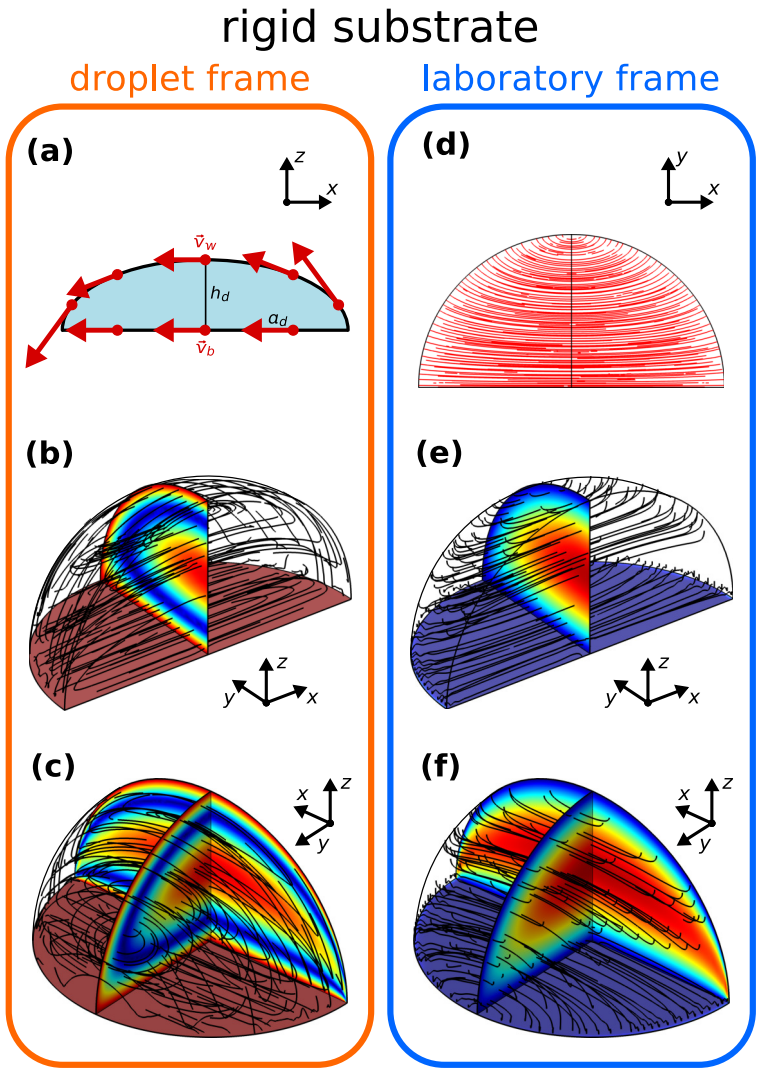

Figure 6.4: Flow pattern inside a droplet moving at an elastomer-rigid interface. In (a-f) the droplet is ellipsoidal, at an interface between two identical materials. Due to symmetry, only a quarter of the droplet is shown. In (g-l) the driplet is half-ellipsoidal, between a soft and a rigid material. (a,g) illustrate the sliding wall boundary conditions. (a-c) and (g-i) are in the droplet's moving frame of reference. (d-f) and (j-l) are in the laboratory frame. Hue at the cross-sectional planes indicates flow speed.

Acknowledgement

I would like to thank the European Union for financing my research, Jesse Kwaks, Vaishali Chopra, Dr. René Hensel and Prof. Eduard Arzt from the Leibniz-Institut für Neue Materialien, Saarbrücken, for their help.

This project has received funding from the European Union's Horizon 2020 research and innovation programme under the Marie Skłodowska-Curie grant agreement No. 642861.

Bibliography

[1] A. Z. Szeri. *Fluid film lubrication*. Cambridge University Press, 2010.

[2] A. Pandey, S. Karpitschka, C. H. Venner, and J. H. Snoeijer. "Lubrication of soft viscoelastic solids". In: *J. Fluid Mech.* 799 (2016), pp. 433–447.

[3] H. Grogger and M. Weiss. "Calculation of the hydroplaning of a deformable smooth-shaped and longitudinally-grooved tire". In: *Tire Sci. Technol.* 25 (1997), pp. 265–287.

[4] B. N. J. Persson, U. Tartaglino, O. Albohr, and E. Tosatti. "Sealing is at the origin of rubber slipping on wet roads". In: *Nat. Mater.* 3 (2004), p. 882.

[5] B. N. J. Persson, U. Tartaglino, O. Albohr, and E. Tosatti. "Rubber friction on wet and dry road surfaces: The sealing effect". In: *Phys. Rev. B* 71 (2005), p. 035428.

[6] J. R. Cho, H. W. Lee, J. S. Sohn, G. J. Kim, and J. S. Woo. "Numerical investigation of hydroplaning characteristics of three-dimensional patterned tire". In: *Eur. J. Mech. A* 25 (2006), pp. 914–926.

[7] M. Varenberg and S. N. Gorb. "Hexagonal surface micropattern for dry and wet friction". In: *Adv. Mater.* 21 (2009), pp. 483–486.

[8] T. F. Fwa, S. S. Kumar, K. Anupam, and G. P. Ong. "Effectiveness of tire-tread patterns in reducing the risk of hydroplaning". In: *Transp. Res. Rec.* 2094 (2009), pp. 91–102.

[9] S. Vincent, A. Sarthou, J.-P. Caltagirone, F. Sonilhac, P. Février, C. Mignot, and G. Pianet. "Augmented Lagrangian and penalty methods for the simulation of two-phase flows interacting with moving solids. Application to hydroplaning flows interacting with real tire tread patterns". In: *J. Comput. Phys.* 230 (2011), pp. 956–983.

[10] B. Zheng, X. Huang, W. Zhang, R. Zhao, and S. Zhu. "Adhesion Characteristics of Tire-Asphalt Pavement Interface Based on a Proposed Tire Hydroplaning Model". In: *Adv. Mater. Sci. Eng.* 2018 (2018), p. 5916180.

[11] H. F. Bohn and W. Federle. "Insect aquaplaning: Nepenthes pitcher plants capture prey with the peristome, a fully wettable water-lubricated anisotropic surface". In: *Proc. Natl. Acad. Sci. USA* 101 (2004), pp. 14138–14143.

[12] T. Nishi. "Influence of lubricant properties and contacting velocity on real contact formation between rubber and glass in a contact process". In: *Tribol. Int.* 127 (2018), pp. 240–244.

[13] T. Nishi. "Influence of curvature radius, elastic modulus, and contact velocity on real contact formation between rubber hemisphere and glass plate during contact process under a water-lubricated condition". In: *Tribol. Int.* 130 (2019), pp. 284–288.

[14] C. Auner, U. Palfinger, H. Gold, J. Kraxner, A. Haase, T. Haber, M. Sezen, W. Grogger, G. Jakopic, J. R. Krenn, G. Leising, and B. Stadlober. "Residue-free room temperature UV-nanoimprinting of submicron organic thin film transistors". In: *Org. Electron.* 10 (2009), pp. 1466–1472.

[15] C. Auner, U. Palfinger, H. Gold, J. Kraxner, A. Haase, T. Haber, M. Sezen, W. Grogger, G. Jakopic, J. R. Krenn, G. Leising, and B. Stadlober. "High-performing submicron organic thin-film transistors fabricated by residue-free embossing". In: *Org. Electron.* 11 (2010), pp. 552–557.

[16] S.-J. Choi, D. Tahk, and H. Yoon. "Spontaneous dewetting-induced residue-free patterning at room temperature". In: *J. Colloid Interface Sci.* 340 (2009), pp. 74–81.

[17] H. Yoon, S. H. Lee, S. H. Sung, K. Y. Suh, and K. Char. "Mold design rules for residual layer-free patterning in thermal imprint lithography". In: *Langmuir* 27 (2011), pp. 7944–7948.

[18] H. Yoon, H. Lee, and W. B. Lee. "Toward residual-layer-free nanoimprint lithography in large-area fabrication". In: *Korea-Aust. Rheol. J.* 26 (2014), pp. 39–48.

[19] M. Leitgeb, D. Nees, S. Ruttloff, U. Palfinger, J. Götz, R. Liska, M. R. Belegratis, and B. Stadlober. "Multilength scale patterning of functional layers by roll-to-roll ultraviolet-light-assisted nanoimprint lithography". In: *ACS Nano* 10 (2016), pp. 4926–4941.

[20] A. Martin, O. M. Rossier, A. Buguin, P. Auroy, and F. Brochard-Wyart. "Spinodal dewetting of thin liquid films at soft interfaces". In: *Eur. Phys. J. E* 3 (2000), pp. 337–341.

[21] K. Jacobs, R. Seemann, and S. Herminghaus. "Stability and dewetting of thin liquid films". In: *Polymer thin films*. World Scientific, 2008, pp. 243–265.

[22] A. D. Roberts and D. Tabor. "Surface forces: direct measurement of repulsive forces due to electrical double layers on solids". In: *Nature* 219 (1968), p. 1122.

[23] F. Brochard-Wyart and P. G. D Gennes. "Dewetting of a water film between a solid and a rubber". In: *J. Phys. Condens. Matter* 6 (1994), A9.

[24] P. Martin and F. Brochard-Wyart. "Dewetting at soft interfaces". In: *Phys. Rev. Lett.* 80 (1998), p. 3296.

[25] B. N. J. Persson, A. I. Volokitin, and E. Tosatti. "Role of the external pressure on the dewetting of soft interfaces". In: *Eur. Phys. J. E* 11 (2003), pp. 409–413.

[26] M. Li, J. Xie, Q. Dai, W. Huang, and X. Wang. "Effect of wetting case and softness on adhesion of bioinspired micropatterned surfaces". In: *J. Mech. Behav. Biomed. Mater.* 78 (2018), pp. 266 –272. ISSN: 1751-6161. DOI: https://doi.org/10.1016/j.jmbbm.2017.11.036.

[27] J. Xie, M. Li, Q. Dai, W. Huang, and X. Wang. "Key parameters of biomimetic patterned surface for wet adhesion". In: *Int. J. Adhes. Adhes.* 82 (2018), pp. 72 –78. ISSN: 0143-7496. DOI: https://doi.org/10.1016/j.ijadhadh.2018.01.004.

[28] M. Li, Q. Dai, W. Huang, and X. Wang. "Pillar versus dimple patterned surfaces for wettability and adhesion with varying scales". In: *J. R. Soc. Interface* 15 (2018), p. 20180681. DOI: 10.1098/rsif.2018.0681.

[29] F. Meng, Q. Liu, X. Wang, D. Tan, L. Xue, and W. J. P. Barnes. "Tree frog adhesion biomimetics: opportunities for the development of new, smart adhesives that adhere under wet conditions". In: *Phil. Trans. R. Soc. A* 377 (2019), p. 20190131. DOI: 10.1098/rsta.2019.0131.

[30] Z. Yoshimitsu, A. Nakajima, T. Watanabe, and K. Hashimoto. "Effects of surface structure on the hydrophobicity and sliding behavior of water droplets". In: *Langmuir* 18 (2002), pp. 5818–5822.

[31] M. Lundgren, N. L. Allan, T. Cosgrove, and N. George. "Molecular dynamics study of wetting of a pillar surface". In: *Langmuir* 19 (2003), pp. 7127–7129.

[32] B. He, N. A. Patankar, and J. Lee. "Multiple equilibrium droplet shapes and design criterion for rough hydrophobic surfaces". In: *Langmuir* 19 (2003), pp. 4999–5003.

[33] N. A. Patankar. "Transition between superhydrophobic states on rough surfaces". In: *Langmuir* 20 (2004), pp. 7097–7102.

[34] T. N. Krupenkin, J. A. Taylor, T. M. Schneider, and S. Yang. "From rolling ball to complete wetting: The dynamic tuning of liquids on nanostructured surfaces". In: *Langmuir* 20 (2004), pp. 3824–3827.

[35] J. G. Fan, D. Dyer, G. Zhang, and Y. P. Zhao. "Nanocarpet effect: Pattern formation during the wetting of vertically aligned nanorod arrays". In: *Nano Lett.* 4 (2004), pp. 2133–2138.

[36] E. Martines, K. Seunarine, H. Morgan, N. Gadegaard, C. D. Wilkinson, and M. O. Riehle. "Superhydrophobicity and superhydrophilicity of regular nanopatterns". In: *Nano Lett.* 5 (2005), pp. 2097–2103.

[37] K. Autumn, Y. A. Liang, S. T. Hsieh, W. Zesch, W. P. Chan, T. W. Kenny, R. Fearing, and R. J. Full. "Adhesive force of a single gecko foot-hair". In: *Nature* 405 (2000), pp. 681–685.

[38] K. Autumn, M. Sitti, Y. A. Liang, A. M. Peattie, W. R. Hansen, S. Sponberg, T. W. Kenny, R. Fearing, J. N. Israelachvili, and R. J. Full. "Evidence for van der Waals adhesion in gecko setae". In: *Proc. Natl. Acad. Sci. USA* 99 (2002), pp. 12252–12256.

[39] K. Autumn and A. M. Peattie. "Mechanisms of adhesion in geckos". In: *Integr. Comp. Biol.* 42 (2002), pp. 1081–1090.

[40] K. Autumn. "Gecko Adhesion: Structure, Function, and Applications". In: *MRS Bull.* 32 (2007), pp. 473–478.

[41] V. Barreau, R. Hensel, N. K. Guimard, A. Ghatak, R. M. McMeeking, and E. Arzt. "Fibrillar Elastomeric Micropatterns Create Tunable Adhesion Even to Rough Surfaces". In: *Adv. Funct. Mater.* 26 (2016), pp. 4687–4694.

[42] S. C. L. Fischer, E. Arzt, and R. Hensel. "Composite Pillars with a Tunable Interface for Adhesion to Rough Substrates". In: *ACS Appl. Mater. Interfaces* 9 (2017), pp. 1036–1044.

[43] K. H. Chu, R. Xiao, and E. N. Wang. "Uni-directional liquid spreading on asymmetric nanostructured surfaces". In: *Nat. Mater.* 9 (2010), pp. 413–417.

[44] C. W. Extrand, I. M. Sung, P. Hall, and D. Schmidt. "Superwetting of structured surfaces". In: *Langmuir* 23 (2007), pp. 8882–8890.

[45] C. Ishino, M. Reyssat, E. Reyssat, K. Okumura, and D. Quéré. "Wicking within forests of micropillars". In: *Europhys. Lett.* 79 (2007), pp. 8–12.

[46] L. Courbin, E. Denieul, E. Dressaire, M. Roper, A. Ajdari, and H. A. Stone. "Imbibition by polygonal spreading on microdecorated surfaces". In: *Nat. Mater.* 6 (2007), pp. 661–664.

[47] W. Barthlott and C. Neinhuis. "Purity of the sacred lotus, or escape from contamination in biological surfaces". In: *Planta* 202 (1997), pp. 1–8.

[48] H. J. Ensikat, P. Ditsche-Kuru, C. Neinhuis, and W. Barthlott. "Superhydrophobicity in perfection: the outstanding properties of the lotus leaf". In: *Beilstein journal of nanotechnology* 2 (2011), pp. 152–161.

[49] P. E. King, P. J. Pugh, M. R. Fordy, N. Love, and S. A. Wheeler. "A comparison of some environmental adaptations of the littoral collembolans anuridella marina (Willem) and anurida maritima (Guerin)". In: *J. Nat. Hist.* 24 (1990), pp. 673–688.

[50] J. Nickerl, M. Tsurkan, R. Hensel, C. Neinhuis, and C. Werner. "The multi-layered protective cuticle of Collembola: a chemical analysis". In: *Journal of The Royal Society Interface* 11 (2014), p. 20140619.

[51] L. Feng, S. Li, Y. Li, H. Li, L. Zhang, J. Zhai, Y. Song, B. Liu, L. Jiang, and D. Zhu. "Super-hydrophobic surfaces: From natural to artificial". In: *Adv. Mater.* 14 (2002), pp. 1857–1860.

[52] E. Nun, M. Oles, and B. Schleich. "Lotus-Effect-Surfaces". In: *Macromol. Symp.* 187 (2002), pp. 677–682.

[53] A. Marmur. "The lotus effect: Superhydrophobicity and metastability". In: *Langmuir* 20 (2004), pp. 3517–3519.

[54] N. A. Patankar. "Mimicking the lotus effect: Influence of double roughness structures and slender pillars". In: *Langmuir* 20 (2004), pp. 8209–8213.

[55] L. Gao and T. J. McCarthy. "The "lotus effect" explained: Two reasons why two length scales of topography are important". In: *Langmuir* 22 (2006), pp. 2966–2967.

[56] R. Hensel, R. Helbig, S. Aland, H. G. Braun, A. Voigt, C. Neinhuis, and C. Werner. "Wetting resistance at its topographical limit: The benefit of mushroom and serif T structures". In: *Langmuir* 29 (2013), pp. 1100–1112.

[57] R. Hensel, R. Helbig, S. Aland, A. Voigt, C. Neinhuis, and C. Werner. "Tunable nano-replication to explore the omniphobic characteristics of springtail skin". In: *NPG Asia Mater.* 5 (2013), e37.

[58] R. Hensel, A. Finn, R. Helbig, H. G. Braun, C. Neinhuis, W. J. Fischer, and C. Werner. "Biologically inspired omniphobic surfaces by reverse imprint lithography". In: *Adv. Mater.* 26 (2014), pp. 2029–2033.

[59] S. Arunachalam, R. Das, J. Nauruzbayeva, E. M. Domingues, and H. Mishra. "Assessing omniphobicity by immersion". In: *Journal of colloid and interface science* 534 (2019), pp. 156–162.

[60] S. Reddy, E. Arzt, and A. del Campo. "Bioinspired surfaces with switchable adhesion". In: *Adv. Mater.* 19 (2007), pp. 3833–3837.

[61] D. M. Drotlef, P. Blümler, and A. del Campo. "Magnetically actuated patterns for bioinspired reversible adhesion (dry and wet)". In: *Adv. Mater.* 26 (2014), pp. 775–779.

[62] U. Bauer, M. Scharmann, J. Skepper, and W. Federle. "'Insect aquaplaning' on a superhydrophilic hairy surface: how Heliamphora nutans Benth. pitcher plants capture prey". In: *Proc. R. Soc. B* 280 (2013), p. 20122569.

[63] J. N. Israelachvili. *Intermolecular and surface forces*. Academic Press, 2011.

[64] J.-M. Serayssol and R. H. Davis. "The influence of surface interactions on the elastohydrodynamic collision of two spheres". In: *J. Colloid Interface Sci.* 114 (1986), pp. 54–66.

[65] T. Becker and F. Mugele. "Collapse of molecularly thin lubricant layers between elastic substrates". In: *J. Phys. Condens. Matter* 15 (2002), S321.

[66] S. de Beer, D. t. Mannetje, S. Zantema, and F. Mugele. "Instability of confined water films between elastic surfaces". In: *Langmuir* 26 (2009), pp. 3280–3285.

[67] B. N. J. Persson and F. Mugele. "Squeeze-out and wear: fundamental principles and applications". In: *J. Phys. Condens. Matter* 16 (2004), R295.

[68] D. Bandyopadhyay, G. Singh, M. L. Becker, and A. Karim. "Capillary wave confinement-induced stabilization of polymer films". In: *ACS Appl. Mater. Interfaces* 5 (2013), pp. 4006–4010.

[69] M. Li, J. Xie, L. Shi, W. Huang, and X. Wang. "Controlling direct contact force for wet adhesion with different wedged film stabilities". In: *J. Phys. D* 51 (2018), p. 165305.

[70] F. Brochard-Wyart and P. Martin. "Adhesion of a soft rubber on a wet solid". In: *J. Adhes.* 67 (1998), pp. 139–151.

[71] G. Carbone and B. N. J. Persson. "Dewetting at soft viscoelastic interfaces". In: *J. Chem. Phys.* 121 (2004), pp. 2246–2252.

[72] A. Martin, A. Buguin, and F. Brochard-Wyart. "Dewetting nucleation centers at soft interfaces". In: *Langmuir* 17 (2001), pp. 6553–6559.

[73] H. R. Hertz. "Über die Berührung fester elastischer Körper". In: *J. Pure Appl. Math.* 92 (1882), pp. 156–171.

[74] I. D. Johnston, D. K. McCluskey, C. K. L. Tan, and M. C. Tracey. "Mechanical characterization of bulk Sylgard 184 for microfluidics and microengineering". In: *J. Micromech. Microeng.* 24 (2014), p. 035017.

[75] L. W. Schwartz and R. R. Eley. "Simulation of droplet motion on low-energy and heterogeneous surfaces". In: *J. Colloid Interface Sci.* 202 (1998), pp. 173–188.

[76] J. H. Snoeijer and B. Andreotti. "Moving contact lines: scales, regimes, and dynamical transitions". In: *Annu. Rev. Fluid Mech.* 45 (2013), pp. 269–292.

[77] M. K. Chaudhury and G. M. Whitesides. "Direct measurement of interfacial interactions between semispherical lenses and flat sheets of poly (dimethylsiloxane) and their chemical derivatives". In: *Langmuir* 7 (1991), pp. 1013–1025.

[78] Y. H. Mori, T. G. M. V de Ven, and S. G. Mason. "Resistance to spreading of liquids by sharp edged microsteps". In: *Colloids Surf.* 4 (1982), pp. 1–15.

[79] P. Martin, P. Silberzan, and F. Brochard-Wyart. "Sessile droplets at a solid/elastomer interface". In: *Langmuir* 13 (1997), pp. 4910–4914.

[80] A. A. Darhuber, S. M. Troian, and S. Wagner. "Physical mechanisms governing pattern fidelity in microscale offset printing". In: *J. Appl. Phys.* 90 (2001), pp. 3602–3609.

[81] D. Kang, E. Lee, H. Kim, Y.-M. Choi, S. Lee, I. Kim, D. Yoon, J. Jo, B. Kim, and T.-M. Lee. "Investigation on synchronization of the offset printing process for fine patterning and precision overlay". In: *J. Appl. Phys.* 115 (2014), p. 234908.

[82] H. M. Sauer, D. Daume, and E. Dörsam. "Lubrication theory of ink hydrodynamics in the flexographic printing nip". In: *J. Print Media Technol. Res.* 4 (2015), pp. 163–172.

[83] I. N. Sneddon. "The distribution of stress in the neighbourhood of a crack in an elastic solid". In: *Proc. Royal Soc. Lond. A* 187 (1946), pp. 229–260.

[84] M. Chudak, J. S. Kwaks, J. H. Snoeijer, and A. A. Darhuber. "Non-axisymmetric elastohydrodynamic solid-liquid-solid dewetting: Experiments and numerical modelling". In: *Eur. Phys. J. E* 43 (2020), p. 2.

[85] A. Hourlier-Fargette, A. Antkowiak, A. Chateauminois, and S. Neukirch. "Role of uncrosslinked chains in droplets dynamics on silicone elastomers". In: *Soft Matter* 13 (2017), pp. 3484–3491.

[86] K. L. Johnson, K. Kendall, and A. D. Roberts. "Surface energy and the contact of elastic solids". In: *Proc. Royal Soc. Lond. A* 324 (1971), pp. 301–313.

[87] G. E. Charles and S. G. Mason. "The mechanism of partial coalescence of liquid drops at liquid/liquid interfaces". In: *J. Colloid Sci.* 15 (1960), pp. 105–122.

[88] S. T. Thoroddsen and K. Takehara. "The coalescence cascade of a drop". In: *Phys. Fluids* 12 (2000), pp. 1265–1267.

[89] G. A. Bach, D. L. Koch, and A. Gopinath. "Coalescence and bouncing of small aerosol droplets". In: *J. Fluid Mech.* 518 (2004), pp. 157–185.

[90] E. M. Honey and H. P. Kavehpour. "Astonishing life of a coalescing drop on a free surface". In: *Phys. Rev. E* 73 (2006), p. 027301.

[91] X. Chen, S. Mandre, and J. J. Feng. "Partial coalescence between a drop and a liquid-liquid interface". In: *Phys. Fluids* 18 (2006), p. 051705.

[92] F. Blanchette and T. P. Bigioni. "Partial coalescence of drops at liquid interfaces". In: *Nat. Phys.* 2 (2006), p. 254.

[93] T. Gilet, K. Mulleners, J.-P. Lecomte, N. Vandewalle, and S. Dorbolo. "Critical parameters for the partial coalescence of a droplet". In: *Phys. Rev. E* 75 (2007), p. 036303.

[94] F. Blanchette and T. P. Bigioni. "Dynamics of drop coalescence at fluid interfaces". In: *J. Fluid Mech.* 620 (2009), pp. 333–352.

[95] F. H. Zhang, E. Q. Li, and S. T. Thoroddsen. "Satellite formation during coalescence of unequal size drops". In: *Phys. Rev. Lett.* 102 (2009), p. 104502.

[96] B. Ray, G. Biswas, and A. Sharma. "Generation of secondary droplets in coalescence of a drop at a liquid–liquid interface". In: *J. Fluid Mech.* 655 (2010), pp. 72–104.

[97] I. S. Klyuzhin, F. Ienna, B. Roeder, A. Wexler, and G. H. Pollack. "Persisting water droplets on water surfaces". In: *J. Phys. Chem. B* 114 (2010), pp. 14020–14027.

[98] H. P. Kavehpour. "Coalescence of drops". In: *Annu. Rev. Fluid Mech.* 47 (2015), pp. 245–268.

[99] A. Fakhari, D. Bolster, and L.-S. Luo. "A weighted multiple-relaxation-time lattice Boltzmann method for multiphase flows and its application to partial coalescence cascades". In: *J. Comput. Phys.* 341 (2017), pp. 22–43.

[100] J. E. Glass, R. D. Lundberg, and F. E. Bailey Jr. "The effect of polymeric hydrocolloids on the partial coalescence of liquid drops at liquid-liquid interfaces". In: *J. Colloid Interface Sci.* 33 (1970), pp. 491–507.

[101] J. D. Sartor and C. E. Abbott. "Some details of coalescence and charge transfer between freely falling drops in different electrical environments". In: *J. Rech. Atmos.* 6 (1972), pp. 479–493.

[102] H. T. Ochs III, K. V. Beard, R. R. Czys, N. F. Laird, D. E. Schaufelberger, and D. J. Holdridge. "Collisions between small precipitation drops. Part I: Laboratory measurements of bounce, coalescence, and temporary coalescence". In: *J. Atmos. Sci.* 52 (1995), pp. 2258–2275.

[103] K. V. Beard and H. T. Ochs III. "Collisions between small precipitation drops. Part II: Formulas for coalescence, temporary coalescence, and satellites". In: *J. Atmos. Sci.* 52 (1995), pp. 3977–3996.

[104] W. D. Ristenpart, J. C. Bird, A. Belmonte, F. Dollar, and H. A. Stone. "Non-coalescence of oppositely charged drops". In: *Nature* 461 (2009), p. 377.

[105] K. V. Beard, H. T. Ochs III, and S. Liu. "Collisions between small precipitation drops. Part III: Laboratory measurements at reduced pressure". In: *J. Atmos. Sci.* 58 (2001), pp. 1395–1408.

[106] P. Yue, C. Zhou, and J. J. Feng. "A computational study of the coalescence between a drop and an interface in Newtonian and viscoelastic fluids". In: *Phys. Fluids* 18 (2006), p. 102102.

[107] X. Chen, S. Mandre, and J. J. Feng. "An experimental study of the coalescence between a drop and an interface in Newtonian and polymeric liquids". In: *Phys. Fluids* 18 (2006), p. 092103.

[108] N. P. Kuznicki, M. Krasowska, P. M. F. Sellaperumage, Z. Xu, J. Masliyah, J. Ralston, and M. N. Popescu. "Cascade partial coalescence phenomena at electrolyte–oil interfaces and determination of bounds for the surface potential". In: *Soft Matter* 9 (2013), pp. 4516–4523.

[109] E. D Malmazet, F. Risso, O. Masbernat, and V. Pauchard. "Coalescence of contaminated water drops at an oil/water interface: Influence of micro-particles". In: *Colloids Surf., A.* 482 (2015), pp. 514–528.

[110] F. Blanchette, L. Messio, and J. W. M. Bush. "The influence of surface tension gradients on drop coalescence". In: *Phys. Fluids* 21 (2009), p. 072107.

[111] Y. Amarouchene, G. Cristobal, and H. Kellay. "Noncoalescing drops". In: *Phys. Rev. Lett.* 87 (2001), p. 206104.

[112] D. Fell, M. Sokuler, A. Lembach, T. F. Eibach, C. Liu, E. Bonaccurso, G. K. Auernhammer, and H.-J. Butt. "Drop impact on surfactant films and solutions". In: *Colloid Polym. Sci.* 291 (2013), pp. 1963–1976.

[113] D. W. Martin and F. Blanchette. "Simulations of surfactant effects on the dynamics of coalescing drops and bubbles". In: *Phys. Fluids* 27 (2015), p. 012103.

[114] T. Dong, W. H. Weheliye, P. Chausset, and P. Angeli. "An experimental study on the drop/interface partial coalescence with surfactants". In: *Phys. Fluids* 29 (2017), p. 102101.

[115] S. Shim and H. A. Stone. "Damped coalescence cascade of liquid drops". In: *Phys. Rev. Fluids* 2 (2017), p. 044001.

[116] K. Haldar, S. Chakraborty, and S. Chakraborty. "Influence of Marangoni stress on the variation in number of coalescence cascade stages". In: *Can. J. Chem. Eng.* 97 (2019), pp. 983–994.

[117] C. W. J. Berendsen, C. J. Kuijpers, J. C. H. Zeegers, and A. A. Darhuber. "Dielectrophoretic deformation of thin liquid films induced by surface charge patterns on dielectric substrates". In: *Soft Matter* 9 (2013), pp. 4900–4910.

[118] B. He and A. A. Darhuber. "Electrical surface charge patterns induced by droplets sliding over polymer and photoresist surfaces". In: *J. Micromech. Microeng.* 29 (2019), p. 105002.

[119] E. Arzt, S. Gorb, and R. Spolenak. "From micro to nano contacts in biological attachment devices". In: *Proc. Natl. Acad. Sci. USA* 100 (2003), pp. 10603–10606.

[120] R. Hensel, R. Helbig, S. Aland, H.-G. Braun, A. Voigt, C. Neinhuis, and C. Werner. "Wetting resistance at its topographical limit: the benefit of mushroom and serif T structures". In: *Langmuir* 29 (2013), pp. 1100–1112.

[121] M. Kamperman, E. Kroner, A. del Campo, R. M. McMeeking, and E. Arzt. "Functional adhesive surfaces with "gecko" effect: The concept of contact splitting". In: *Adv. Eng. Mater* 12 (2010), pp. 335–348.

[122] R. Hensel, K. Moh, and E. Arzt. "Engineering Micropatterned Dry Adhesives: From Contact Theory to Handling Applications". In: *Adv. Funct. Mater* 28 (2018), p. 1800865.

[123] N. Hosoda and S. N. Gorb. "Underwater locomotion in a terrestrial beetle: combination of surface de-wetting and capillary forces". en. In: *Proc. R. Soc. Lond. B: Biol. Sci.* 279 (Oct. 2012), pp. 4236–4242. ISSN: 0962-8452, 1471-2954. DOI: 10.1098/rspb.2012.1297.

[124] P. Rao, T. L. Sun, L. Chen, R. Takahashi, G. Shinohara, H. Guo, D. R. King, T. Kurokawa, and J. P. Gong. "Tough Hydrogels with Fast, Strong, and Reversible Underwater Adhesion Based on a Multiscale Design". en. In: *Adv. Mater.* 30 (Aug. 2018), p. 1801884. ISSN: 09359648. DOI: 10.1002/adma.201801884.

[125] W Federle, W. Barnes, W Baumgartner, P Drechsler, and J. Smith. "Wet but not slippery: boundary friction in tree frog adhesive toe pads". en. In: *J. R. Soc. Interface* 3 (Oct. 2006), pp. 689–697. ISSN: 1742-5689, 1742-5662. DOI: 10.1098/rsif.2006.0135.

[126] F. Meng, Q. Liu, X. Wang, D. Tan, L. Xue, and W. J. P. Barnes. "Tree frog adhesion biomimetics: opportunities for the development of new, smart adhesives that adhere under wet conditions". en. In: *Philos. Trans. R. Soc. A* 377 (July 2019), p. 20190131. ISSN: 1364-503X, 1471-2962. DOI: 10.1098/rsta.2019.0131.

[127] W. J. P. Barnes. "Biomimetic Solutions to Sticky Problems". In: *Science* 318 (2007), pp. 203–204. ISSN: 0036-8075. DOI: 10.1126/science.1149994.

[128] P. Glass, H. Chung, N. R. Washburn, and M. Sitti. "Enhanced Wet Adhesion and Shear of Elastomeric Micro-Fiber Arrays with Mushroom Tip Geometry and a Photopolymerized p(DMA-co-MEA) Tip Coating". en. In: *Langmuir* 26

(Nov. 2010), pp. 17357–17362. ISSN: 0743-7463, 1520-5827. DOI: 10.1021/la1029245.

[129] P. Glass, H. Chung, N. R. Washburn, and M. Sitti. "Enhanced Reversible Adhesion of Dopamine Methacrylamide-Coated Elastomer Microfibrillar Structures under Wet Conditions". en. In: *Langmuir* 25 (June 2009), pp. 6607–6612. ISSN: 0743-7463, 1520-5827. DOI: 10.1021/la9009114.

[130] A. Majumder, A. Sharma, and A. Ghatak. "A Bioinspired Wet/Dry Microfluidic Adhesive for Aqueous Environments". en. In: *Langmuir* 26 (Jan. 2010), pp. 521–525. ISSN: 0743-7463, 1520-5827. DOI: 10.1021/la9021849.

[131] B. Soltannia and D. Sameoto. "Strong, Reversible Underwater Adhesion via Gecko-Inspired Hydrophobic Fibers". en. In: *ACS Appl. Mater. Interfaces* 6 (Dec. 2014), pp. 21995–22003. ISSN: 1944-8244, 1944-8252. DOI: 10.1021/am5075375.

[132] J. K. A. Langowski, D. Dodou, M. Kamperman, and J. L. van Leeuwen. "Tree frog attachment: mechanisms, challenges, and perspectives". en. In: *Front. Zool.* 15 (Dec. 2018), p. 32. ISSN: 1742-9994. DOI: 10.1186/s12983-018-0273-x.

[133] Y. Wang, V. Kang, E. Arzt, W. Federle, and R. Hensel. "Strong Wet and Dry Adhesion by Cupped Microstructures". en. In: *ACS Appl. Mater. Interfaces* 11 (July 2019), pp. 26483–26490. ISSN: 1944-8244, 1944-8252. DOI: 10.1021/acsami.9b07969.

[134] Y. Ma, S. Ma, Y. Wu, X. Pei, S. N. Gorb, Z. Wang, W. Liu, and F. Zhou. "Remote Control over Underwater Dynamic Attachment/Detachment and Locomotion". en. In: *Adv. Mater.* 30 (July 2018), p. 1801595. ISSN: 09359648. DOI: 10.1002/adma.201801595.

[135] S. J. Kim, M. W. Moon, K. R. Lee, D. Y. Lee, Y. S. Chang, and H. Y. Kim. "Liquid spreading on superhydrophilic micropillar arrays". In: *J. Fluid Mech.* 680 (2011), pp. 477–487.

[136] A. Gauthier, M. Rivetti, J. Teisseire, and E. Barthel. "Role of kinks in the dynamics of contact lines receding on superhydrophobic surfaces". In: *Phys. Rev. Lett.* 110 (2013), pp. 1–5.

[137] Q. Yuan, X. Huang, and Y. P. Zhao. "Dynamic spreading on pillar-arrayed surfaces: Viscous resistance versus molecular friction". In: *Phys. Fluids* 26 (2014), pp. 1–11.

[138] J. Purtov, A. Verch, P. Rogin, and R. Hensel. "Improved development procedure to enhance the stability of microstructures created by two-photon polymerization". In: *Microelectron. Eng.* 194 (2018), pp. 45–50.

[139] R. K. Jayne, T. J. Stark, J. B. Reeves, D. J. Bishop, and A. E. White. "Dynamic Actuation of Soft 3D Micromechanical Structures Using Micro-Electromechanical Systems (MEMS)". In: *Adv. Mater. Technol.* 3 (2018), p. 1700293.

[140] R. Hensel, R. M. McMeeking, and A. Kossa. "Adhesion of a rigid punch to a confined elastic layer revisited". In: *J. Adhesion* 95 (2019), pp. 44–63. DOI: 10.1080/00218464.2017.1381603.

[141] A. Müller, M. C. Wapler, and U. Wallrabe. "A quick and accurate method to determine the Poisson's ratio and the coefficient of thermal expansion of PDMS". In: *Soft Matter* 15 (2019), pp. 779–784.

[142] M. Chudak, J. S. Kwaks, J. H. Snoeijer, and A. A. Darhuber. "Escape dynamics of liquid droplets confined between soft interfaces: non-inertial coalescence cascades". In: *Soft Matter* 16 (2020), pp. 1866–1876.

[143] K. L. Johnson. *Contact Mechanics*. Cambridge University Press, 1985.

[144] M. Li, J. Xie, L. Shi, W. Huang, and X. Wang. "Controlling direct contact force for wet adhesion with different wedged film stabilities". In: *J. Phys. D: Appl. Phys.* 51 (2018), p. 165305. DOI: 10.1088/1361-6463/aab58d.

[145] B Lorenz, B. A. Krick, N Mulakaluri, M Smolyakova, S Dieluweit, W. G. Sawyer, and B. N. J. Persson. "Adhesion: role of bulk viscoelasticity and surface roughness". In: *J. Phys.: Cond. Matt.* 25 (2013), p. 225004. DOI: 10.1088/0953-8984/25/22/225004.

[146] B Lorenz, B. A. Krick, N Rodriguez, W. G. Sawyer, P Mangiagalli, and B. N. J. Persson. "Static or breakloose friction for lubricated contacts: the role of surface roughness and dewetting". In: *J. Phys.: Cond. Matt.* 25 (2013), p. 445013. DOI: 10.1088/0953-8984/25/44/445013.

[147] C. Dhong and J. Frechette. "Coupled effects of applied load and surface structure on the viscous forces during peeling". In: *Soft Matter* 11 (10 2015), pp. 1901–1910. DOI: 10.1039/C4SM02616K.

[148] J.-H. Dirks. "Physical principles of fluid-mediated insect attachment - Shouldn't insects slip?" In: *Beilstein J. Nanotechnol.* 5 (2014), pp. 1160–1166. ISSN: 2190-4286. DOI: 10.3762/bjnano.5.127.

[149] B.-E. Pinchasik, J. Steinkühler, P. Wuytens, A. G. Skirtach, P. Fratzl, and H. Möhwald. "From Beetles in Nature to the Laboratory: Actuating Underwater Locomotion on Hydrophobic Surfaces". In: *Langmuir* 31 (2015), pp. 13734–13742. DOI: 10.1021/acs.langmuir.5b03821.

[150] Q. Barral, G. Ovarlez, X. Chateau, J. Boujlel, B. Rabideau, and P. Coussot. "Adhesion of yield stress fluids". In: *Soft Matter* 6 (6 2010), pp. 1343–1351. DOI: 10.1039/B922162J.

[151] Y. Chen, J. Meng, Z. Gu, X. Wan, L. Jiang, and S. Wang. "Bioinspired Multiscale Wet Adhesive Surfaces: Structures and Controlled Adhesion". In: *Adv. Funct. Mat.* 30 (2020), p. 1905287. DOI: 10.1002/adfm.201905287.

[152] J. A. Greenwood and K. L. Johnson. "The mechanics of adhesion of viscoelastic solids". In: *Philos. Mag. A* 43 (1981), pp. 697–711. DOI: 10.1080/01418618108240402.

[153] R. Gupta and J. Fréchette. "Measurement and scaling of hydrodynamic interactions in the presence of draining channels". In: *Langmuir* 28 (2012), pp. 14703–14712.

[154] G. A. Pilkington, R. Gupta, and J. Fréchette. "Scaling hydrodynamic boundary conditions of microstructured surfaces in the thin channel limit". In: *Langmuir* 32 (2016), pp. 2360–2368.

[155] T Chastel and A. Mongruel. "Squeeze flow between a sphere and a textured wall". In: *Phys. Fluids* 28 (2016), p. 023301.

[156] A Kalra, A Lowe, and A. M. Al-Jumaily. "Mechanical behaviour of skin: a review". In: *J. Mater. Sci. Eng* 5 (2016), p. 1000254.

[157] R. Hollis, J. Gowdy, and A. Rizzi. "Design and Development of a Tabletop Precision Assembly System". In: *Mechatronics Robot. Aachen, Ger* (2004), 1619–1623.

[158] M. Zhou, Y. Tian, D. Sameoto, X. Zhang, Y. Meng, and S. Wen. "Controllable Interfacial Adhesion Applied to Transfer Light and Fragile Objects by Using Gecko Inspired Mushroom-Shaped Pillar Surface". In: *ACS Appl. Mater. Interfaces* 5 (2013), 10137–10144.

[159] H. Jeong, J.-K. Lee, H. Kim, S. Moon, and K. Suh. "A Nontransferring Dry Adhesive with Hierarchical Polymer Nanohairs". In: *Proc. Natl. Acad. Sci* 106 (2009), 5639–5644.

[160] J. Purtov, M. Frensemeier, and E. Kroner. "Switchable Adhesion in Vacuum Using Bio-Inspired Dry Adhesives". In: *ACS Appl. Mater. Interfaces* 7 (2015), 24127–24135.

[161] S. Song, D.-M. Drotlef, C. Majidi, and M. Sitti. "Controllable Load Sharing for Soft Adhesive Interfaces on Three-Dimensional Surfaces". In: *Proc. Natl. Acad. Sci* 114 (2017), 4344– 4353.

[162] J. Booth, V. Tinnemann, R. Hensel, E. Arzt, R. McMeeking, and K. Foster. "Statistical Properties of Defect-Dependent Detachment Strength in Bioinspired Dry Adhesives". In: *J. R. Soc. Interface* 16 (2019).

[163] V. Tinnemann, L. Hernandez, S. C. Fischer, E. Arzt, R. Bennewitz, and R. Hensel. "In Situ Observation Reveals Local Detachment Mechanisms and Suction Effects in Micropatterned Adhesives". In: *Adv. Funct. Mater.* 29 (2019), p. 1807713.

[164] D. Paretkar, M. Kamperman, A. Schneider, D. Martina, C. Creton, and E. Arzt. "Bioinspired Pressure Actuated Adhesive System". In: *Mater. Sci. Eng., C* 31 (2011), 1152–1159.

[165] V. Tinnemann, E. Arzt, and R. Hensel. "Switchable Double-Sided Micropatterned Adhesives for Selective Fixation and Detachment". In: *J. Mech. Phys. Solids* 123 (2019), 20–27.

[166] M. Frensemeier, J. Kaiser, C. Frick, A. Schneider, E. Arzt, R. Fertig, and E. Kroner. "Temperature-Induced Switchable Adhesion Using Nickel-Titanium-Polydimethylsiloxane Hybrid Surfaces". In: *Adv. Funct. Mater* 25 (2015), 3013–3021.

[167] S. Reddy, E. Arzt, and A. Del Campo. "Bioinspired Surfaces with Switchable Adhesion". In: *Adv. Mater* 19 (2007), 3833–3837.

[168] J. Krahn, E. Bovero, and C. Menon. "Magnetic Field Switchable Dry Adhesives". In: *ACS Appl. Mater. Interfaces* 7 (2015), 2214–2222.

[169] D. Drotlef, P. Blümler, and A. Del Campo. "Magnetically Actuated Patterns for Bioinspired Reversible Adhesion (Dry and Wet)". In: *Adv. Mater* 26 (2014), 775–779.

[170] N. Nadermann, J. Ning, A. Jagota, and C.-Y. Hui. "Active Switching of Adhesion in a Film-Terminated Fibrillar Structure". In: *Langmuir* 26 (2010), 15464–15471.

[171] E. Kizilkan, J. Strueben, A. Staubitz, and S. Gorb. "Bioinspired Photocontrollable Microstructured Transport Device". In: *Sci. Robot* 2 (2017), p. 9454.

[172] C. Cao, X. Sun, Y. Fang, Q. Qin, A. Yu, and X. Feng. "Theoretical Model and Design of Electroadhesive Pad with Interdigitated Electrodes". In: *Mater. Des* 89 (2016), 485–491.

[173] J. Shintake, S. Rosset, B. Schubert, D. Floreano, and H. Shea. "Versatile Soft Grippers with Intrinsic Electroadhesion Based on Multifunctional Polymer Actuators". In: *Adv. Mater* 28 (2016), 231–238.

[174] J. Guo, T. Bamber, M. Chamberlain, L. Justham, and M. Jackson. "Optimization and Experimental Verification of Coplanar Interdigital Electroadhesives". In: *J. Phys. D. Appl. Phys* 49 (2016).

[175] B. Persson and J. Guo. "Electroadhesion for Soft Adhesive Pads and Robotics: Theory and Numerical Results". In: *Soft Matter* 15 (2019), 8032–8039.

[176] K. Asano, F. Hatakeyama, and K. Yatsuzuka. "Fundamental Study of an Electrostatic Chuck for Silicon Wafer Handling". it. In: *IEEE Trans. Ind. Appl* 38 (2002), 840–845.

[177] G. Monkman. "Electroadhesive microgrippers". In: *Ind. Robot* (2003).

[178] H. Prahlad, R. Pelrine, S. Stanford, J. Marlow, and R. Kornbluh. "Electroadhesive Robots - Wall Climbing Robots Enabled by a Novel, Robust, and Electrically Controllable Adhesion Technology". In: *Proc. - IEEE Int. Conf. Robot. Autom* (2008), 3028–3033.

[179] J. Shintake, V. Cacucciolo, D. Floreano, and H. Shea. "Soft Robotic Grippers". In: *Adv. Mater.* (2018).

[180] J. Krahn and C. Menon. "Electro-dry-adhesion". In: *Langmuir* 28 (2012), pp. 5438–5443.

[181] D. Ruffatto, A. Parness, and M. Spenko. "Improving Controllable Adhesion on Both Rough and Smooth Surfaces with a Hybrid Electrostatic/Gecko-like Adhesive". In: *J. R. Soc. Interface* 11 (2014), p. 20131089.

[182] L. Xu, H. Wu, G. Yao, L. Chen, X. Yang, B. Chen, X. Huang, W. Zhong, X. Chen, Z. Yin, et al. "Giant voltage enhancement via triboelectric charge supplement channel for self-powered electroadhesion". In: *ACS nano* 12 (2018), pp. 10262–10271.

[183] J. Guo, M. Tailor, T. Bamber, M. Chamberlain, L. Justham, and M. Jackson. "Investigation of Relationship between Interfacial Electroadhesive Force and Surface Texture". In: *J. Phys. D. Appl. Phys* 49 (2015).

[184] R. Krape. *Applications Study of Electroadhesive Devices; National Aeronautics and Space Administration.* NASA Contractor Report, CR-1211, 1968.

[185] M. Schargott, V. Popov, and S. Gorb. "Spring Model of Biological Attachment Pads". In: *J. Theor. Biol* 243 (2006), 48–53.

[186] J. Zambakas, D. Retalis, and D. Mavrakis. "A Simultaneous Interpretation, by Wind Speed and Direction, of Ambient Air Polar Conductivities in Athens, Greece". In: *Arch. Meteorol. Geophys. Bioclimatol. Ser. A* 33 (1985), 381–388.

[187] L. Smith and G. Schilling. “The Variation of Electrical Conductivity of Air within Sealed Rooms”. In: *J. Atmos. Terr. Phys* 4 (1954), 314–321.

[188] J. Mark. “Polymer Data Handbook”. In: *J. Am. Chem. Soc* 131 (2009), 16330–16330.

[189] G. Morey. “The Property of Glass”. In: *Am. Chem* (1954).

[190] E. Warburg and T. Ihmori. “Ueber Das Gewicht Und Die Ursache Der Wasserhaut Bei Glas Und Anderen Körpern”. de. In: *Ann. Phys* 263 (1886), 481–507.

[191] Y. Awakuni and J. Calderwood. “Water Vapour Adsorption and Surface Conductivity in Solids”. In: *J. Phys. D. Appl. Phys* 5 (1972), 1038–1045.

[192] B. Skinner, M. Loth, and B. Shklovksii. “Ionic Conductivity on a Wetting Surface”. In: *Phys. Rev. E - Stat. Nonlinear, Soft Matter Phys* 80 (2009).

[193] H. Curtis. “Insulating Properties of Solid Dielectrics”. In: *Bull. Bur. Stand* 11 (1915), p. 359.

[194] H. Carlon. “Electrical Properties of Atmospheric Moist Air: A Systematic, Experimental Study; U.S”. cs. In: *Army Technical Report* (1988).

[195] W. Cobb and H. Wells. “The Electrical Conductivity of Oceanic Air and Its Correlation to Global Atmospheric Pollution”. In: *J. Atmos. Sci* 27 (1970), 814–819.

[196] S. Sampath, V. Sasi Kumar, and S. Murali Das. “Airborne Measurements of Atmospheric Electrical Conductivities”. In: *Pure Appl. Geophys.* 143 (1994), 713–727.

[197] A. Van Hippel. *Tables of Dielectric Materials*. MIT Cambridge, Labortory for Insulation Research, 1944.

[198] F. Deyhimi and J. Munoz. “Surface Resistivity of Different Silylated Glasses”. de. In: *J. Appl. Electrochem* 14 (1984), 803–806.

[199] V. Paiva, L. Santos, D. Da Silva, T. Burgo, and F. Galembeck. “Conduction and Excess Charge in Silicate Glass/Air Interfaces”. In: *Langmuir* 35 (2019), 7703–7712.

[200] A. Moulson and J. Herbert. *Electroceramics: Materials, Properties, Applications*. John Wiley & Sons, 2003.

[201] J. Shackelford, Y.-H. Han, S. Kim, and S.-H. Kwon. *CRC materials science and engineering handbook*. CRC press, 2016.

[202] E. Kroner, R. Maboudian, and E. Arzt. "Adhesion Characteristics of Pdms Surfaces during Repeated Pull-off Force Measurements". In: *Adv. Eng. Mater* 12 (2010), 398–404.

List of Publications

Peer-reviewed articles based on this project

- M. Chudak, J. S. Kwaks, J. H. Snoeijer, and A. A. Darhuber. "Non-axisymmetric elastohydrodynamic solid-liquid-solid dewetting: Experiments and numerical modelling". In: *Eur. Phys. J. E* 43.1 (2020), p. 2.

- M. Chudak, J. S. Kwaks, J. H. Snoeijer, and A. A. Darhuber. "Escape dynamics of liquid droplets confned between soft interfaces: non-inertial coalescence cascades". In: *Soft Matter* 16.7 (2020), pp. 1866–1876.

- V. Chopra, M. Chudak, R. Hensel, A. A. Darhuber, and E. Arzt. "Enhancing Dry Adhesion of Polymeric Micropatterns by Electric Fields". In: *ACS Appl. Mater. Interfaces.* 12.24 (2020), pp. 27708–27716.

- M. Chudak, V. Chopra, R. Hensel, E. Arzt, and A. A. Darhuber. "Elastohydrodynamic dewetting of thin liquid films – elucidating underwater adhesion of topographically patterned surfaces". In review (2020).

Other peer-reviewed articles

- S. Pieprzyk, M. N. Bannerman, A. C. Brańka, M. Chudak, and D. M. Heyes. "Thermodynamic and dynamical properties of the hard sphere system revisited by molecular dynamics simulation". In: *Phys. Chem. Chem. Phys.* 21.13 (2019), pp. 6886–6899.

Selected oral presentations

- M. Chudak and A. A. Darhuber. "Dynamics of unstable dewetting at soft solid interfaces". Burgers Symposium, Lunteren, The Netherlands. (21–22 May 2019)
- M. Chudak, J.H. Snoeijer and A. A. Darhuber. "Dewetting of thin liquid films confined between soft elastic solids". Physics@Veldhoven, Veldhoven, The Netherlands. (22–23 January 2019)
- M. Chudak and A. A. Darhuber. "Instability of thin liquid films compressed between soft solids". European Coating Symposium, Fribourg, Switzerland. (8–10 November 2017)
- M. Chudak and A. A. Darhuber. "Adhesion to wet and icy surfaces". First Training School on Fundamental Aspects in Polymer Synthesis, Adhesion and Modelling, Patras, Greece. (14–16 September 2016)

Selected poster presentations

- M. Chudak, V. Chopra, R. Hensel and A. A. Darhuber. "Wet Adhesion of Patterned Soft Solid Surfaces". International Conference on Adhesion in Aqueous Media, Dresden, Germany. (9–12 September 2019)
- M. Chudak and M. Hoffmann. "Analysing the properties of photosensitizers used in photodynamic therapy". First Molecular Crystals Students Conference, Wrocław, Poland. (21–23 September 2011)

Curriculum Vitae

Maciej Chudak was born in 1991 in Poznań, Poland. Between 2010 and 2015 he studied technical physics at the Poznań University of Technology. He obtained an engineer's and a master's degree in cooperation with the Institute of Molecular Physics of the Polish Academy of Sciences, supervised by Dr. hab. Arkadiusz Brańka. In his thesis, he focused on granular dynamics and developed a three-dimensional numerical discrete element method model of a planetary ball mill. From 2015 to 2020 he worked as a Ph.D. student in the Fluids & Flows group in the Applied Physics Department of the Eindhoven University of Technology.

Dynamics of Wet Adhesion at Soft Interfaces

Maciej Chudak

Dynamics of Wet Adhesion at Soft Interfaces Maciej Chudak